

NORTHWESTERN UNIVERSITY

Cantilever-free Techniques and Tools for Delivering  
Materials and Energy to Surfaces

A DISSERTATION

SUBMITTED TO THE GRADUATE SCHOOL  
IN PARTIAL FULFILLMENT OF THE REQUIREMENTS

for the degree

DOCTOR OF PHILOSOPHY

Field of Materials Science

by

Chad Zhou

EVANSTON, ILLINOIS

August 2015

Copyright © 2015, Chad Zhou

All Rights Reserved

# ABSTRACT

## Cantilever-free Techniques and Tools for Delivering Materials and Energy to Surfaces

Yu Zhou

The thesis is divided into two parts. The first part, including chapter two through four, focuses on the fundamental understanding of polymeric materials transport and light energy delivery in cantilever-free scanning probe lithography (SBL). In Chapter two, I investigate the transport of block copolymer inks with varying viscosities, from an atomic force microscope (AFM) tip to a substrate. The size of the patterned block copolymer features has been determined to increase with dwell time and decrease with ink viscosity, which is explained by a mass transfer model.

In Chapter three, I explore the optical paths in apertureless pen array and find that by blocking the flat backing layer between pens, the optical interaction with the surface is dominated by the light at the tip of pens, allowing one to serially write sub-wavelength features. Furthermore, I find that the apertureless pen can be reversibly deformed to tune the illumination region from the submicrometer to micro-meter scale.

Chapter four introduces and evaluates the concept of using cantilever-free scanning probe arrays as structures that can modulate nanoscale ink flow and composition with light. By utilizing polymer pen arrays with an opaque gold layer surrounding the base of the transparent polymer pyramids, we show that inks with photopolymerizable or isomerizable constituents can be used in conjunction with light channelled through the pyramids to control ink viscosity or composition in a dynamic manner.

The second part of my thesis focuses on orientational control of metal nanoparticles and nanowires during capillary assembly. Chapter five and six describe the large-area alignment of multi-segmented nanowires and anisotropic gold nanoparticles in nanoscale trenches with control over their angular position facilitated by capillary forces. We elucidate the role of the geometry of the templates in the assembly of anisotropic nanoparticles consisting of different shapes and sizes. These insights allow us to design templates that immobilize individual triangular nanoprisms and concave nanocubes in a shape-selective manner. Furthermore, by studying the roles of interparticle forces in this method, we are able to construct face-to-face and edge-to-edge nanocube dimers and triangular nanoprism bowtie antennas.

---

Thesis Advisor: Professor Chad A. Mirkin

## Acknowledgements

First, I would like to thank my PhD advisor, Prof. Chad Mirkin, for letting me work in this research group for the past four years. I have been given numerous opportunities that have broadened and enriched my horizons ranging from writing papers, presenting in conferences, interacting with experts and leaders at other research entities and within industry. I appreciate very much Chad's support for my applications to fellowships and contests, including the Ryan Fellowship and the Chinese Government Award for Outstanding Self-financed Student.

I also want to acknowledge my committee members—Prof. Vinayak P. Dravid, Prof. Kenneth R. Shull and Prof. George C. Schatz—for their knowledge, advice, and inspirations during my qualification exam and thereafter. I acknowledge my mentors in the lab who helped me develop methodologies for research: Dr. Xiaozhu Zhou, Dr. Guoliang Liu, and Dr. Xing Liao.

I thank all my collaborators who have provided significant contributions and invaluable advice for many of the projects described in this dissertation: Dr. Xiaozhu Zhou, Dr. Zhuang Xie, Dr. Chuan Zhang, Daniel Park, Dr. Daniel Eichelsdoerfer, Dr. Andrew Senesi, Pengcheng Chen, Qingyuan Lin, Shu He. I also appreciate those who worked behind the scenes to help me: Dr. Sarah Petrosko, Pamela Walson, Jennifer McGinnis and Elizabeth Forest.

Last but not least, I thank my father and my wife Fang Wang (Piggy) for their love and constant support throughout my higher education.

## Table of Contents

ABSTRACT .....	3
Acknowledgement.....	5
Table of Contents .....	6
List of Figures .....	8
List of Tables.....	22
Chapter 1 Introduction.....	23
1.1    Nanolithography for Materials Science .....	24
1.2    Scanning Probe Lithographic Techniques.....	26
1.3    Cantilever-free Scanning Probe Architecture.....	27
1.3.1    Polymer Pen Lithography .....	28
1.3.2    Beam Pen Lithography.....	32
Chapter 2 The Role of Polymer Viscosity on Ink Transport in Dip-Pen Nanolithography ..	35
2. 1    Introduction .....	36
2. 2    Experimental Section.....	38
2. 3    Results and Discussion .....	40
2. 4    Conclusions .....	55
Chapter 3 Apertureless Cantilever-Free Pen Arrays for Scanning Photochemical Printing ..	56
3. 1    Introduction .....	57

3. 2 Experimental Section.....	59
3. 3 Results and Discussion .....	62
3. 4 Conclusions .....	81
Chapter 4 On-Tip Photo-Modulated Molecular Printing .....	82
4. 1 Introduction .....	83
4. 2 Experimental Section.....	86
4. 3 Results and Discussion .....	88
4. 4 Conclusions .....	106
Chapter 5 Capillary Force-driven, Large-area Alignment of Multi-segmented Nanowires	107
5.1. Introduction .....	108
5.2. Experimental Section.....	112
5.3. Results and Discussion .....	113
5.4. Conclusions .....	131
Chapter 6 Shape-Selective Deposition and Assembly of Anisotropic Nanoparticles.....	132
6.1. Introduction .....	133
6.2. Experimental Section.....	135
6.3. Results and Discussion .....	140
6.4. Conclusions .....	154
References .....	155

## List of Figures

<b>Figure 1.1</b> Photographic and scanning electron microscope (SEM) images of a fabricated PPL pen array.....	30
<b>Figure 1.2</b> Z-piezo extension of feature size control. a) Schematic image illustrated how low and high pressure on the pen array produce different feature size; b) SEM image of a dot array with different z-piezo extension.....	31
<b>Figure 1.3</b> Beam pen lithography. a) Schematic of BPL, where transparent polymer tips are coated with an opaque metal layer (gold) except at the end of the tips. In this way, light only exposes a light-sensitive photoresist-coated surface at the tip. b) SEM image of a FIB fabricated BPL pen array with aperture size smaller than 100 nm; c) SEM image of a chromium dot array created by BPL arrays (after metal evaporation and photoresist lift-off), in which the apertures were fabricated by FIB. Feature diameter is 111+11 nm; d) Optical microscope image of a array of Chicago skyline by BPL .....	34
<b>Figure 2.1</b> Hydrodynamic radius of the block copolymer micelles measured with dynamic light scattering.....	42
<b>Figure 2.2</b> (top) Shear stress as a function of shear rate for block copolymer inks with different Au loading $\alpha$ . (bottom) Viscosity of polymer inks with various amount of Au loading. The ink viscosity is almost doubled as the Au loading increases from 1:64 to 1:4. (inset)	

Exemplary viscosity measurement of a block copolymer ink with Au loading of 1:64. The viscosity reaches a plateau at high shear rates and the ink shows shear thinning behavior. .43

**Figure 2.3** AFM height images of the patterned polymer features from different inks. The Au

loading,  $\alpha$ , ranges from 1:4 to 1:64, and the patterning dwell time ranges from 0.01 to 10 s.

The dwell time sequence and scale bars apply to all AFM images.....45

**Figure 2.4** (a, b) Diameter and (c, d) volume of patterned polymer features as a function of dwell

time and Au loading. (b) and (d) are expanded views of (a) and (c) at lower dwell times,

respectively. Solid lines are a guide to the eye.....46

**Figure 2.5** (a) Diameter of the patterned block copolymer features with the same dwell time of

0.01 S as a function of Au loading. The four points are from four different pens. (b) Fitting

of polymer feature volume as a function of dwell time. Error bars are omitted for clarity...47

**Figure 2.6** Schematic of mass transfer during DPN patterning of an aqueous polymer ink. **a**, An

AFM tip with defined cylindrical coordinates. **b**, Profile of the ink velocity ( $v$ ) across a

horizontal thin slab. The tip diameter is  $R_1$ , and the thickness of polymer ink layer is  $R_2-R_1$ .

**c**, The polymer ink transfers from the tip to a hydrophobic substrate through a meniscus. **d**,

The final volume ( $V$ ) of the patterned polymer features as a function of dwell time ( $t$ ) and

ink viscosity ( $\mu$ ). .....50

**Figure 2.7** SEM image of nanoparticles synthesized within patterned polymer nanoreactors with various dwell times. The Au loading  $\alpha$  in the ink is 1:4. The dwell time follows the same sequence as that in Fig 3. For clarity, only the first two dwell times are shown.....52

**Figure 2.8** The scaling behavior of nanoparticle size. **a**, Diameter of Au nanoparticles in polymer nanoreactors. The nanoparticle size scales linearly with the size of polymer nanoreactors. **b**, The slope ( $\beta$ ) of the fitted lines in **(a)** scales linearly with  $3\alpha$ .....54

**Figure 3.1** Principles and fabrication of apertureless cantilever-free pen arrays. (A) Optical microscope image and schematic illustration showing the four light paths present when elastomeric pyramids are illuminated. These suggest that if the light incident on the back layer could be blocked, light at the tip of the pen will dominate the optical interaction with the surface. (B) Schematic of the fabrication of the apertureless BPL pen arrays: (i) evaporation of 5 nm Ti and 200 nm Au on hard polydimethylsiloxane (*h*-PDMS) pen arrays; (ii) spin coating of PMMA that only covers flat region of the pen array; (iii) chemical etching of metal layer followed by removal of PMMA. (C) Scanning electron microscopy (SEM) image of the as-fabricated apertureless pen arrays. (D) Schematic of scanning optical lithography using the apertureless cantilever-free pen arrays. ....64

**Figure 3.2** Force dependence in photoresist patterns generated with an apertureless cantilever-free pen array. (A) Dark field optical microscope image of a large region of developed photoresist patterns. Each  $7 \times 3$  array of dots is written by a single pen under same exposure

dose but with a z-piezo extension that increases from left to right. (B) Tapping-mode AFM image of a typical dot array showing the change in size and shape with increasing z-piezo extension from left to right. (C) Average size of features written at varying z-piezo extension.....67

**Figure 3.3** Effect of exposure dose on the photoresist patterns generated with an apertureless cantilever-free pen array. (A&B) Dark field optical microscope images of a large region of developed photoresist patterns by varing exposure dose (A), and one typical array of dots produced with varied exposure time from 1 to 10 s and  $Z_{ext}$  of 0, 2, 4 and 6  $\mu\text{m}$  from bottom to top row. (C) Tapping-mode AFM images of the patterned dot arrays shown in (B). Scale bars: 5  $\mu\text{m}$ . (D) Plot of feature size at initial contact with exposure time. (E) Plot of volume of developed photoresist versus z-piezo extension. (F) Plot of fraction of remaining thickness in the center of patterns versus the logarithm of exposure time. (G) Statistic results of maximum depth in photoresist patterns with the exposure time and the z-piezo extension.....71

**Figure 3.4** Near-field intensity profiles generated by FDTD simulations. (A) From top to bottom: intensity profiles at horizontal planes at the top, in the middle and at the bottom of photoresist and at a vertical plane. The tip size is 0.2  $\mu\text{m}$ . (B-C) The same information as (A) for the tip sizes of 1.2 and 3.2  $\mu\text{m}$ . Scale bar: 2  $\mu\text{m}$ . .....73

**Figure 3.5** Generation of feature gradients with force-tuned size and shape. (A) Schematic of a tilted lithography experiment using apertureless pen arrays. (B) Representative dark-field optical microscope and SEM images of Au dot arrays generated at the left, middle and right edges of a ~0.5 cm wide pen array. Here, the average sizes were  $2.91 \pm 0.12 \mu\text{m}$ ,  $1.48 \pm 0.07 \mu\text{m}$  and  $0.41 \pm 0.09 \mu\text{m}$  from left to right. Scale bars are  $100 \mu\text{m}$  and  $5 \mu\text{m}$ , respectively.....76

**Figure 3.6** (A-B) SEM images of Au patterns arrays fabricated with 40 nm photoresist and 150 nm lift-off resist. By adjusting  $Z_{\text{ext}}$  and exposure time, we obtained Au features with various shapes (A) and dot arrays with average size of  $250 \pm 30 \text{ nm}$  (B). (C) Au lines patterned by adjusting  $Z_{\text{ext}}$  to write pixels with different sizes.....77

**Figure 3.7** Simultaneous delivery of optical energy and materials. (A) Schematic of photochemical printing of Rhodamine-modified thiol inks by thiol-ene photochemistry. (B) Fluorescence microscope image ( $\lambda_{\text{ex}} = 537\text{-}562 \text{ nm}$ ,  $\lambda_{\text{em}} = 570\text{-}640 \text{ nm}$ ) of the patterned  $4 \times 3$  arrays with illumination times of 1, 2, 3, and 4 min from bottom to top rows by apertureless pens. (C) Fluorescence microscope image of an array patterned by a single pen, showing dots with (right 3 columns) and without (left 1 column) UV illumination. Scale bar:  $10 \mu\text{m}$ . (D) Intensity profiles of the patterned features with different illumination times as well as the control group, indicated by the dotted lines shown in (C).....80

**Figure 4.1** Schematic illustration of on-tip photo-modulated molecular printing in which nanoscale photoreactions will be induced in the ink flow by simultaneous light illumination confined on the pyramidal tip. Photocontrol of ink transport and chemical composition of the printed features is demonstrated utilizing either photopolymerization or photoisomerization of ink molecules.....85

**Figure 4.2** Photo-modulated ink transport. (A) Dark-field optical microscope image of the printed features of NOA photopolymer ink under dark (left) and simultaneous UV illumination (right) conditions. (B) Magnified atomic force microscopy (AFM) image of one typical NOA dot array patterned with UV light, with the white arrows showing the writing direction. The dwell time for each dot is 5 s. (C) Plot of feature volume with time for two typical arrays patterned under dark and UV light. The UV intensity is  $\sim 0.1 \text{ mW/cm}^2$ . (D) Dwell-time dependence of the NOA feature volume with varied UV illumination time, with statistics from arrays patterned by 5 pens. (E) AFM image of NOA dot features generated on Au substrate with size ranging from 100 to 40 nm by 18-min UV illumination. The UV intensity is  $\sim 0.1 \text{ mW/cm}^2$ . .....91

**Figure 4.3** (A) AFM images of a typical dot array for time-dependent ink transport study in which each column was patterned with different UV illumination time sequentially, and a control array patterned under dark. (B) Plot of deposition rate with UV illumination time corresponding to Figure 2D. Statistics are obtained from arrays printed by 5 pens.....92

**Figure 4.4** Size uniformity statistics of NOA dot features over a  $3\times 3$  mm<sup>2</sup> area from randomly selected 11 arrays. .... 95

**Figure 4.5** (A) Scanning electron microscope (SEM) image of a dot array of PEGDA/PEO-b-P2VP/HAuCl<sub>4</sub> ink printed under UV illumination and after annealing. The UV intensity is ~150 mW/cm<sup>2</sup>. (B) Magnified SEM image of the patterned polymer spots with single Au nanoparticles inside. From left to right, the polymer feature size was 1100, 760, and 325 nm, corresponding to nanoparticles with size of 19, 15, and 8 nm, respectively. Scale bars: 200 nm. (C) Plot of Au nanoparticles size with printed polymer feature size controlled by light.

..... 96

**Figure 4.6** Reversible modulation of ink properties by light switching. (A) Schematic illustrations of light propagation on different pen arrays and the resulted AFM images of dot arrays patterned with switched light. Scale bars: 10  $\mu$ m. (B) Plot of feature volume ratio V/V<sub>0</sub> with time during the patterning with switched light by three types of pyramidal pen arrays. The UV intensity is ~0.1 mW/cm<sup>2</sup>. .... 98

**Figure 4.7** (A) SEM image of the apertureless pen array, where  $L_{tip}$  represents the edge length of the apertureless tip. (B) SEM image of the ink-coated pen array after spin coating, showing the ink accumulation around the base of pens. The image is obtained by curing the NOA ink on the pen array from front side. (C) SEM image of the ink-coated pen array after back-side UV illumination for 40 min and acetone rinsing. (D) Schematic illustration of the ink

refilling and mixing mechanism for recovery of the ink properties. (E) The effect of  $L_{\text{tip}}$  on the feature volume ratio change during the patterning with switched light. The UV intensity is  $\sim 2 \text{ mW/cm}^2$  ..... 100

**Figure 4.8** Effect of photopolymerization on size decay and recovery. (A) Plot of feature volume ratio with time, in which the UV illumination time was varied from 390 s to 900 s. The UV intensity is  $\sim 0.1 \text{ mW/cm}^2$ . (B) Plot of decay ratio and recovery ratio with the UV illumination time, with statistics from 5 pens. (C) Plot of feature volume ratio with time by varying the applied UV intensity. The edge length of the used apertureless tip is 30  $\mu\text{m}$  for all the figures. ..... 102

**Figure 4.9** Photo-reversible modulation of pattern functionality. (A) Schematic illustration of photoisomerization between spiropyran (SP) and merocyanine (MC) structures. The MC structure shows intense red fluorescence. (B) Dark-field and corresponding fluorescence ( $\lambda_{\text{ex}} = 537\text{--}562 \text{ nm}$ ,  $\lambda_{\text{em}} = 570\text{--}640 \text{ nm}$ ) microscope images of two interlaced arrays of PEG/SP ink printed with UV and visible light illumination, respectively. The UV intensity is  $\sim 2 \text{ mW/cm}^2$  and the power for green light is  $\sim 2.5 \text{ mW/cm}^2$ . (C) Fluorescence microscope image of the printed dot arrays under alternately varied visible and UV light in each row, with the white arrow showing the writing direction. (D) Plot of fluorescence intensity with the alternation of light. ..... 105

**Figure 5.1** Schematic illustration of the alignment of multi-segmented nanowires into trenches

by capillary forces. (A) Functionalization of nanowires with CTAB in a 0.45 mM CTAB aqueous solution. Coating of a bilayer CTAB on the surface of the nanowires prevents their aggregation and increases the stability of the suspension. (B) (i) Fabrication of PDMS stamp with negative trenches by curing elastomers on a silicon master with positive features. (ii) Alignment of nanowires into the trenches when a drop of nanowire solution moves across the trench area driven by a drying process (via heating).....111

**Figure 5.2** Silicon master and PDMS stamps. AFM image (A) and height profile (B) of raised

HSQ features confirm the height is ~35 nm after E-beam patterning and development. (C) SEM image for the same raised HSQ features as in (A). (D) SEM image of the PDMS stamp with negative trenches made from molding the elastomer on the master. Scale bars: 1  $\mu\text{m}$ .....115

**Figure 5.3** Comparison of electrochemically-synthesized nanowires (A) before and (B) after

CTAB functionalization. The nanowires that were not functionalized with CTAB using the aforementioned process settle to the bottom within a few hours (A). The CTAB-functionalized nanowires were well-dispersed without settling for up to 24 hours (B). (C) UV-Vis spectra of CTAB-functionalized nanowires as-prepared and after sitting for 24 hours show good stability.....118

**Figure 5.4** Representative SEM images and angle statistics of the aligned multi-segmented nanowires. (A) Array of aligned nanowires consisting of two Au segments separated by a short Ni segment. (B) Distribution of the orientation of aligned nanowires with a length of 250 nm. The inset schematic shows how the alignment angle  $\theta$  is measured. The width of the histogram bar is  $1^\circ$ . (C-E) Arrays of nanowires with a diameter of 35 nm and consisting of Au and Ni segment with different lengths: (C) Total length:  $252 \pm 24$  nm, Ni segment:  $29 \pm 4$  nm, aspect ratio: 7; (D) Total length:  $177 \pm 9$  nm, Ni segment:  $11 \pm 3$  nm, aspect ratio: 5; (E) Total length:  $125 \pm 8$  nm, Ni segment:  $2 \pm 0.4$  nm, aspect ratio: 3.5. Scale bars: 1  $\mu\text{m}$ .

.....120

**Figure 5.5** SEM image comparison of the accumulation zone of nanowires synthesized through (A) the OWL method and (B) surfactant-mediated chemical reduction method. (A) Disordered domains are formed due to rough wire surfaces (Inset, TEM image) of the multi-segmented nanowires. (B) Ordered domains are formed due to accumulation of the nanorods with atomically smooth surfaces (Inset, TEM image). Inset scale bars: 80 nm.

**Figure 5.6** Transfer of multi-segmented nanowire arrays to a target substrate (e.g., graphene) by micro-contact printing. (A) (i) Positioning nanowire arrays on top of graphene with a home-made micro-manipulator. (ii) Nanowires are transferred by applying pressure on the stamp against the target substrate at 135 °C. (B) SEM images of the transferred nanowires on a

single layer of graphene, before and after Ni etching. The registry of Au segments is maintained.....124

**Figure 5.7** (A) Homemade apparatus for positioning aligned nanowires on a graphene sheet. The apparatus allows one to control registry of the nanowire array and target substrate. (B) Optical image of the transferred nanowires on a few-layer graphene flake made by mechanical exfoliation.....126

**Figure 5.8** Fabrication of gapped graphene nanoribbons and SERS substrate. (A) Aligned graphene nanoribbons generated by using the gapped nanowires from Figure 4B as etch masks. Nanoribbons 200 nm long with a gap of ~25 nm were fabricated. (B) A SERS measurement of 1,4-BDT from aligned gapped nanowires. A row of hot spots is shown in the top-left inset. a.u., arbitrary units.....127

**Figure 5.9** (A) Raman mapping of aligned graphene ribbons. (B) Spectra of ribbon regions and background in (A) show clear G and 2D peaks from the graphene ribbons. ....128

**Figure 5.10** Density control of the aligned nanowires. SEM images of aligned nanowires that were transferred to a Si substrate with (A) a lateral pitch of 400 nm and a vertical pitch of 700 nm and (B) a lateral and vertical pitch of 700 nm. Scale bars: 500 nm. ....130

**Figure 6.1** Schematic process of large-area, shape-selective assembly of Au nanoprisms into pre-defined triangular trenches on a PDMS stamp. During the evaporation of the nanoprism solution droplet at 40 °C, a dense packing zone of nanoprisms is formed at the drop edge.

The prisms in the packing zone are immobilized in the templates due to capillary forces present when the drop shrinks and moves over the trench area ..... 141

**Figure 6.2** SEM images of the dense packing zones of nanoparticles at the drop edge. (A) Concave nanocubes. (B) Nanoprism after purification. (C) As-synthesized nanoprisms with impurity spherical nanoparticles. Scale bars: 500 nm ..... 142

**Figure 6.3** Large-area assembly of gold nanoprisms with control over the angular position. SEM image (left) shows an array of mostly single nanoprism assembled in triangular templates with inset that highlights the control over angular orientation. Scale bar: 500 nm. The dark-field microscope image (right) shows the downward movement (as shown by the arrow) of a drop edge across the template regions as water evaporates ..... 144

**Figure 6.4** Representative SEM images and angular statistics of the assembled Au nanostructures. Arrays of (A) nanoprisms and (B) concave nanocubes with edge lengths of 100 nm assembled on PDMS substrates. Insets shows schematics of nanoprisms and cubes aligned to triangular and square templates. Scale bars: 1  $\mu$ m. Angular statistics of the (C) nanoprism and (D) concave nanocube within the templates show narrow orientation distributions within  $\pm 6^\circ$  and  $\pm 5^\circ$ , respectively. Insets show how the angular orientation is defined ..... 145

**Figure 6.5** Shape-selective template-assisted assembly and purification of nanoprisms. (A) TEM image of the product of the Au nanoprism synthesis containing nanoprism products (edge

length: 140 nm, thickness: 7.5 nm) and spherical nanoparticle impurities (diameter: 35 nm).

(B) Schematics showing that gold nanoprisms are selectively assembled to the shallow triangular templates while spherical nanoparticles with a much larger diameter are not. In the bottom scheme, the particles and trenches are to-scale. (C) SEM image of the assembly of as-synthesized nanoprisms into 20 nm deep templates. No spherical particles were found in a template area consisting of two thousand templates. Scale bars: 500 nm.....148

**Figure 6.6** Representative SEM images of nanoparticle dimers consisting of concave cubes (A: face-to-face; B: edge-to-edge) and nanoprism bowties (C, D). Scale bars: 500 nm. Large immersion forces between the cubes in the face-to-face dimers (E) are responsible for pulling the cubes together to form intimate contact, while smaller immersion force between the cubes in the edge-to-edge dimers (F) and prisms in the bowties (G) do not pull the individual particles together. ....151

**Figure 6.7** Polarization-dependent field-enhancement of face-to-face concave nanocube dimers by Raman spectroscopy and FDTD simulation. (A) SERS Spectra of a face-to-face concave cube dimer functionalized with 1,4-BDT, showing larger SERS intensity from longitudinal (red) than transverse (black) polarization. A 785 nm laser was used for the Raman measurement. The inset SEM image shows the dimer transferred to a silicon substrate for the SERS measurement; scale bar is 100 nm. (B-E) The intensity enhancements  $|E_{\text{local}}/E_{\text{incident}}|^2$  based on FDTD simulation for both longitudinal (B, C) and transverse (D, E)

polarizations at 784.5 incident wavelength. (B, D) are cross sections at the gap centers and  
(C, E) are cross sections at top surface of the cubes (C, E). Intensity data are shown  
logarithmically.....153

## List of Tables

<b>Table 5.1:</b> Parameters of the nanoscale trenches for the alignment of multi-segmented nanowires.....	123
<b>Table 6.1:</b> Spin coating conditions for HSQ resist film.....	144
<b>Table 6.2:</b> Parameters for individual particle alignment.....	145
<b>Table 6.3:</b> Parameters for nanoparticle dimer alignment.....	146

## **Chapter 1 Introduction**

## 1.1 Nanolithography for Materials Science

Nanolithography is a rapidly developing field and one of the most important technological tools, which has significantly impacted the semiconductor industry by the precise delivery of light energy to surface coated with photoresist. The current state-of-art semiconductor manufacturing plants are based on a series of technologies including DUV optics, immersion lithography, high-k materials and 3-D tri-gate transistor, which have pushed the half-pitch (half the distance between identical features) of transistors from 3.2 micrometers (8088 processor, Intel, 1979) down to 22 nm (Haswell processor, Intel, 2012) and will even decrease to 14 nm following Moore's Law.<sup>1</sup> Nanolithography allows the mass production of integrated circuits with billions of transistors on one chip, which are the basic elements for personal computers, cell phones and Internet devices; these advances have undoubtedly changed the world thus introducing society into the information era.

Nanolithography also has revolutionized materials science significantly by allowing researchers to pattern surfaces with various materials. With the development of nanotechnology, it was realized that materials in the size range of 1-100 nm have properties dramatically different from their bulk counterparts because of size, interface and quantum effects. Methods to synthesize materials on the nanoscale are greatly desired for research involving nanomaterials. However, unlike the mass production required in industries, researchers only need a small amount of samples for each new design and proof of concept studies. In addition, because of the

diversity of materials science, nanolithography is required to be compatible with a myriad of material systems including hard oxides, soft materials like polymer and gels, and even biological entities like cells and tissues. In such cases, a swift, low cost technique that can be applied to different material systems but still provides high-throughput and registration is strongly preferred. These requirements motivate the concept of “desktop nanofabrication”, which can be used to rapidly and routinely synthesize nanomaterials in a simple manner. A straightforward desktop nanofabrication tool would dramatically improve the efficiency of research in nanomaterials.

Many efforts have been invested towards achieving desktop nanofabrication, and the developed methods have resulted in a diversity of applications in fields such as electronics, optics, nanomechanics, and nanobiology.<sup>2</sup> Based on following mechanism, these candidate nanolithographic methods can be divided into two main categories. One is parallel printing, which is an analog to pressing a wooden mold on a paper for ink printing, including techniques such as photolithography,<sup>3</sup> nanoimprinting lithography,<sup>4</sup> microcontact printing ( $\mu$ CP),<sup>2</sup> nanosphere lithography<sup>5</sup> and so on. All of these require a prefabricated mask to either optically expose or mechanically deform the underlying substrate, by means of which the pattern on master mask will be directly transferred to the substrates. These parallel methods share the common advantage of high-throughput, which can process a wafer substrate in seconds or minutes. However, the flexibility of these techniques is limited. For each design, a new mask

needs to be fabricated, and the time and financial cost of the mask fabrication can be significant. In the second category, direct-write techniques such as electron-beam lithography,<sup>6</sup> laser writing<sup>7</sup> and scanning probe lithography (SPL),<sup>8-9</sup> rely on serial writing process eg, similar to write on paper with a pen. These techniques have great flexibility to generate arbitrary patterns on a substrate, however they are inherently low throughput, even when multiple “pens” are used.

## 1.2 Scanning Probe Lithographic Techniques

Since the invention of the atomic force microscope (AFM),<sup>10</sup> people have utilized scanning probe lithography (SPL), a technique in which a sharp tip to effect various kinds of surface modifications. SPL can be divided into two main groups, depending on whether energy or materials are delivered from the tip to the substrate.<sup>11</sup> For the energy delivery examples, techniques that employ mechanical scratching,<sup>12</sup> heat,<sup>13</sup> electrical bias,<sup>14</sup> and optical energy<sup>15</sup> have been developed to physically or chemically alter the substrate surfaces.<sup>8, 16</sup> On the other hand, material delivery techniques such as dip-pen nanolithography (DPN) and related molecule printing techniques,<sup>9, 11, 17</sup> directly deposit materials such as alkanethiol molecules,<sup>9</sup> DNA,<sup>18</sup> proteins,<sup>19</sup> polymers<sup>20</sup> and many other molecules on substrates. By using polymers or other molecules as carriers, inorganic materials such as nanoparticles and fullerenes also can be patterned.<sup>21</sup> The patterned molecule monolayer not only can be used as an etch mask for electrodes and photomasks,<sup>22</sup> but also as a template for material assembly,<sup>23</sup> polymer phase separation<sup>24</sup> and even biological applications.<sup>11</sup>

SPLs are generally regarded as low throughput processes because the tip has to serially scan each line across the entire region of interest. Given that the scan range of a typical AFM is less than 100  $\mu\text{m}$ , it can take hours or even days for SPL-based techniques to pattern a square millimeter. An obvious way to improve the throughput of SPL is to utilize multiple tips patterning in parallel. Efforts have been made toward this direction in both energy and material delivery with parallelized and multiplexed cantilever arrays. For example, the Millipede,<sup>25</sup> developed by IBM, has 1024 cantilevers in an array for the delivery of thermal energy. 1-D and 2-D arrays of pens have been used for DPN, with as many as 55,000 cantilevers operating in parallel to deliver molecules simultaneously.<sup>26-28</sup> However, the more cantilevers in a array, the more difficult the fabrication of the array becomes and equivalently, the higher the cost becomes. For instance, each 2-D array can cost more than a thousand dollars, which is a major limitation given that such arrays are very fragile and difficult to operate.

### 1.3 Cantilever-free Scanning Probe Architecture

It turns out that both the advantages and disadvantages of SPL all come from the core component: the cantilever. Is there a way to fundamentally change the architecture of SPL while keeping the advantages of it? In 2008, Huo et al proposed a cantilever-free scanning probe architecture, in which a massively parallel pyramidal pen array made of elastomeric materials on top of a rigid and transparent support was employed to replace the costly and fragile cantilevers. This cantilever-free architecture has opened a new door that enabled SPL to have throughput

comparable to the parallel printing methods and cost low enough for the goal of a “desktop nanofab”.

### 1.3.1 Polymer Pen Lithography

In the first demonstration of the cantilever-free architecture, Huo et al utilized the fabricated massively parallel pen array to directly transport molecules, which was termed polymer pen lithography (PPL).<sup>29</sup> Each PPL pen array has up to 11 million pyramidal pens with average tip diameter of  $80 \pm 10$  nm and can write simultaneously. For a typical experiment, the pen array was brought into contact with a surface and water meniscus formed around the contact area. Alkanethiol molecules diffuse from the tip to surface to form self-assembled monolayers on top of a Au-coated substrate. Because of the diffusion mechanism of ink transport, the feature size is proportional to the square root of the dwell time, which is defined as the time that the pen array remains in contact with the substrate. Besides the time dependence, because of the elastomeric structure, when pushing the pen array harder on the substrate with larger z-piezo extension, the pens deform and generate larger features dependent on the z-piezo extension. Therefore, by means of both time-dependence and z-piezo dependence, features with diameter from the sub-100 nm to tens of micrometers can be generated in a single patterning experiment.

In addition to the delivery of small alkanethiol molecules, PPL has been used to deposit a wide variety of materials including polymers, lipids and proteins. Polymers can be used as the carrier matrices for the delivery of small molecules and nanoparticles as well as serving as a

reaction vessel to direct the synthesis of nanoparticles.<sup>30-35</sup> These nanoparticles were used to assemble patterns of single proteins, which could be used to probe the limits of cell-surface interactions.<sup>36</sup> The unique ability of PPL to apply a controlled pressure during deposition has also been used to drive reactions on a surface, including the Click reaction and Staudinger ligation.<sup>30, 37-38</sup> A meniscus mediated diffusion model has already described the delivery of small molecule inks by PPL,<sup>29</sup> but the transport mechanism of the polymer ink from tip to surface still remains poorly understood.

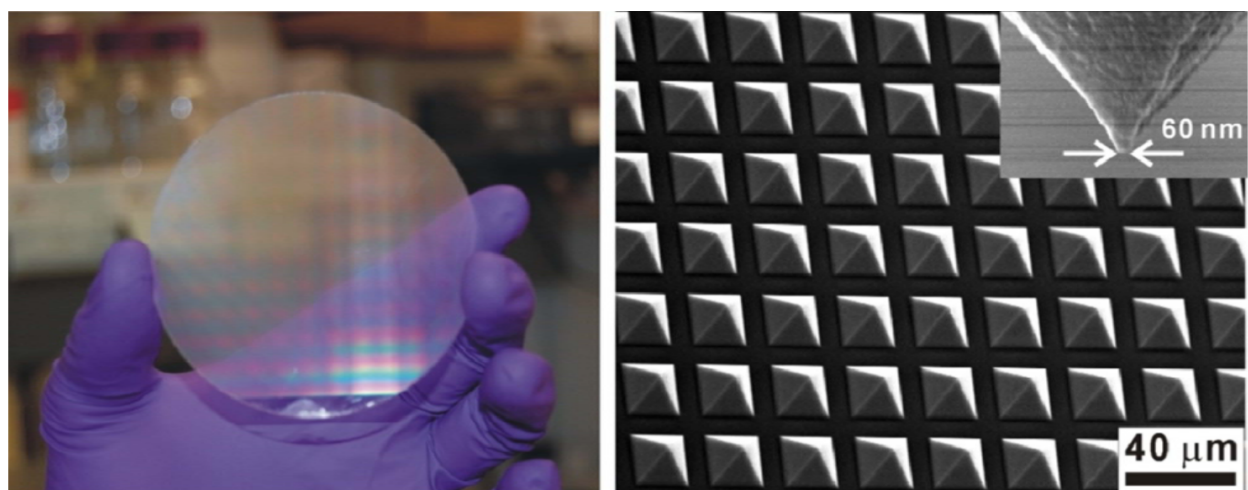


**Figure 1.1** Photographic and scanning electron microscope (SEM) images of a fabricated PPL pen array.

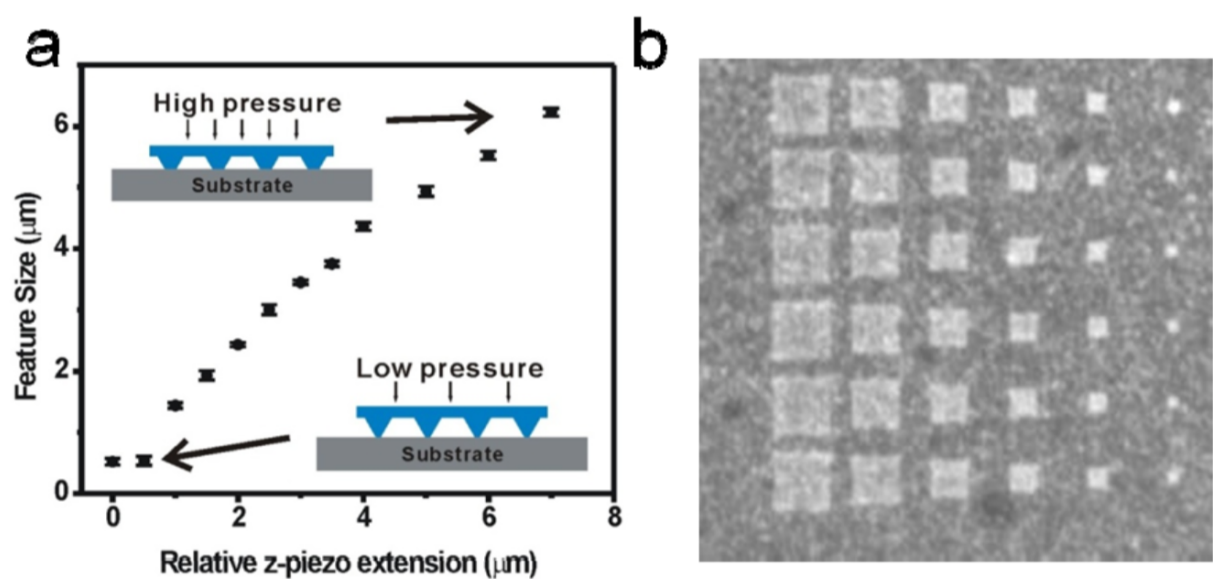


**Figure 1.2** Z-piezo extension of feature size control. a) Schematic image illustrated how low and high pressure on the pen array produce different feature size; b) SEM image of a dot array with different z-piezo extension.

### 1.3.2 Beam Pen Lithography

Shortly after the invention of PPL, Huo et al. extended the cantilever-free architecture to perform near-field optical lithography in parallel, which was termed beam pen lithography (BPL).<sup>39</sup> Sub-wavelength apertures were fabricated by focused-ion beam on top of each pyramidal pen with aperture diameter smaller than 100 nm. The fabricated BPL pen array was brought into contact with a photoresist coated substrate. A beam of UV light was delivered from the back of the BPL pen array, through subwavelength apertures to selectively expose the photoresist just beneath each aperture. Because of the close proximity between the nanometer scale apertures and the substrate, an evanescent wave dominates the process and light intensity decays exponentially away from the edge of the aperture. Features below the diffraction limit can be generated, and with the piezo-controlled stage, arbitrary patterns can be drawn with each BPL pen. This is the first demonstration of scanning near-field lithography with a 2-D parallel pen array.

The method to fabricate the nanometer scale aperture array is a key component of BPL. Although a Focused-Ion Beam (FIB) can provide apertures small enough for near-field lithography, it is a serial writing process, which takes hours to pattern a simple  $5 \times 5$  array. A method to open apertures in parallel was developed by bringing an Au-coated pen array into contact with a poly(methyl methacrylate)-coated substrate.<sup>40</sup> The Au layer at the apex of each pen was mechanically exfoliated from the pen array, leaving apertures on all pens. However, the

need for rigid opaque materials and apertures at the tips of the pens in BPL constrains this technique from fully leveraging the advantages of elastomeric pens with respect to molecular printing and requires a complicated nanofabrication step to open uniform sub-wavelength apertures at the tip of each probe.

In the following chapters, I first investigate the transport of block copolymer inks with various viscosities from the tip to surface, in order to achieve a comprehensive understanding on the transport mechanism of polymeric materials in scanning probe lithography. Further, I explore the optical implications of not having opaque films or apertures at the tip of pens in a cantilever-free pen array, for improving the robustness of the pen array and easy of fabrication. Then, I evaluate the concept of using cantilever-free scanning probe arrays as structures that can modulate nanoscale ink flow and composition with light energy. Finally, I study using lithographically defined templates to assemble anisotropic nanoparticles with control over their angular position by the capillary force-based approach.

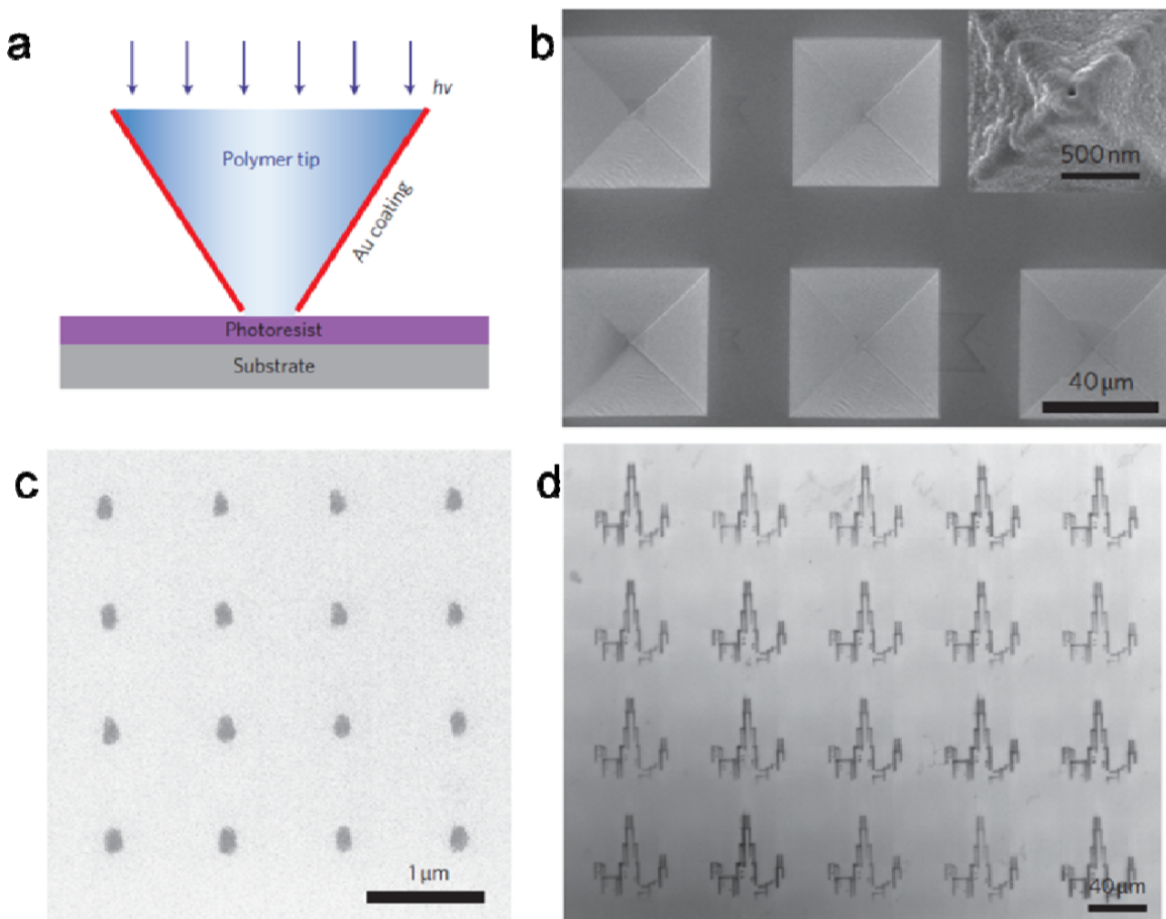


**Figure 1.3** Beam pen lithography. a) Schematic of BPL, where transparent polymer tips are coated with an opaque metal layer (gold) except at the end of the tips. In this way, light only exposes a light-sensitive photoresist-coated surface at the tip. b) SEM image of a FIB fabricated BPL pen array with aperture size smaller than 100 nm; c) SEM image of a chromium dot array created by BPL arrays (after metal evaporation and photoresist lift-off), in which the apertures were fabricated by FIB. Feature diameter is 111+11 nm; d) Optical microscope image of a array of Chicago skyline by BPL

## Chapter 2

# The Role of Polymer Viscosity on Ink Transport in Dip-Pen Nanolithography

Portions of this chapter have been published in: *Chemical Science*, 2013

This work was done in collaboration with Dr. Guoliang Liu

## 2. 1 Introduction

Dip-pen nanolithography (DPN), originally developed as a molecular patterning technique for making features of organic thiols on an Au surface,<sup>9</sup> has rapidly become a versatile tool for making nanostructures on many types of surfaces from a wide variety of materials such as sols,<sup>41</sup> nucleic acids,<sup>18</sup> proteins,<sup>19</sup> phospholipids,<sup>28</sup> collagen,<sup>42</sup> nanoparticles,<sup>43-44</sup> and bacteria.<sup>45-46</sup> Such capabilities have enabled important new applications in chemistry, materials science, and biology.<sup>47-52</sup> Recent additions to the arsenal of DPN inks are block copolymers loaded with metal salts, which, when patterned, can be subsequently reduced to generate individual crystalline nanoparticles through a technique termed scanning probe block copolymer lithography (SPBCL).<sup>53</sup> Initially, this technique was limited to a few highly mobile materials such as Au and CdS,<sup>53-54</sup> but research into the mechanism underlying particle formation has led to a step-wise annealing process that has generalized the method for a large class of nanostructures, including many metals, metal oxides, and metal alloys.<sup>55</sup> However, the mechanistic factors that underlie block copolymer ink transfer from tip to surface during SPBCL have yet to be elucidated. Given the strong relationship in SPBCL between the size of the polymer feature and the size of the resulting nanoparticle, a fundamental investigation of the ink transfer process is critical for a comprehensive understanding of the entire nanoparticle synthetic method, as well as the design of new inks for broader applications.

Previous mechanistic studies into the DPN process have focused extensively on the transfer of small molecules that form self-assembled monolayers.<sup>56-66</sup> A diffusion model in which the ink molecules diffuse from the tip to the surface can explain the meniscus-mediated transfer and patterning of such conventional ink molecules. According to this model, the diameter of a patterned feature scales linearly with the square root of the time the tip dwells at the patterning location, or dwell time.<sup>56</sup> There are two important assumptions in this model: 1) the ink molecules diffuse on the substrate from a point source that has a given molecular flow rate, and 2) the ink molecules are so small that they can diffuse independently and follow a random-walk motion before chemisorption onto the substrate. These assumptions are valid for small molecules such as 16-mercaptophexadecanoic acid (MHA) or 1-octadecanethiol (ODT). In contrast, the block copolymers used in SPBCL have significantly larger molecular weights,<sup>55</sup> and importantly, these chain-like polymer molecules are entangled with one another at the nanometer scale such that they cannot diffuse independently.<sup>67</sup> As a result, the assumption of independent molecular diffusion is not valid, and thus the model is not applicable to block copolymer ink transfer. While chemisorption of the molecules on the surface is a driving force for the transfer of small molecules, block polymer molecules are physisorbed onto surfaces. Therefore, a different transport behavior is expected for this class of materials, leading to questions such as, how are polymer inks transferred from the AFM tip to the substrate, and which parameters govern the transfer of polymer inks from tip to substrate? Examples of patterning polymer melts using

thermal DPN reveal that the polymer flow is affected by the ink viscosity,<sup>57</sup> yet for aqueous polymer solution transport *via* DPN, the effect of viscosity on the ink flow during the patterning process is unknown.

## 2. 2 Experimental Section

### Materials:

Poly(ethylene oxide)-*b*-poly(2-vinyl pyridine) (PEO-*b*-P2VP, M<sub>n</sub>=2.8-*b*-1.5 kg•mol<sup>-1</sup>, polydispersity index, PDI=1.11) was purchased from Polymer Source, Inc. and used as received. Tetrachloroauric(III) acid trihydrate (HAuCl<sub>4</sub>·3H<sub>2</sub>O), hexamethyldisilazane (HMDS) and hexane were purchased from Sigma-Aldrich, Inc., and used as received. DPN® pen arrays (Type M, no gold-coating) were purchased from Nanoink, Inc. Silicon wafers were purchased from Nova Electronic Materials.

### Sample Preparation:

PEO-*b*-P2VP and HAuCl<sub>4</sub>·3H<sub>2</sub>O were dissolved in water, and then mixed with a controlled molar ratio between 2VP and Au from 4 to 64. The final ink had a PEO-*b*-P2VP concentration of 5 mg·mL<sup>-1</sup>. After stirring overnight, the solution was dip-coated onto a DPN® pen array. After drying in an N<sub>2</sub> stream, the pen array was mounted onto an AFM (NScriptor, NanoInk, Inc.) in a chamber with controlled humidity. The relative humidity was in the range of 85%. Prior to DPN patterning, the silicon wafers were kept in a desiccator with two vials of HMDS and hexane mixture for 24 h to ensure that they were hydrophobic. The patterned substrate was placed in a

tube furnace. The annealing conditions were programmed as follows: ramp to 150 °C in 1 h, soak at 150 °C for 4 h in Ar, cool down to room temperature in 1 h, ramp to 500 °C in 1 h, soak at 500 °C for 4 h in Ar, cool down to room temperature in 1 h.

### **Characterization:**

**Dynamic light scattering (DLS):** The hydrodynamic radius of Au loaded block copolymer micelles were measured on a Malvern Zetasizer at room temperature.

**Rheometry:** To approximate the block copolymer inks on the AFM tips during patterning, we measured the viscosity for inks with a relatively high concentration ( $200 \text{ mg}\cdot\text{ml}^{-1}$ ). Viscosities of the polymer inks were measured on a Paar Physica MCR300 viscometer at room temperature. To approximate the conditions at the tip during patterning, the ink concentration used for the viscosity measurement was  $200 \text{ mg}\cdot\text{ml}^{-1}$ .

**Atomic force microscopy (AFM):** The patterned polymer features were analyzed on a Bruker dimension icon with ScanAsyst. The height profiles were exported from Nanoscope. The diameter and height of the polymer nanoreactors were measured directly, and the volume was calculated by integrating the height over area that each polymer nanoreactor spans.

**Scanning electron microscopy (SEM):** The final nanoparticle size was characterized with a Hitachi S-4800 SEM at an acceleration voltage of 5 kV and a current of  $20 \mu\text{A}$ . Probe current was set to high, and focus mode was set to ultrahigh resolution (UHR). Only the upper second

electron detector was used. The measured sizes of nanoparticles were compared and calibrated with those measured with TEM.

**Scanning transmission electron microscopy (STEM):** Hitachi STEM HD-2300A in Z-contrast mode at an acceleration voltage of 200 kV and a current of 78  $\mu\text{A}$  was used to calibrate the size measurement of nanoparticles by SEM. The samples for calibration were patterned on 50-nm-thick hydrophobic silicon nitride membranes.

## 2.3 Results and Discussion

To develop a working mechanism of polymer ink transfer from an AFM tip to a substrate, we first experimentally investigated the patterning of polymer inks with differing viscosities. In the SPBCL process, a block copolymer ink that has been loaded with a metal precursor is deposited onto a surface, and then thermally annealed to remove the polymer matrix while converting the metal precursor into a single nanoparticle. Interestingly, the ink used in the SPBCL process provides a simple way of tuning the polymer ink viscosity, in that the ink viscosity is directly related to the amount of loaded metal precursor.<sup>68</sup> In a typical experiment, the block copolymer poly(ethylene oxide)-*block*-poly(2-vinyl pyridine) (PEO-*b*-P2VP,  $M_n=2.8\text{-}b\text{-}1.5 \text{ kg}\cdot\text{mol}^{-1}$ ) was mixed with the metal salt HAuCl<sub>4</sub>. Inks with different viscosities were prepared by varying the amount of Au loading in the block copolymer ink ( $\alpha$ ), which is defined as the molar ratio between Au and 2-vinyl pyridine in the block copolymer ( $\alpha = [\text{Au}]:[2\text{VP}]$ ). In this work, the inks have Au loadings of  $\alpha = 1:4, 1:8, 1:16, 1:32$ , and  $1:64$ . After dissolution of the

loaded polymer in water above its critical micelle concentration, the block copolymer assembles into micelles (Figure 2.1).<sup>68-69</sup>

We observed that the ink viscosity depends strongly on Au loading (Figure 2.2). For the block copolymer ink with an Au loading of  $\alpha=1:64$  and a polymer concentration of  $200 \text{ mg}\cdot\text{ml}^{-1}$ , the ink is slightly shear thinning and the viscosity plateaus at a shear rate of  $\sim 10 \text{ s}^{-1}$  (Figure 2.2 inset). Importantly, the fact that this ink is shear thinning highlights the inability of the polymer to move independently, supporting the argument that polymeric inks deviate from the conventional molecular diffusion model of DPN transport. To extract viscosity values for comparison, we deliberately use the viscosities in the regime where they are independent of shear rate (Figure 2.2, plateau region). In this regime, the viscosity of the block copolymer ink increases from  $27.0$  to  $45.8 \text{ mPa}\cdot\text{s}$  as  $\alpha$  increases from  $1:64$  to  $1:4$  (Fig. 2.2). As a result of the relatively low molecular weight, the block copolymer forms loose micelles, which interact with one another through weakly intercalated block copolymer molecules.<sup>68</sup> Increasing the amount of  $\text{HAuCl}_4$  enhances the strength of interaction between the micelles via coordination of Au with multiple pyridine groups from different polymer chains,<sup>68, 70</sup> and therefore increases the ink viscosity. Indeed, it is remarkable that the ink viscosity increases 70% by increasing the Au loading in the block copolymer from  $1:64$  to  $1:4$ .

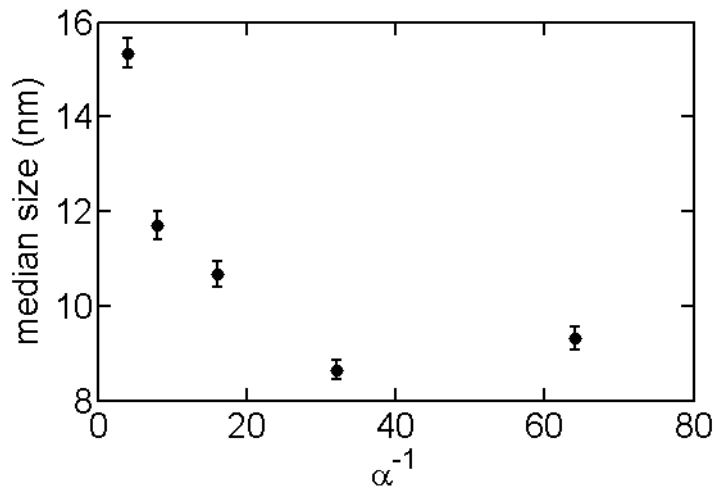


**Figure 2.1** Hydrodynamic radius of the block copolymer micelles measured with dynamic light scattering.

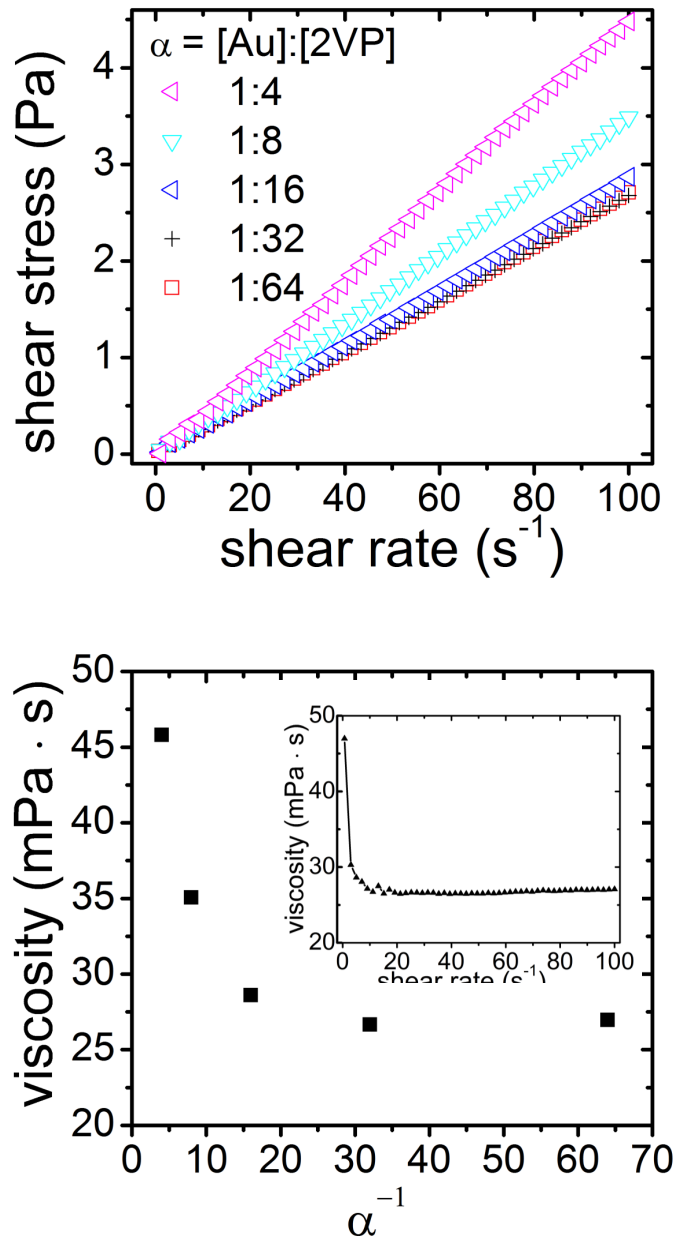


**Figure 2.2** (top) Shear stress as a function of shear rate for block copolymer inks with different Au loading  $\alpha$ . (bottom) Viscosity of polymer inks with various amount of Au loading. The ink viscosity is almost doubled as the Au loading increases from 1:64 to 1:4. (inset) Exemplary viscosity measurement of a block copolymer ink with Au loading of 1:64. The viscosity reaches a plateau at high shear rates and the ink shows shear thinning behavior.

Block copolymer inks with different viscosities behave differently during patterning. Using DPN, the aforementioned polymer inks were patterned on hydrophobic silicon substrates to generate nanoreactors for synthesizing nanoparticles; feature size was controlled by varying dwell time (Figure 2.3). The patterned block copolymer feature sizes (both diameter and volume) were quantified by AFM and SEM and plotted as a function of dwell time (Figure 2.4). In general, the block copolymer feature size increases with increasing dwell time and decreasing ink viscosity. From 0.01 to 1 s, the patterned block copolymer feature size increases rapidly, but exhibits a markedly decreased rate of growth from 1 to 10 s. When  $\alpha$  is decreased from 1:4 to 1:16, the feature size is significantly increased for a given dwell time (for example, 0.01 s in Figure 2.5a). Increasing  $\alpha$  further to 1:32 and 1:64 does not yield faster rates of deposition because the viscosities of the polymer inks are comparable in the  $\alpha$  range from 1:16 to 1:64 (Figure 2.2). It is also important to note that the feature size does not scale linearly with square root of time over the entire dwell time range, confirming that the diffusion model is not applicable to the polymer inks.

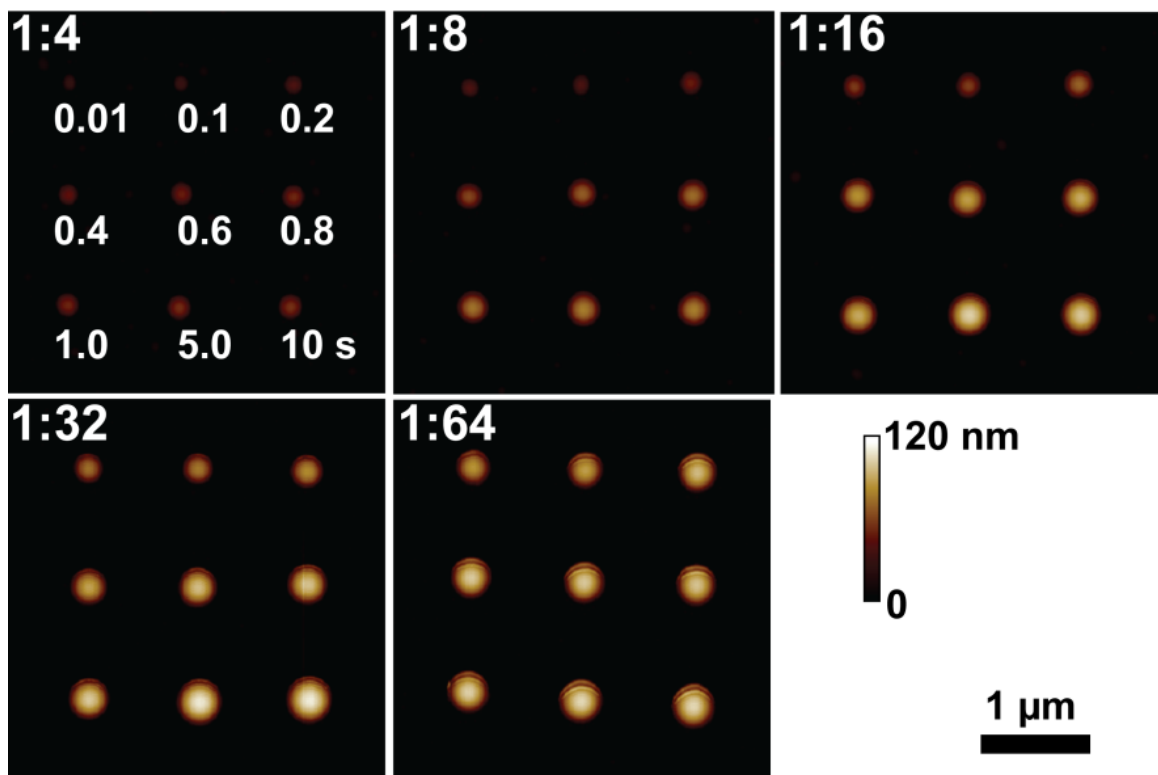


**Figure 2.3** AFM height images of the patterned polymer features from different inks. The Au loading,  $\alpha$ , ranges from 1:4 to 1:64, and the patterning dwell time ranges from 0.01 to 10 s. The dwell time sequence and scale bars apply to all AFM images.

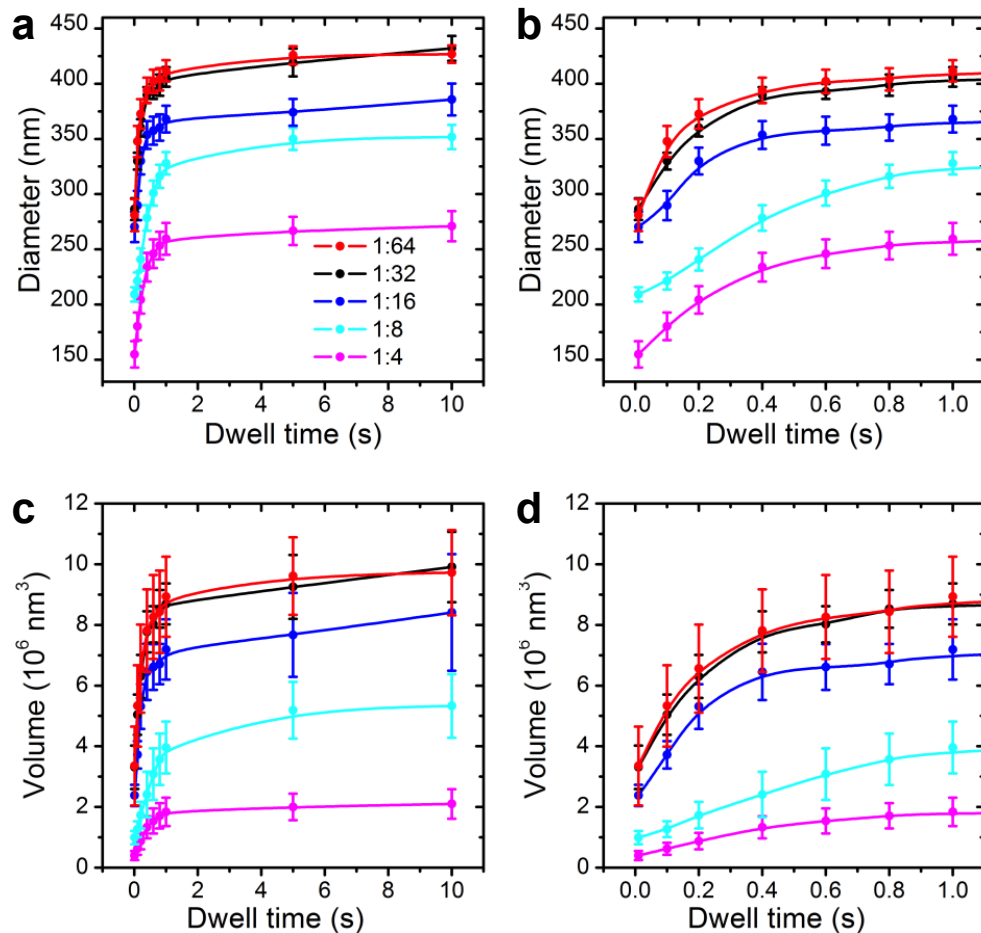


**Figure 2.4** (a, b) Diameter and (c, d) volume of patterned polymer features as a function of dwell time and Au loading. (b) and (d) are expanded views of (a) and (c) at lower dwell times, respectively. Solid lines are a guide to the eye.

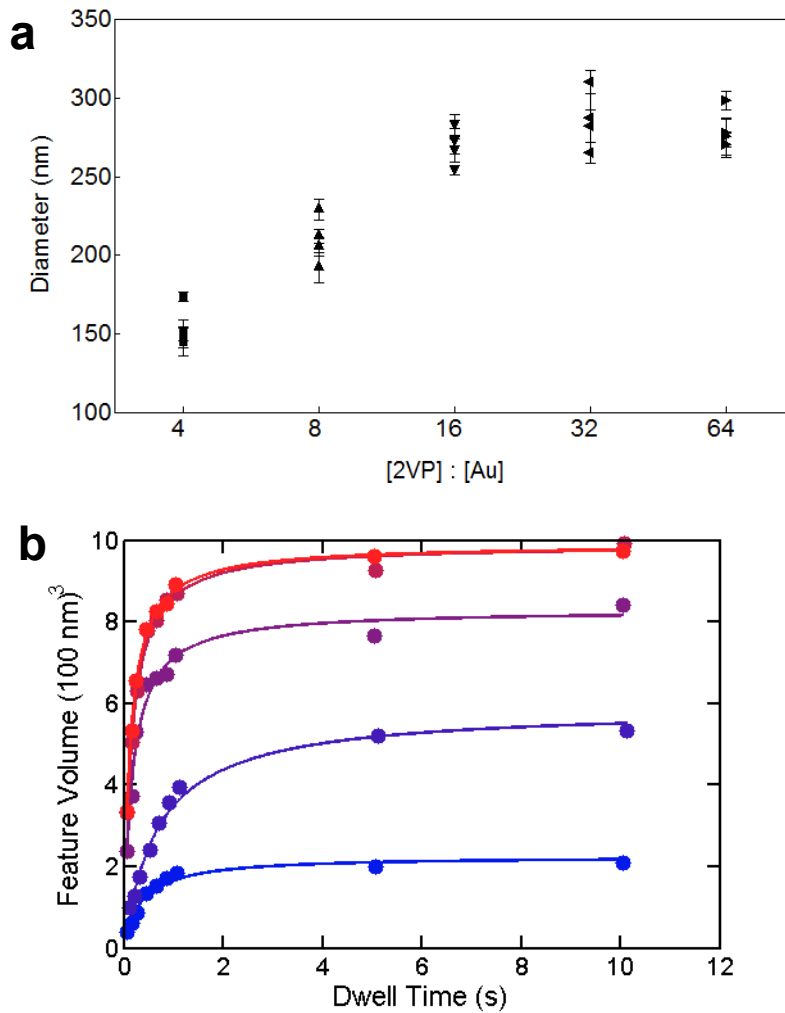


**Figure 2.5** (a) Diameter of the patterned block copolymer features with the same dwell time of 0.01 S as a function of Au loading. The four points are from four different pens. (b) Fitting of polymer feature volume as a function of dwell time. Error bars are omitted for clarity.

To describe the observed behavior of polymer ink transfer from an AFM tip to a substrate, we propose a mass transfer model that calculates the amount of ink that transports across any horizontal cross-section near the end of AFM tip (Figure 2.6a and b). For simplicity, we adopt a cylindrical approximation of an AFM tip<sup>57</sup> that has a tip radius of  $R_1$ . In this model, the tip was coated with a polymer layer, and we assume that the thickness of this ink layer does not change during an experiment as there is a reservoir of ink from the cantilever at the top of the AFM tip. We define the thickness of polymer ink as  $R_2 - R_1$ . Given that the water-based ink used here is nearly a Newtonian fluid (the shear stress appears linearly with respect to shear rate, and it intersects at zero) under our experimental conditions (Figure 2.5b), and inertial effects are negligible because of the extremely low Reynolds number in this system,<sup>57</sup> the polymer velocity profile on the AFM tip can be approximated by the Stokes equations,

$$0 = -\nabla p + \mu \nabla^2 v + \rho g \quad (1)$$

where  $v$ ,  $\nabla p$ ,  $\mu$ ,  $\rho$  and  $g$  are, respectively, velocity of ink flow, pressure gradient along the tip, ink viscosity, ink density, and gravity. Since there is no radial or angular flow ( $v_r = 0$  and  $v_\varphi = 0$ ), the equation can be simplified to,

$$\nabla^2 v_z = \frac{F}{\mu} \quad (2)$$

where  $F = \rho g - \nabla p$ . Since the final volume of polymer ink that is delivered onto the substrate is an integration of ink velocity with respect to time and cross-section area, it should also be

inversely proportional to the ink viscosity. In addition, the pressure gradient  $\nabla p$  depends upon the surface energy of the ink materials, as well as the shape of the polymer features on the substrate. As shown in previous work,<sup>57</sup> the pressure gradient is proportional to the curvature difference between the polymers at the top and bottom of the tip. The curvature of polymer at the top of the tip is zero, and at the bottom the curvature is determined by the polymer feature size whose curvature decreases with dwell time. Based on this model, we expect that: 1) given the same dwell time, a more viscous ink results in smaller patterned polymer features; 2) given the same ink viscosity, the feature size increases with dwell time, but the ink transfer rate decreases with dwell time. The projected profile of polymer volume as a function of dwell time and viscosity is schematically shown in Figure 2.6d. Indeed, our measured data confirm that the relationships between feature size, dwell time, and ink viscosity (Figure 2.4) are in agreement with the mass transfer model.

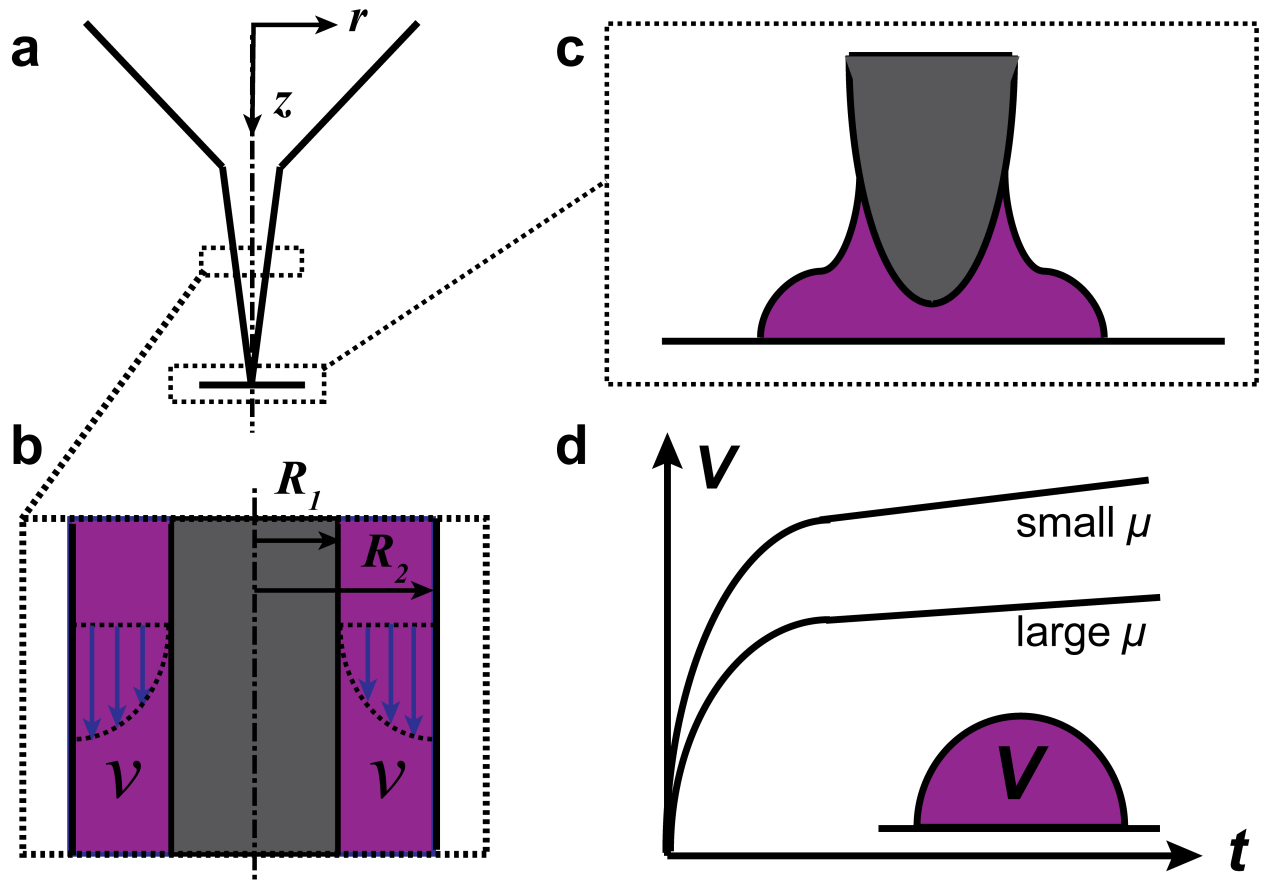


**Figure 2.6** Schematic of mass transfer during DPN patterning of an aqueous polymer ink. **a**, An AFM tip with defined cylindrical coordinates. **b**, Profile of the ink velocity ( $v$ ) across a horizontal thin slab. The tip diameter is  $R_1$ , and the thickness of polymer ink layer is  $R_2-R_1$ . **c**, The polymer ink transfers from the tip to a hydrophobic substrate through a meniscus. **d**, The final volume ( $V$ ) of the patterned polymer features as a function of dwell time ( $t$ ) and ink viscosity ( $\mu$ ).

We further explored the utility of these polymer features to synthesize single nanoparticles of various sizes by analyzing the size of the nanoparticles as a function of polymer feature size. Following the protocol of polymer-mediated synthesis of nanoparticles,<sup>55</sup> the patterned block copolymer features were annealed stepwise at 150 °C for 4 h and at 500 °C for 4 h under an Ar atmosphere. SEM image of an array of Au nanoparticles formed from a block copolymer ink with an Au loading  $\alpha = 1:4$  confirms that the size of the synthesized nanoparticles increases with dwell time (Figure 2.7).

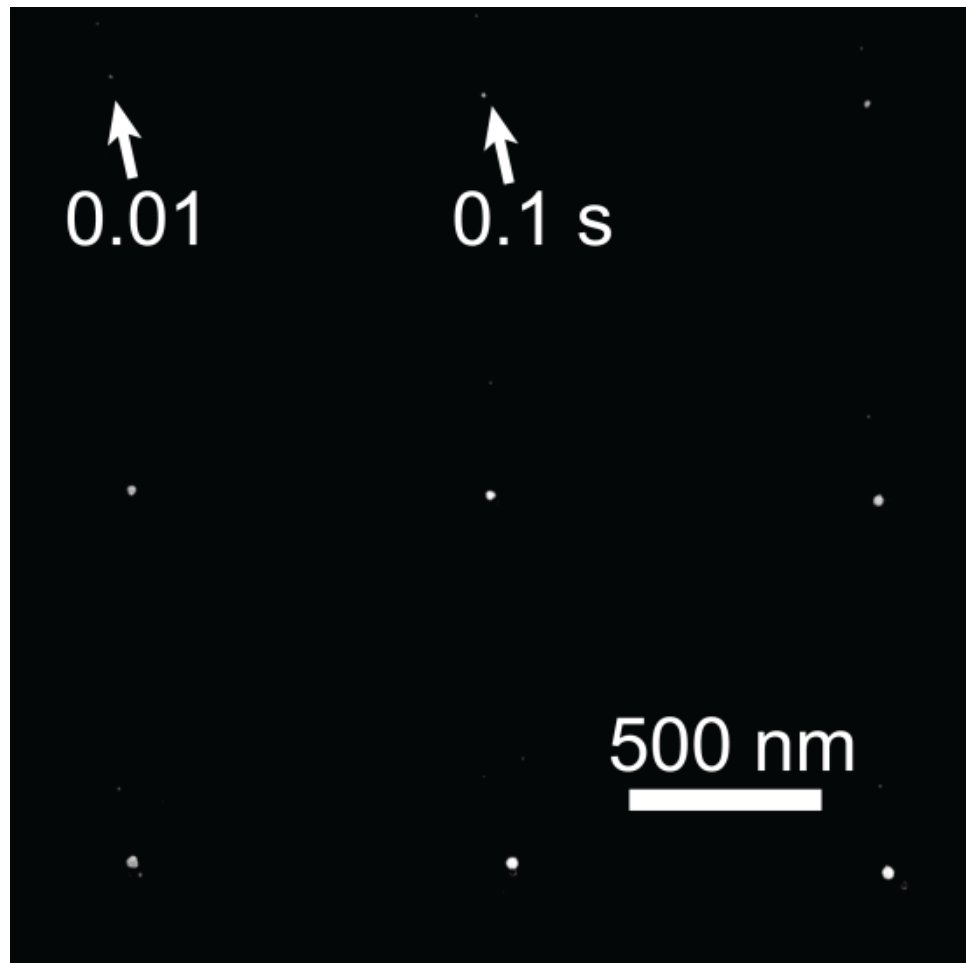


**Figure 2.7** SEM image of nanoparticles synthesized within patterned polymer nanoreactors with various dwell times. The Au loading  $\alpha$  in the ink is 1:4. The dwell time follows the same sequence as that in Fig 3. For clarity, only the first two dwell times are shown.

The nanoparticle size is a function of the polymer feature size and the metal salt concentration (Figure 2.8). For patterned polymer features with the same diameter, the size of the nanoparticles increases as the Au loading increases. In principle, the nanoparticle size should be governed by the number of Au atoms,  $N_{Au\ atom}$ , in the patterned block copolymer nanoreactor or in the synthesized nanoparticle,

$$N_{Au\ atom} = \frac{\rho_p V_p}{M_{w,p}} N_A N_{2VP} \alpha = \frac{\rho_g V_g}{M_{w,g}} N_A \quad (4)$$

in which  $\rho$ ,  $V$ ,  $M_w$ ,  $N_A$ ,  $N_{2VP}$  are density, volume, molecular weight, Avogadro number, and number of 2VP monomers in one block copolymer chain, respectively. The subscripts  $p$  and  $g$  denote polymer and gold nanoparticle, respectively. Since  $V_p \propto D^3$ , and  $V_g \propto d^3$ , where  $D$  and  $d$  are diameters of the polymer feature and nanoparticles, the diameters of the nanoparticle and the block copolymer feature should scale as

$$d/D \propto \sqrt[3]{\alpha} \quad (5)$$

Therefore, we linearly fit the diameter of nanoparticle with respect to the diameter of the block copolymer features. The slopes of the fitted lines follow the above scaling law, as shown in Figure 2.8.

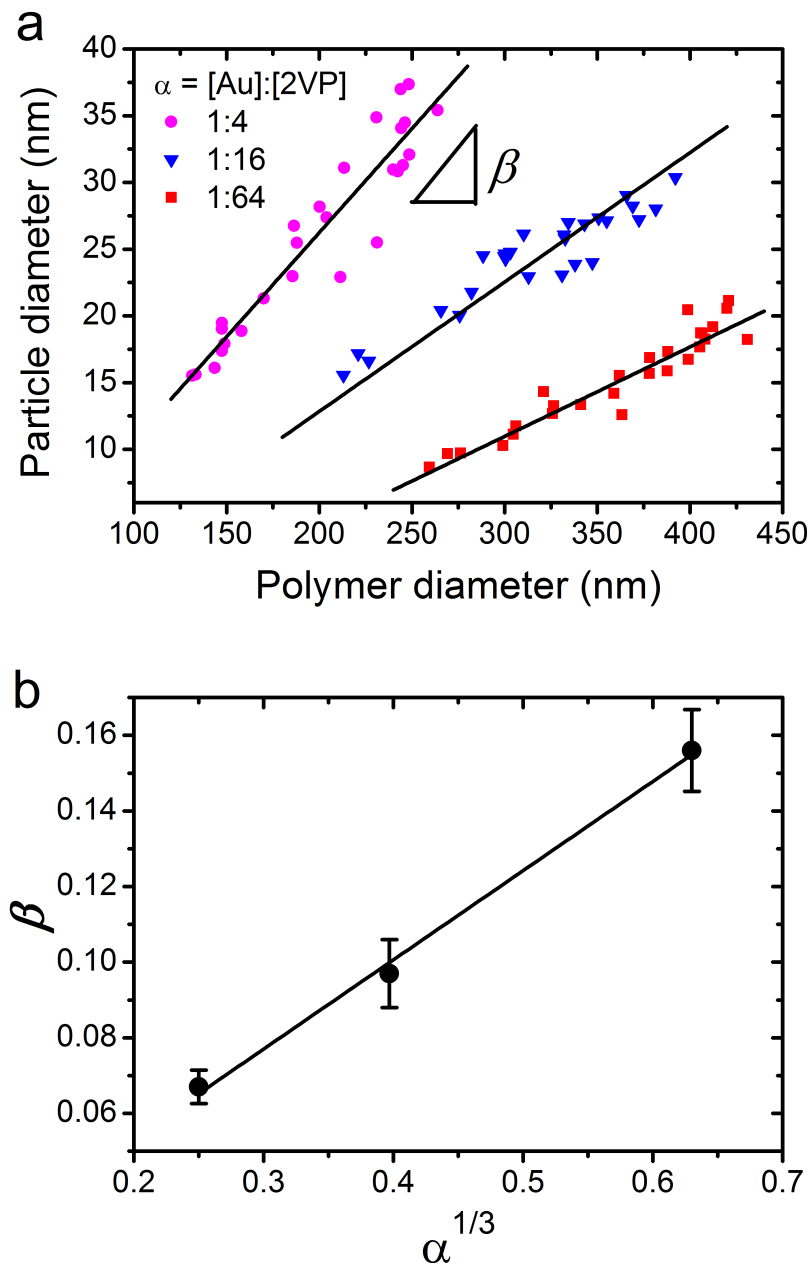


**Figure 2.8** The scaling behavior of nanoparticle size. **a**, Diameter of Au nanoparticles in polymer nanoreactors. The nanoparticle size scales linearly with the size of polymer nanoreactors. **b**, The slope ( $\beta$ ) of the fitted lines in (a) scales linearly with  $\sqrt[3]{\alpha}$ .

## 2.4 Conclusions

We have found that viscosity plays a major role in ink transfer during DPN. A slight increase of Au loading in the block copolymer remarkably increases the ink viscosity, rendering significantly different transfer properties during the patterning process. A mass transport model is developed to describe the patterning of block copolymer inks. In contrast with the conventional diffusion model, in which diffusivity plays a major role in small molecule ink transfer, here the mass transport model highlights viscosity as an important parameter to control the patterning of large molecule inks. The patterned block copolymer features can further serve as nanoreactors for nanoparticle synthesis. The extracted relationship between nanoparticle size and patterning time as well as metal salt loading can guide the synthesis of nanoparticles with desired size on a surface for extended applications in catalysis, plasmonics, and nanolithography. Given that viscosity is a generic material property, this study should also offer insights into patterning other advanced materials for the assembly of sophisticated nanostructures.<sup>45, 71-75</sup>

## Chapter 3

# **Apertureless Cantilever-Free Pen Arrays for Scanning Photochemical Printing**

Portions of this chapter have been published in: *Small, 2015*

This work was done in collaboration with Dr. Zhuang Xie

### 3.1 Introduction

There are two categorically different approaches for defining patterns on surfaces, those based on the delivery of energy and those based on the delivery of materials.<sup>11, 76-78</sup> The delivery of energy is the mainstay of the microelectronics community while the delivery of materials is commonly used in biological contexts where the materials of interest are chemically diverse and sensitive to harsh processing conditions. One recently developed set of techniques that spans this divide is cantilever-free scanning probe lithography (SPL) wherein materials or energy are deposited from an array of pens that rest on an elastomeric film on a rigid support.<sup>35, 39, 79-84</sup> This architecture affords the high resolution commonly observed in SPL in combination with high throughput by virtue of the simultaneous operation of as many as millions of pens. Given the widespread usage of energy delivery techniques, beam pen lithography (BPL), in which cantilever-free pens can be used as near-field probes to direct light onto surfaces in a massively parallel and multiplexed fashion, has aroused broad interest in low cost desktop nanofabrication and site-selective photochemistry.<sup>39, 85-86</sup> However, the need for rigid opaque materials and apertures at the tips of the pens in BPL constrains this technique from fully leveraging the advantages inherent to elastomeric pens with respect to molecular printing and necessitates a complicated nanofabrication step to open uniform sub-wavelength apertures at the tip of each probe. Here, we explore the optical implications of not having opaque films or apertures at the tip of pens in a cantilever-free pen array and find that by blocking the flat backing layer between

pens, the optical interaction with the surface is dominated by the light at the tip of the pen, allowing one to serially write sub-wavelength features. Furthermore, the absence of a rigid metal film coating the pens, we find that they can be reversibly deformed to tune the illumination region from the submicrometer to micrometer scale and used to simultaneously deliver materials and optical energy in a single experiment. This approach provides a route to multiplexing with respect to length scales and materials.

While it is straightforward to fabricate cantilever-free pen arrays composed of elastomeric pyramids, it has been assumed that opening an aperture on the pyramid tip is required for high-resolution patterning in BPL.<sup>39, 85-88</sup> Following the original demonstration of BPL,<sup>39</sup> several groups developed methods of fabricating aperture arrays based on metal<sup>85, 87</sup> and carbon black<sup>88</sup> opaque layers. However, from a practical standpoint, requiring apertures is a challenge as this is the part of the pen array fabrication process that is most sensitive to processing conditions and can result in non-uniform apertures. Although near-field photolithography has also been demonstrated using pyramid arrays coated uniformly with chromium,<sup>88</sup> these predominantly opaque pen arrays have limited utility for the delivery of materials as the rigid metal coatings physically block the elastomer and cannot be reversibly deformed, properties that diminish the use of elastomeric tip as ink reservoir to mediate molecular patterning<sup>89</sup> and prevent one from toggling ink transport by altering contact force,<sup>38, 80, 90-91</sup> respectively. Therefore, the only demonstration of aperture-based BPL for patterning materials and light involves matrix-assisted

deposition of materials and far-field light illumination in sequential steps.<sup>86</sup> Interestingly, one can question the need for an opaque film on the pen as early work by the Whitesides' group has shown that transparent polydimethylsiloxane (PDMS) pyramids can support total internal reflection on the faces of such pyramids, which in some cases can lead to light being directed out the top surface of the pyramid array.<sup>92-93</sup> Based on these observations, we hypothesized that cantilever-free scanning probe arrays with no opaque coatings on the pyramidal pens can simultaneously and effectively deliver optical energy and materials, which could enable one to control surface reactions with combined approaches based on light, contact force, and material transfer.

### 3.2 Experimental Section

**Fabrication of Apertureless Pen Arrays.** Polymer pen array made of hard polydimethylsiloxane (*h*-PDMS) was treated with O<sub>2</sub> plasma at 150 mTorr and 45 W for 1 min. Next, an opaque coating of 5 nm Ti and 200 nm Au was evaporated onto the pen array using an electron-beam evaporation system (Kurt J. Lesker Co., USA). To expose the transparent pyramidal tips, poly(methyl methacrylate) (PMMA950 A3, MicroChem Inc., USA) was spin-coated onto the tip array at 1000 rpm for 45 s followed by baking at 100 °C for 10 min. The PMMA coating was repeated for one more time to ensure complete coverage. Finally the pen array was immersed in a Au etching solution (Gold Etchant TFA, Transense Company Inc., USA) for 70 s followed by Ti etching (Titanium Etchant TFT, Transense Company Inc., USA)

for 5 s to remove the metal coatings on the pyramids while maintaining the backplane between pens opaque.

**Lithography Procedure.** Typically, an n-type <100> silicon wafer was spin-coated with a 450 nm thick layer of positive photoresist (Shipley1805, MicroChem Inc., USA) at 4000 rpm for 45 s followed by soft-baking on a hot plate at 115°C for 1 min. For lift-off processing, a layer of lift-off resist (LOR 1A, MicroChem Inc., USA) was spin-coated at 4000 rpm for 45 s and then baked at 180 °C for 5 min. Subsequently, the pattern resist was spin-coated using a pre-diluted photoresist solution with propylene glycol monomethyl ether acetate (MicroChem Inc., USA) at 1:1 v/v for 100 nm thick layers and 1:3 v/v for 40 nm thick layers. Apertureless pen arrays were mounted onto a BPL apparatus and leveled to the photoresist-coated substrates optically. Patterns were generated under the control of piezoelectric actuators of a scanning probe platform (XE150, Park Systems) and a commercial digital micromirror device (DMD – DLP LightCommander, Logic PD) coupled with a collimated 440 mW 405 nm LED light source (M405L2, Thor Labs USA) to allow the exposure time between 1 and 10 s. After patterning, the photoresist was developed in MF24A (MicroChem Inc. USA) for 20-30 s and rinsed with DI water. A layer of 2 nm Cr and 10 nm Au was evaporated onto the developed samples followed by etching of polymer resist in Remover PG (MicroChem Inc., USA) overnight. Patterns of photoresist and metals were characterized using optical microscopy (Axiovert-Zeiss), atomic force microscopy (Dimension Icon, Bruker), and scanning electron microscopy (S-4800-II, Hitachi).

**Photochemical Printing.** The ink for photochemical patterning was prepared by mixing Rhodamine-modified thiol ( $1 \text{ mg mL}^{-1}$ ), photoinitiator 2,2-dimethoxy-2-phenylacetophenone ( $0.3 \text{ mg mL}^{-1}$ ) and glycerol ( $50 \text{ mg mL}^{-1}$ ) in ethanol. Then the ink was spin coated onto the plasma-treated pen array (2000 rpm, 30 s). The piranha-washed Si wafers were immersed into the solution of 10-undecenyl trichlorosilane (1% v/v in toluene) for 2 h to form an alkene-terminated surface. The inked tip array was mounted onto the scanning head, leveled and brought into contact with the alkene-modified substrate under simultaneous UV illumination (365 nm,  $150\text{-}200 \text{ mW cm}^{-2}$ ) from Hg lamp, with illumination time ranging from 1 to 4 min. After patterning, the substrate was sonicated in ethanol for 30 min and blow dried with nitrogen. Patterns were characterized using fluorescence microscopy ( $\lambda_{\text{ex}} = 537\text{-}562 \text{ nm}$ ,  $\lambda_{\text{em}} = 570\text{-}640 \text{ nm}$ ).

**Simulations.** Ray tracing simulations of light normally incident on a pen array was conducted using Persistence of Vision Raytracer Pty. Ltd. Finite-difference time-domain (FDTD) simulations were performed with a commercial package (Lumerical FDTD solutions v.8.7.0). The refractive indices of photoresist and PDMS pyramid were assumed to be 1.66 and 1.43. FDTD was run with purely pyramid structures. Due to the computation limitation, the pyramid size in the simulation was reduced to  $8 \mu\text{m}$ . Perfectly Matched Layers (PML) boundary condition was used to absorb the electromagnetic fields at the simulation boundary. The Total Field Scattered Field (TFSF) plane wave source was used to avoid the light interaction with simulation

boundary. The light polarization was paralleled to the edge of the pyramid. The spectral profile of the light source (LED) was addressed by averaging the intensity profiles over spectral range of the light source with the spectral line shape as the weighting factor.

### 3.3 Results and Discussion

In order to explore the optics for serial writing with apertureless pens, we considered the paths through which light can propagate through an elastomeric pyramid. In observing an elastomeric pyramid from the top, it is clear from the varying contrast in different regions that light incident on different areas is directed in different ways (Figure 3.1A). Through ray tracing simulations of light normally incident on a pen array (Persistence of Vision Raytracer Pty. Ltd.), we determined that there are four distinct optical paths that may play a role in BPL (Figure 3.1A): a) light that is directed to the vicinity of the tip, b) light that is incident on flat faces of the pyramid near their centers, c) light that is incident on the flat faces of the pyramids near their edges, and d) light that is incident on the flat backing layer. The central requirement for effective BPL is that the light path a) dominates the delivery of optical energy to the surface. In order for this to be true, all other light paths must be somehow marginalized. Fortunately, the light path b) internally reflects once in the pen and then leaves via the opposing face at a 24° angle with respect to the surface. This steep angle serves to diffuse this light broadly across the photosensitive surface. In contrast, the light path c), which accounts for ~40% of the light illuminating the pyramid, internally reflects twice in the pen and then leaves via the opposing

face at a 2° angle, moving vertically away from the photosensitive surface. Finally, the light path d) is directly transmitted to the photosensitive surface. Since light of this kind would represent an uncontrolled background illumination, it must be blocked for reliable scanning optical lithography to occur. These optical calculations led us to hypothesize that by simply blocking the flat backing layer (light path d), we may effectively deliver optical energy predominately at the apex of an apertureless pen by virtue of the self-light-focusing nature of the PDMS pyramid.

Based on this principle, we fabricated cantilever-free pen arrays with an opaque coating on the backing layer, but not on the sidewalls of the pyramidal pens (Figure 3.1B). Notably, this procedure is significantly less complex than known procedures that produce apertures. Hard PDMS arrays of pyramids with 30 μm base widths and 100 μm pitch were produced according to previously published protocols. In order to render the backing layer opaque, pen arrays were coated with 5 nm Ti/200 nm Au and subsequently spin-coated with a protective layer of PMMA. Importantly, we found that at specified PMMA concentrations and spin speeds, the PMMA coated the backing layer but not the pens themselves, allowing us to use chemical etching to remove the opaque coating on the pyramidal pens (Figure 3.1B and C, see experimental details in Section 5.2).

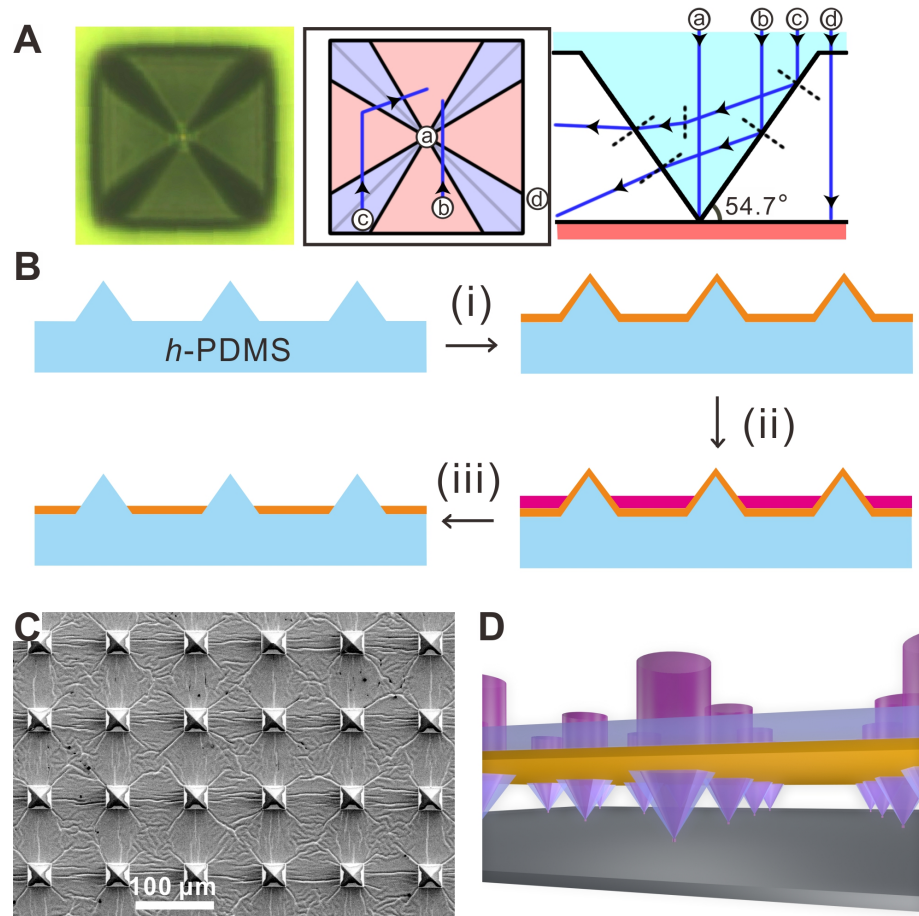


**Figure 3.1** Principles and fabrication of apertureless cantilever-free pen arrays. (A) Optical microscope image and schematic illustration showing the four light paths present when elastomeric pyramids are illuminated. These suggest that if the light incident on the back layer could be blocked, light at the tip of the pen will dominate the optical interaction with the surface. (B) Schematic of the fabrication of the apertureless BPL pen arrays: (i) evaporation of 5 nm Ti and 200 nm Au on hard polydimethylsiloxane (*h*-PDMS) pen arrays; (ii) spin coating of PMMA that only covers flat region of the pen array; (iii) chemical etching of metal layer followed by removal of PMMA. (C) Scanning electron microscopy (SEM) image of the as-fabricated apertureless pen arrays. (D) Schematic of scanning optical lithography using the apertureless cantilever-free pen arrays.

In order to quantify the propagation of light through the self-light-focusing tips, we performed lithography experiments on polymer photoresist. The apertureless elastomer pen array was mounted on a scanning probe system (XE150, Park Systems) and leveled with respect to a patterning substrate pre-coated with a 450-nm-thick positive-tone photoresist. Subsequently, the pen array was brought into contact with the surface and illuminated from the back side for a specified time ( $\lambda = 405$  nm). The light was guided to individual pens using a digital micromirror device.<sup>85</sup> Importantly, this apparatus allowed us to independently control the location of the pen array, contact pressure, and illumination time. Following exposure to light, treating the photoresist with a developer caused the photoresist that had been exposed to dissolve, effectively leaving a physical remnant of the light intensity profile. As an initial experiment, we exposed a 7  $\times$  3 dot array with 5  $\mu\text{m}$  pitch to 4 s of light with a relative Z-piezo extension ( $Z_{ext}$ ) that gradually increased from 0 to 6  $\mu\text{m}$  in each row. After developing the photoresist, we observed a large region of uniform duplicates of this dot array pattern, and the background areas without contacting with the tips were unexposed, in agreement with our expectation that each pen in the 20, 000 pen array would generate a copy of the pattern (Figure 3.2A). The nanoscale morphologies of the features in these patterns were characterized by atomic force microscopy (Figure 3.2B). As  $Z_{ext}$  was increased from 0 to 1  $\mu\text{m}$ , the size and shape of the exposed region did not change significantly and the developed regions corresponded to roughly circular holes  $\sim$ 400 nm in width (full width at half maximum) with maximum depths of  $\sim$ 200 nm, indicating no

significant tip deformation owing to the buffering of the soft bulk PDMS layer.<sup>80</sup> It should be also noted that as the tip was slightly elevated for 0.5-1  $\mu\text{m}$ , holes with similar size and shape were still formed, but the depth was only less than half of those written at initial contact. The depth difference can be attributed to less energy loss in the near-field regime upon tip contact due to lack of scattering/reflection at the interfaces created by air gap. These observations prove that the light self-focused on the tip apex (optical paths a) dominates the optical interaction with the photoresist surface and that light exiting through the faces (optical paths b and c) does not contribute significantly to the light intensity on the patterning surface.

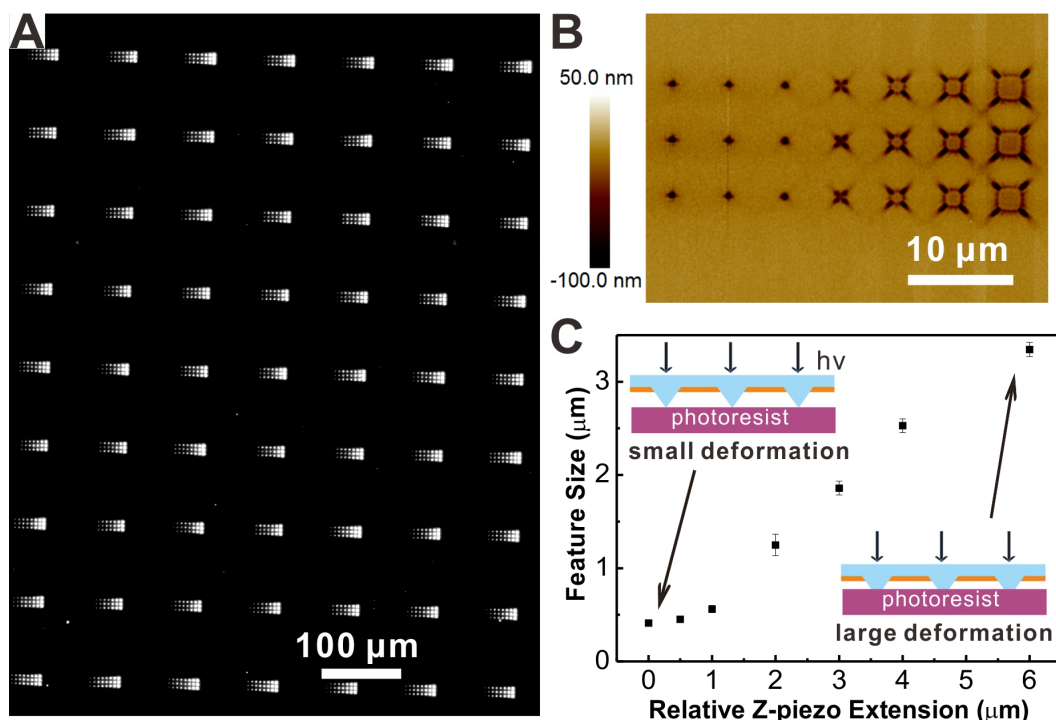


**Figure 3.2** Force dependence in photoresist patterns generated with an apertureless cantilever-free pen array. (A) Dark field optical microscope image of a large region of developed photoresist patterns. Each  $7 \times 3$  array of dots is written by a single pen under same exposure dose but with a z-piezo extension that increases from left to right. (B) Tapping-mode AFM image of a typical dot array showing the change in size and shape with increasing z-piezo extension from left to right. (C) Average size of features written at varying z-piezo extension.

In molecular printing with elastomeric pens, the force-dependent patterning with an extension sweep has been extensively studied.<sup>80, 91</sup> While a metal-coated BPL pen array cannot be compressed without plastic deformation of the metal, since the apertureless pens are composed entirely of an elastomer, the reversible tip deformability can give rise to a variable amount of optical energy delivered to the surface. Specifically, by increasing  $Z_{ext}$  from 1 to 6  $\mu\text{m}$ , the shapes of the exposed feature were found to change from round dots to squares with the four protruding corners. The reversible change in feature size (the rows were written one at a time) illustrates that applied pressure can dictate the region that is exposed to light. It is important to note that this result is in contrast with aperture-based BPL where features larger than a micron take prohibitively long to pattern due to the rapid decay of near-field light. Rather than being restricted to a fixed aperture, the elastomeric pens are effectively behaving as having variable apertures as defined by refractive optics.<sup>92-93</sup> The feature size of these protruding squares increased from  $0.56 \pm 0.04 \mu\text{m}$  to  $3.35 \pm 0.07 \mu\text{m}$  as a linear function of  $Z_{ext}$ , showing the similar force dependence as that in PPL (Figure 3.2C). Interestingly, the light intensity was observed to have uneven distribution, where the central area is much less affected compared with the corner and edge areas of the square shape and the four corners exhibit the highest depth value. The observation can be analogous with the molecular printing results in PPL, and the elastic deformation of tip is believed as the main cause.

The exposure time was also investigated to tuning the patterned features. A series of  $4 \times 2$  dot arrays were fabricated with exposure time varying from 1 s to 10 s, while increasing  $Z_{\text{ext}}$  from 0 to 6  $\mu\text{m}$  in each array (Figure 3.3A-C). For those dot features written at initial contact, the feature size presented a linear increase with the exposure time from  $294 \pm 35$  nm to  $840 \pm 33$  nm (Figure 3.3D). Interestingly, at short exposure time, light focusing on the tip apex resulted in deep penetration in the dot features, while the intensity is distracted to four corners and most of the central regions within the square-shaped tip contact area maintained undeveloped. As exposure time prolongs, the corner, edge and central regions of the square patterns were sequentially filled with minimal loss of optical confinement. The increased aperture area has caused increased dosage delivered to the resist. We used the photoresist depth profile to estimate the irradiation dose. The volume of the developed photoresist shows a linear increase as the degree of tip deformation increases after 10 s exposure (Figure 3.3E), indicating the increase in the total irradiation dosage on the surface, which is in accordance with previous report. Furthermore, through the linear function between the fraction of photoresist remaining thickness and the exposure time (Figure 3.3F) and assumption that the dose is  $50 \text{ mJ/cm}^2$  at fraction=0, we calculated the time for totally expose a 500-nm S1805 photoresist and the optical intensity in the center as 3.3, 4.4, 1.5, 1.5  $\text{mW/cm}^2$  for  $Z_{\text{ext}}=0, 2, 4$ , and  $6 \mu\text{m}$ , respectively. Although the tip shows enhanced intensity at small deformation, these square features at high deformation could still be reliably used for lithography. The maximum depth generated in each features were

plotted with exposure time and  $Z_{ext}$  (Figure 3.3G) to provide a guidance to adjust the contact force, exposure time and photoresist thickness for lift-off process.

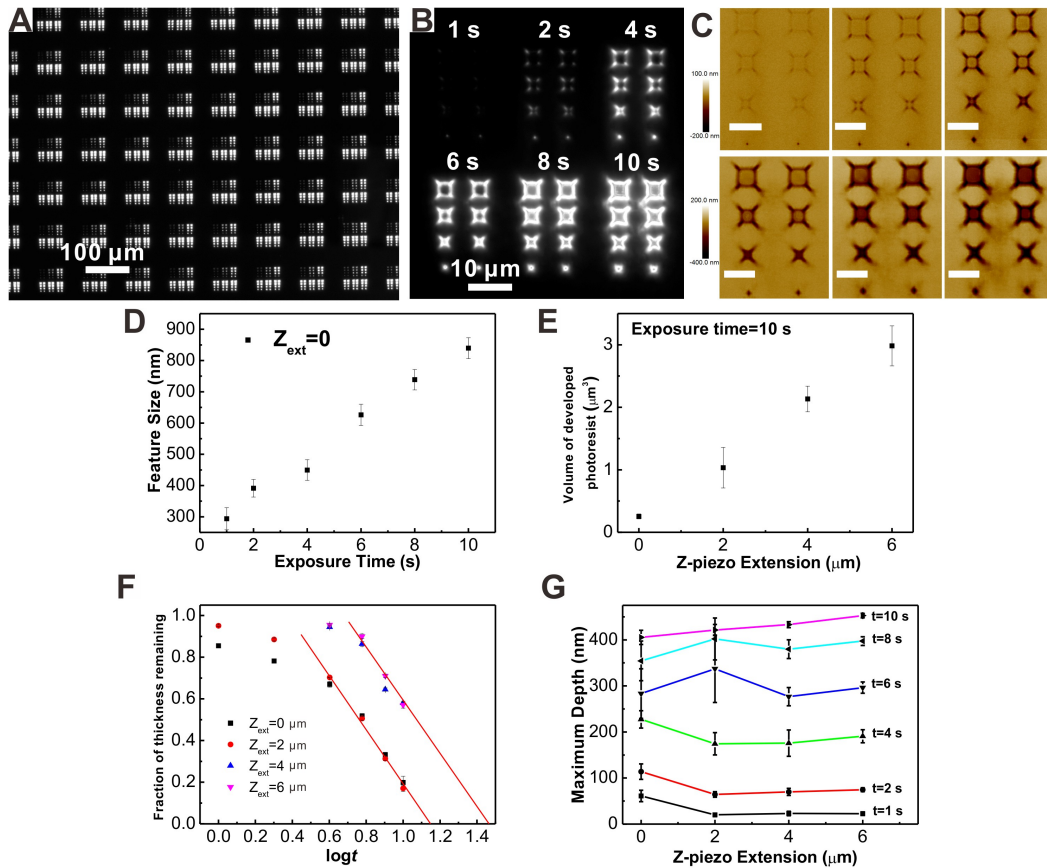


**Figure 3.3** Effect of exposure dose on the photoresist patterns generated with an apertureless cantilever-free pen array. (A&B) Dark field optical microscope images of a large region of developed photoresist patterns by varying exposure dose (A), and one typical array of dots produced with varied exposure time from 1 to 10 s and  $Z_{\text{ext}}$  of 0, 2, 4 and 6  $\mu\text{m}$  from bottom to top row. (C) Tapping-mode AFM images of the patterned dot arrays shown in (B). Scale bars: 5  $\mu\text{m}$ . (D) Plot of feature size at initial contact with exposure time. (E) Plot of volume of developed photoresist versus z-piezo extension. (F) Plot of fraction of remaining thickness in the center of patterns versus the logarithm of exposure time. (G) Statistic results of maximum depth in photoresist patterns with the exposure time and the z-piezo extension.

To further understand the optical phenomena contributing to the observed patterns, FDTD simulations were performed with a commercial package (Lumerical FDTD solutions v.8.7.0). The refractive indices of photoresist and PDMS pyramid were assumed to be 1.66 and 1.43. Due to the computation limitation, the size of pyramid base in the simulation was reduced to 8  $\mu\text{m}$ . We obtained the intensity distribution in the photoresist using tips with square cross section and edge size of 0.2, 1.2 and 3.2  $\mu\text{m}$ , respectively. Overall, a good agreement was found between the simulative (Figure 3.4) and experimental results (Figure 3.2 and 5.3) on less deformed tips. The light illuminating from the tip base is highly concentrated at the tip apex owing to the pyramidal shape, with an intensity of  $\sim 7 \times 10^4$  times higher than that in the background. Also the calculations suggest that the light at the tip is  $\sim 7$  times more intense than the incident light. Due to the interference caused by the tip surface and the bottom layer of photoresist, periodic intensity modulation is observed in all three dimensional directions. The cross-sectional profiles also point out that the penetrated light in the photoresist shows higher intensity in the dot feature than the square feature at the same depth, which is consistent with the observations on exposure time. However, the spatial distribution of light at high levels of tip deformation is neither reproduced by FDTD nor ray tracing simulations, leading us to attribute the interesting light patterns to a complex deformation of the elastomeric tips. These fascinating shapes could be studied by coupled mechanical-optical simulations and could even be used as a diagnostic to learn about tip deformation.

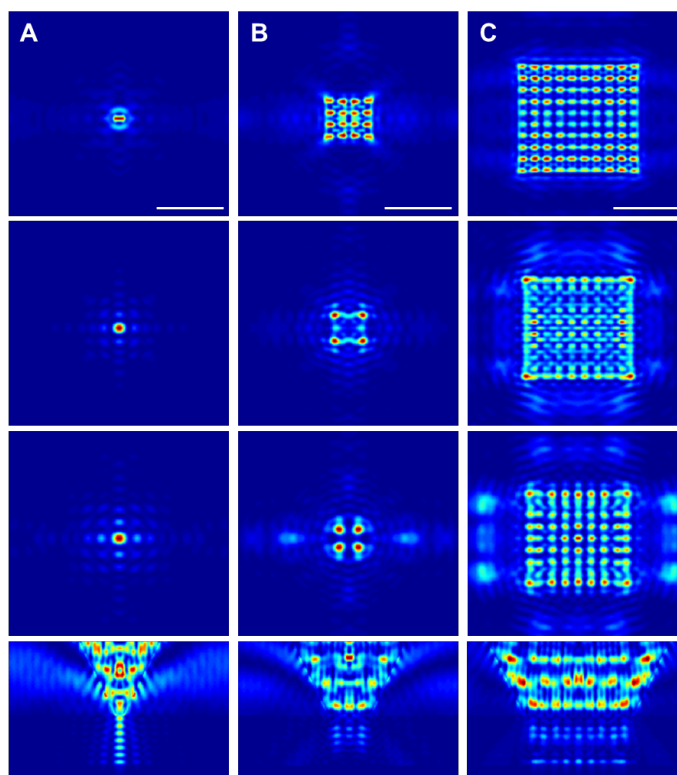


**Figure 3.4** Near-field intensity profiles generated by FDTD simulations. (A) From top to bottom: intensity profiles at horizontal planes at the top, in the middle and at the bottom of photoresist and at a vertical plane. The tip size is 0.2  $\mu\text{m}$ . (B-C) The same information as (A) for the tip sizes of 1.2 and 3.2  $\mu\text{m}$ . Scale bar: 2  $\mu\text{m}$ .

Since a standard application of photolithography is the generation of metallic features using a lift-off process, generation of Au patterns was demonstrated through the same lithographic approach using apertureless pen arrays. In evaluating this, we also took advantage of an important capability of the elastomer pen array in the context of molecule printing wherein by slightly tilting the pen array with respect to the pattern surface, one can rapidly create a gradient in feature sizes from nanometer to micrometer length scales.<sup>94</sup> Since the light propagation through the deformable tip can be force-tunable in a wide range, the tilting approach would also apply to the apertureless pen array (Figure 3.5A). As proof-of-concept, we performed a lithography experiment on a substrate coated with a polymer bilayer of 100 nm photoresist atop a 150 nm lift-off resist. Each pen was programmed to write a 8×8 dot array (pitch=7 μm) with 2 s exposure time, and the tilt was chosen such that the tip-substrate distance was varied by 6 μm across the ~0.5 cm pen array (~0.07°). After developing the resist, evaporating 2 nm Cr and 10 nm Au, and subsequently removing the polymer using a chemical etch, Au features were obtained with a size gradient ranging from ~ 3 μm to ~400 nm along the ~0.5 cm distance. From optical and SEM images of typical Au pattern arrays selected from 3 regions in one direction (Figure 3.5B), the Au patterns gradually change from square shapes to round dot, with the average size of 2.91±0.12 μm, 1.48±0.07 μm and 0.41±0.09 μm, respectively. Interestingly, by choosing thinner photoresist films and shorter exposure times, hollow square features and isolated Au features as small as 250±30 nm were generated (Figure 3.6A and B). In addition,

continuous lines were also made by writing dot patterns with pitches smaller than their feature size (Figure 3.6C). For instance, Au patterns consisting of lines with width of 400 nm, 2  $\mu\text{m}$  and 8  $\mu\text{m}$  were produced, in which the  $Z_{\text{ext}}$  was set as 0, 2, and 4  $\mu\text{m}$  to write pixels with approximate size of 400 nm, 1  $\mu\text{m}$  and 2.5  $\mu\text{m}$ , respectively. These patterning results suggest that the apertureless elastomer pens can be used for a variety of micro- and nanofabrication tasks and combinatorial screening.

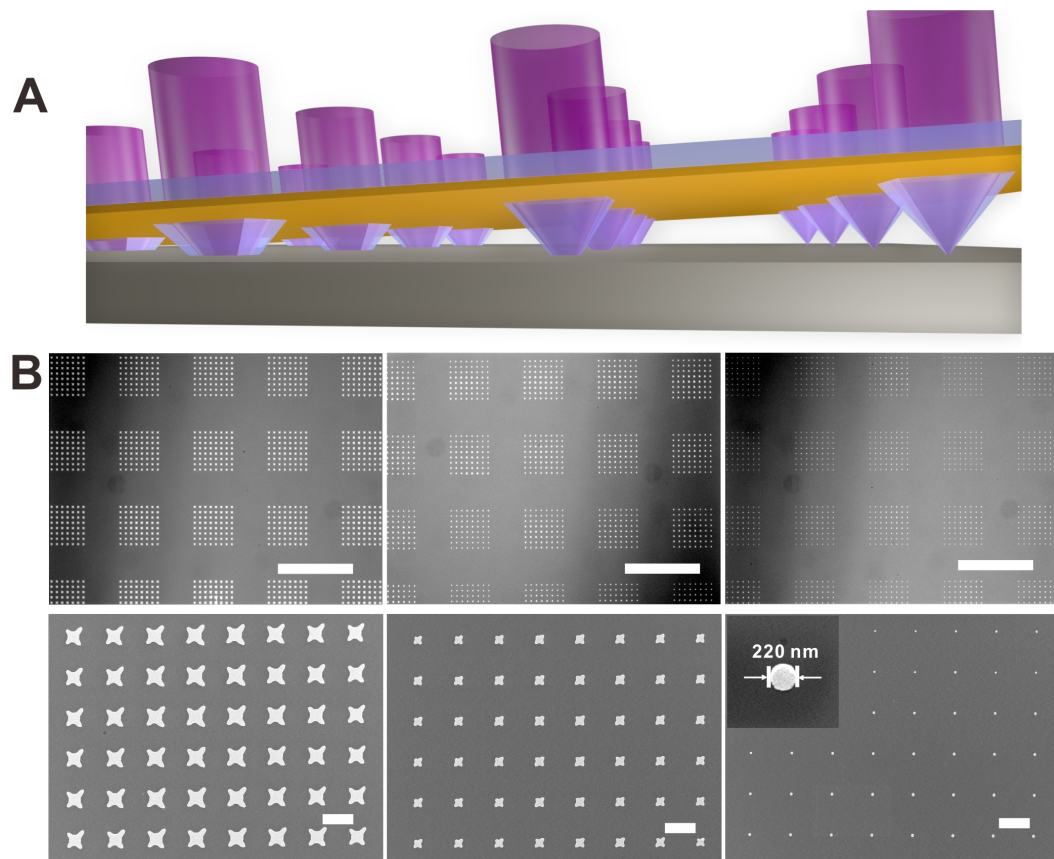


**Figure 3.5** Generation of feature gradients with force-tuned size and shape. (A) Schematic of a tilted lithography experiment using apertureless pen arrays. (B) Representative dark-field optical microscope and SEM images of Au dot arrays generated at the left, middle and right edges of a  $\sim 0.5$  cm wide pen array. Here, the average sizes were  $2.91 \pm 0.12$   $\mu\text{m}$ ,  $1.48 \pm 0.07$   $\mu\text{m}$  and  $0.41 \pm 0.09$   $\mu\text{m}$  from left to right. Scale bars are 100  $\mu\text{m}$  and 5  $\mu\text{m}$ , respectively.

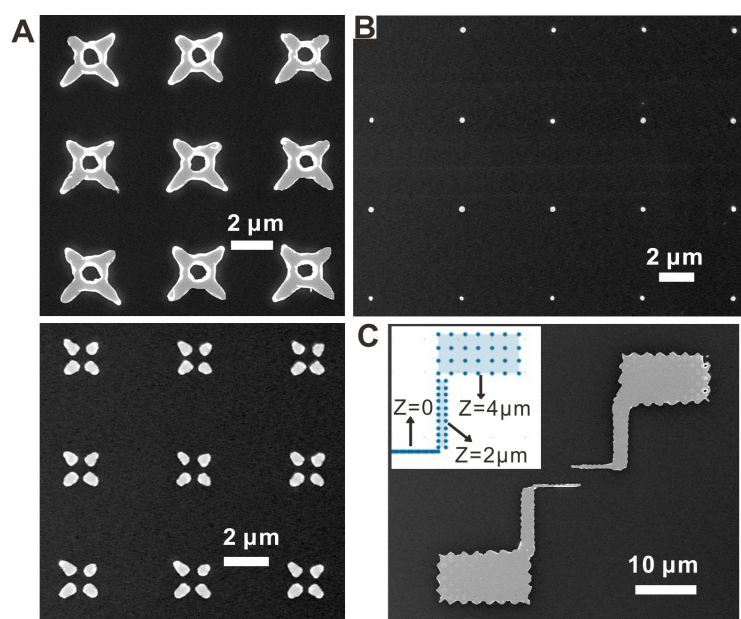


**Figure 3.6** (A-B) SEM images of Au patterns arrays fabricated with 40 nm photoresist and 150 nm lift-off resist. By adjusting  $Z_{ext}$  and exposure time, we obtained Au features with various shapes (A) and dot arrays with average size of  $250 \pm 30$  nm (B). (C) Au lines patterned by adjusting  $Z_{ext}$  to write pixels with different sizes.

Having shown that apertureless cantilever-free pen arrays can be used to effectively pattern light on a photosensitive surface, we evaluated ability to use these arrays to combine molecular printing and the delivery of optical energy. To this end, we used thiol-ene photo “click” chemistry<sup>86, 95</sup> to pattern a thiol molecule modified with fluorescent Rhodamine B dye onto an alkene-functionalized surface (Figure 3.7A). Prior to patterning, the apertureless pen array was spin-coated with a mixture of the fluorescent thiol, 2,2-dimethoxy-2-phenylacetophenone (DMPA) as photoinitiator and glycerol as high-viscosity liquid matrix. Then, the inked pen array was brought into contact with the alkene-terminated Si substrate to write a  $4 \times 3$  dot array while the pen array was illuminated by UV light (365 nm, 150-200 mW cm<sup>-2</sup>) to induce local surface photo-click reactions. In order to study the effect of illumination, the dwell time was varied between 1 and 4 min, and a column of 4 dots was also printed with the same dwell times but no illumination as a control. After patterning and subsequently sonicating the substrate in ethanol for 30 min, we characterized the samples using fluorescence microscopy (Figure 3.7B,  $\lambda_{\text{ex}} = 537$ -562 nm,  $\lambda_{\text{em}} = 570$ -640 nm) and found that the fluorescence intensity gradually increased with dwell time (Figure 3.7C and D), while the control dots showed very little fluorescence and did not change intensity with dwell time, as expected.<sup>86</sup> These results confirm that the apertureless PDMS pen can be used to simultaneously print molecules and drive a chemical reaction with light. In contrast to PPL, we did not observe spurious dots from incidental contact during leveling or a diffusion-controlled feature size owing to the efficient light confinement at the tip.

It should also be noted that while the optical intensity profile is not isotropic at high deformation, all features observed in this experiment were round, which we attribute to the feature shape being defined by molecule printing in addition to confinement of light. This raises the interesting possibility of using a combined molecule-light based approach to define uniform features that would be smaller than either technique alone.

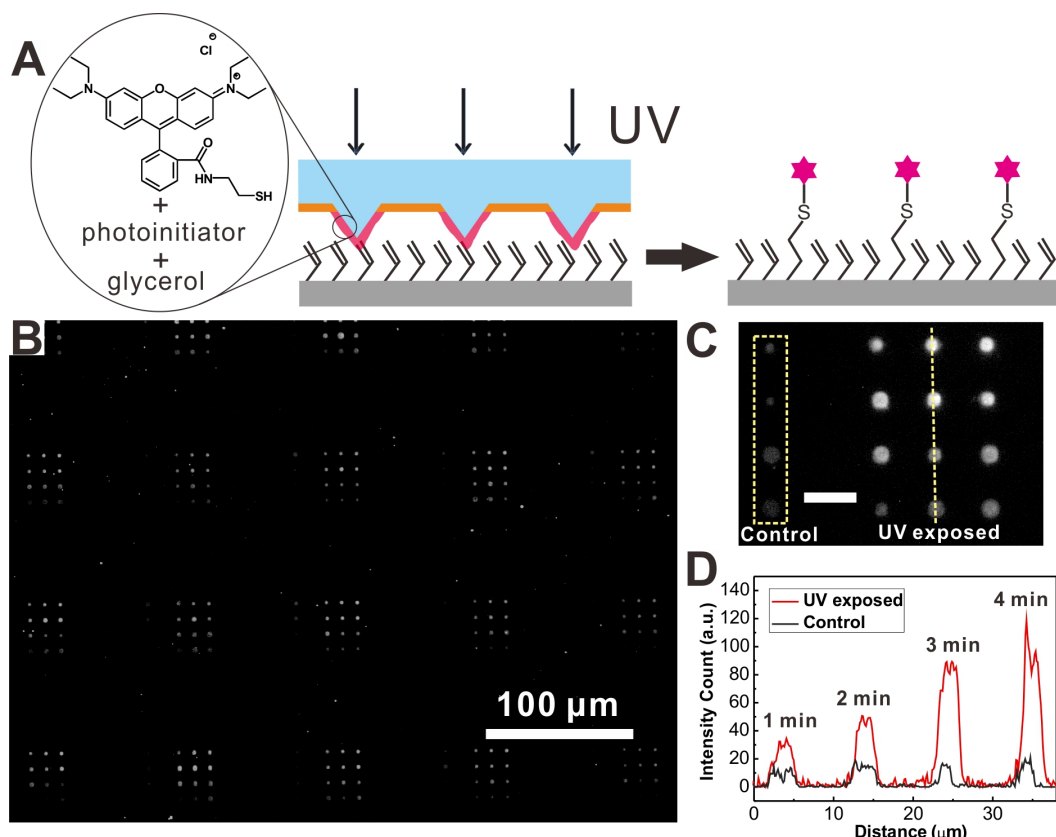


**Figure 3.7** Simultaneous delivery of optical energy and materials. (A) Schematic of photochemical printing of Rhodamine-modified thiol inks by thiol-ene photochemistry. (B) Fluorescence microscope image ( $\lambda_{\text{ex}} = 537\text{-}562 \text{ nm}$ ,  $\lambda_{\text{em}} = 570\text{-}640 \text{ nm}$ ) of the patterned  $4 \times 3$  arrays with illumination times of 1, 2, 3, and 4 min from bottom to top rows by apertureless pens. (C) Fluorescence microscope image of an array patterned by a single pen, showing dots with (right 3 columns) and without (left 1 column) UV illumination. Scale bar:  $10 \mu\text{m}$ . (D) Intensity profiles of the patterned features with different illumination times as well as the control group, indicated by the dotted lines shown in (C).

### 3.4 Conclusions

In this chapter, we have shown that due to the optical and mechanical properties of elastomeric pyramids, it is possible to locally control the chemical and optical environment of a nanoscopic region on a surface in a manner that allows for the simultaneous delivery of materials and energy. Given the simplicity of the pen arrays used here, we expect this approach to become very important for a wide range of applications that require features greater than or equal to  $\sim 200$  nm. In addition to providing insights into the optics and mechanics of nanoscale elastomeric systems, we expect this technique to significantly lower the barrier to entry to researchers interested in performing rapid prototyping and combinatorial chemistry.

## **Chapter 4**

### **On-Tip Photo-Modulated Molecular Printing**

This work was done in collaboration with Dr. Zhuang Xie

## 4.1 Introduction

The ability to print features on the 1-100 nm length scale with control over shape, size and chemical composition has enabled breakthroughs in a wide range of fields spanning from combinatorial synthesis and screening<sup>76-77, 96</sup> to fabrication of photonic and plasmonic nanostructures<sup>97-100</sup> to chip-based bioassay and diagnostics.<sup>11, 101-103</sup> Typically, two conceptually different strategies are involved in nanoscale printing:<sup>77</sup> the delivery of energy to a resist layer to induce localized physical and/or chemical conversions such as nanoimprint lithography<sup>104</sup>, and the direct transfer of “ink” molecules to a substrate from a source substance, exemplified by microcontact printing ( $\mu$ CP)<sup>2</sup> or dip-pen nanolithography (DPN)<sup>105</sup>. While the former strategy has been demonstrated suitable for fabricating nanostructures for nano-optics and nano-electronics in the past decades, the latter strategy, namely “molecular printing”, is more advantageous for chemists and biologists.

With the advent of cantilever-free scanning probe arrays, researchers can pattern large areas at very low cost without sacrificing resolution or materials flexibility. Such structures typically consist of elastomeric arrays of pyramids, mounted on hard transparent backing, that span macroscopic areas. And when utilized with a conventional atomic force microscope (AFM), they can be used to either transport molecules from their tips to surfaces<sup>35, 80, 83-84, 106-107</sup> or channel light and effect patterning with near-field or far-field resolution<sup>39, 85-86, 108</sup>. When molecules are transported from the tip to surface, one typically relies on contact time or force to control feature

size. However, by combining energy transfer (controlled with photons) with molecular transfer, one could in principle gain a new level of control. Herein, we report a new cantilever-free architecture designed to allow one to utilize light to chemically regulate the flow of molecule-based materials from tip to surface. It does so via two different pathways. The first involves a controlled light-induced polymerization that only occurs on the surfaces of the pyramids that define the tips; polymerization leads to increased ink viscosity and decreased flow rate. The second approach uses light to dynamically toggle between multiple isomeric ink forms, allowing one to change the type of molecules transported in an experiment in real time, without the need to change the array or inking procedure (Figure 4.1). Notably, the photo-modulation method is remarkably simple and straightforward to implement, and the position and intensity of the delivered light can be easily manipulated with high precision and rapid switching for site-selective control over multiple length scales.<sup>39,85</sup>

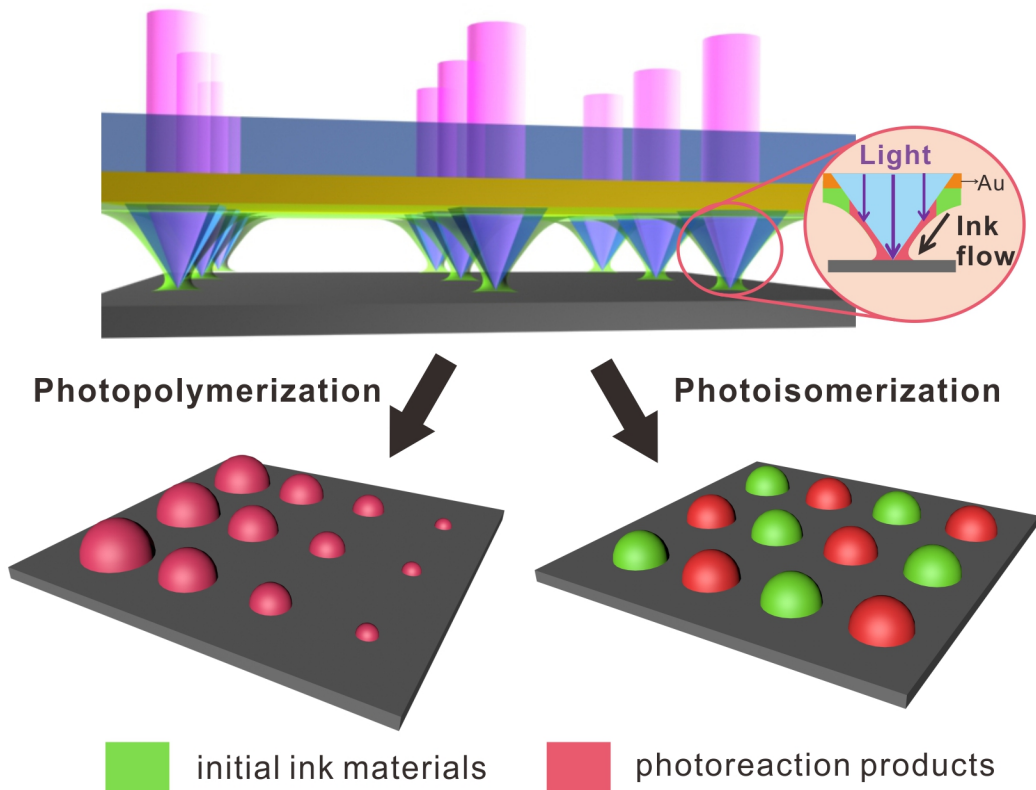


**Figure 4.1** Schematic illustration of on-tip photo-modulated molecular printing in which nanoscale photoreactions will be induced in the ink flow by simultaneous light illumination confined on the pyramidal tip. Photocontrol of ink transport and chemical composition of the printed features is demonstrated utilizing either photopolymerization or photoisomerization of ink molecules.

## 4.2 Experimental Section

**Fabrication of apertureless pen array.** Apertureless pen array was made following previously reported procedures. Briefly, hard polydimethylsiloxane (*h*-PDMS) pyramidal pen array (40  $\mu\text{m}$  edge length, 100  $\mu\text{m}$  pitch) was obtained by replica molding from a silicon master, followed by metal evaporation of 5 nm Ti / 200 nm Au on the pen array with an electron-beam evaporation system (Kurt J. Lesker Co., USA). A poly(methyl methacrylate) (PMMA950, MicroChem Inc., USA) resist layer was spin coated onto the tip array followed by baking at 100 °C for 10 min, which was repeated for one more time to ensure complete coverage. The apertureless tips were produced by etching the unprotected Au on the pen array with a Au etching solution (Gold Etchant TFA, Transense Company Inc., USA) for 70 s. By adjusting the PMMA concentration (3% to 10%) and spin coating parameters (1000 to 2000 rpm, 45 s), we were able to generate various apertureless tips with tip edge length ranging from 30 to 8  $\mu\text{m}$ .

**Photo-modulated printing by thiol-ene photopolymerization.** NOA 81 (Norland Products, Inc., USA) was diluted with propylene glycol monomethyl ether acetate with a weight ratio of 1:2. Fresh silicon wafers, hexamethyldisilazane (HMDS) modified silicon wafers and Au-coated silicon wafers were used as substrates. The apertureless pen array were briefly treated with O<sub>2</sub> plasma (150 mTorr, 65W) for 2 min, and then inked with the liquid inks by spin coating (1000 rpm, 60 s). The inked pen array was mounted onto the scanner of an atomic force microscope (XE-150, Park Systems), leveled to the substrate and programmed to write dot arrays with a

dwell time of 5 s. During patterning, a fiber-coupled LED (365 nm, 4.1 mW, Thorlabs) was placed over the back side of the pen array directly or through a focus lens, with the switch and the light intensity controlled by a LED controller. The patterns were characterized by optical microscopy (Axiovert-Zeiss) and atomic force microscopy (Dimension Icon, Bruker).

**Photo-modulated printing by free-radical photopolymerization.** Poly(ethylene oxide)-block-poly(2-vinyl pyridine) (PEO-b-P2VP,  $M_n = 2.8\text{-}b\text{-}1.5 \text{ kg}\square\text{mol}^{-1}$ , 12.5 mg $\square\text{mL}^{-1}$ ) and HAuCl<sub>4</sub> (4 mg $\square\text{mL}^{-1}$ ) aqueous solutions were stirred overnight. Then the solution was added drop wise to polyethylene glycol diacrylate (PEGDA, average  $M_n = 700$ ) containing photoinitiator 2,2-dimethoxy-2-phenylacetophenone (DMPA, 50 mg $\square\text{mL}^{-1}$ ) in a volume ratio of 1:1. Finally, a small amount of glucose (25 mg/mL) was added to the ink to accelerate the photopolymerization. The ink was spin-coated onto the pen array with a speed of 3000 rpm for 60 s. The printing procedure was similar to that of NOA ink, with a mounted high-power LED (365 nm, 190 mW, Thorlabs) employed as the light source and HMDS-modified silicon wafer as the substrate. After patterning, the substrate was annealed at 120 °C for 24 h under argon and characterized with scanning electron microscopy (S-4800-II, Hitachi).

**Photo-modulated printing by photoisomerization.** A spiropyran derivative 1 $\square$ ,3 $\square$ -dihydro-1 $\square$ ,3 $\square$ ,3 $\square$ -trimethyl-6-nitrospiro[2H-1-benzopyran-2,2 $\square$ -(2H)-indole] (SP, 1 mg $\square\text{mL}^{-1}$ ) was mixed with poly (ethylene glycol) (PEG,  $M_w = 600$ ) in toluene (10 mg $\square\text{mL}^{-1}$ ). The apertureless

pen array was inked with PEG/SP ink by spin coating (1000 rpm, 60 s) and the printing was performed on the HMDS-modified silicon substrate with a dwell time of 10 s. The used lights were fiber-coupled LEDs with UV (365 nm, 4.1 mW) and green (530 nm, 5 mW) wavelengths. The patterns were characterized by dark-field optical microscopy (Axiovert-Zeiss) and fluorescence microscopy ( $\lambda_{\text{ex}} = 537\text{--}562 \text{ nm}$ ,  $\lambda_{\text{em}} = 570\text{--}640 \text{ nm}$ ).

### 4.3 Results and Discussion

In order to perform photochemical reactions within the on-tip ink flow, apertureless pen array with opaque backplane and transparent PDMS pyramidal tips, namely apertureless tips, were employed to confine the light illumination on the ink-coated tips.<sup>108</sup> As proof-of-concept demonstration of photo-modulation by photopolymerization, a commercially available UV-curable liquid photopolymer (NOA 81, Norland Products, Inc.) was chosen as ink material owing to its appropriate initial viscosity (0.3 Pa·s) for inking and fast curing (2 J/cm<sup>2</sup> for full curing) in air atmosphere. When exposed to UV light, thiol-ene photopolymerization<sup>109</sup> will occur in the NOA ink between the urethane-based tetrafunctional allyl ether and its thiol counterpart trimethylolpropane tris(2-mercaptopropanoate).<sup>110</sup> The photopolymerization will result in an increase in ink viscosity up to two orders of magnitude in the bulk liquid ink as reported in literatures.<sup>111</sup> Since the NOA ink is solvent-free and impermeable to water vapor, we hypothesized that the ink

rheological properties during printing is determined by the photopolymerization in the ink flow, which will greatly govern the ink transport.<sup>112-114</sup> To test the on-tip photo-modulation of ink properties by polymerization, in a typical experiment, the apertureless pen array (40 μm side length, 100 μm pitch) was inked with the NOA ink by spin coating, and then attached to a piezoelectric scanner. After leveling the 2D pen array with respect to a silicon wafer substrate, the pen array was brought into contact with the substrate controlled by a scanning probe system (XE-150, Park Systems) to pattern a 8×5 dot array by each pen with dwell time of 5 s, during which simultaneous UV illumination from a 365 nm fiber LED was applied onto the pen array (~8×5 mm<sup>2</sup>, ~4,000 pens) from the back side. The selective illumination was conducted with the illumination area confined as ~3 mm in diameter through a focus lens (intensity ~0.1 mW/cm<sup>2</sup>), while the rest of the pen array (~33 mm<sup>2</sup>) was maintained in dark as control to compare the effect of UV light and dark conditions. After patterning, a distinct difference between the features printed with and without UV illumination was observed by optical microscopy. As seen from Figure 4.2A, in the area under continuous UV illumination, the printed NOA features exhibited gradual decrease in feature size along with the writing direction, while the feature size was retained in the arrays printed under dark. Further atomic force microscopy (AFM) characterization confirmed that immediately after turning on the UV light, both the diameter and height of the printed features were gradually reduced, which led to a drastic shrinkage in the feature volume by greater than a factor of 1,000 after 18-min UV illumination compared with the

volume of the initially printed features as well as the features printed under dark (Figure 4.2B and 6.2C). We then examined how the ink transport rate varied along with the photopolymerization process by investigating the time-dependent ink deposition under UV illumination. We patterned NOA dot arrays at different UV illumination stages from 0 s to 540 s sequentially. And in each stage, the dwell time was varied from 1 s to 16 s (Figure 4.3). By plotting the feature volume with the dwell time under different UV illumination stages (Figure 4.2D), it is clearly shown that the ink transport rate is decreased with increasing UV illumination time. Indeed, the light-tuned ink transport can be attributed to the increased ink viscosity by photopolymerization to slow down the ink flow on the tip.<sup>113</sup> On the other hand, we could obtain a series of sub-micrometer polymer features with various polymerization degrees through the on-tip flow polymerization process. Therefore, the on-tip photo-modulation allows us to control and monitor the photopolymerization within the ink flow, which could provide an alternative way to study on polymerization and the associated polymer properties at the sub-micrometer scale by molecular printing.

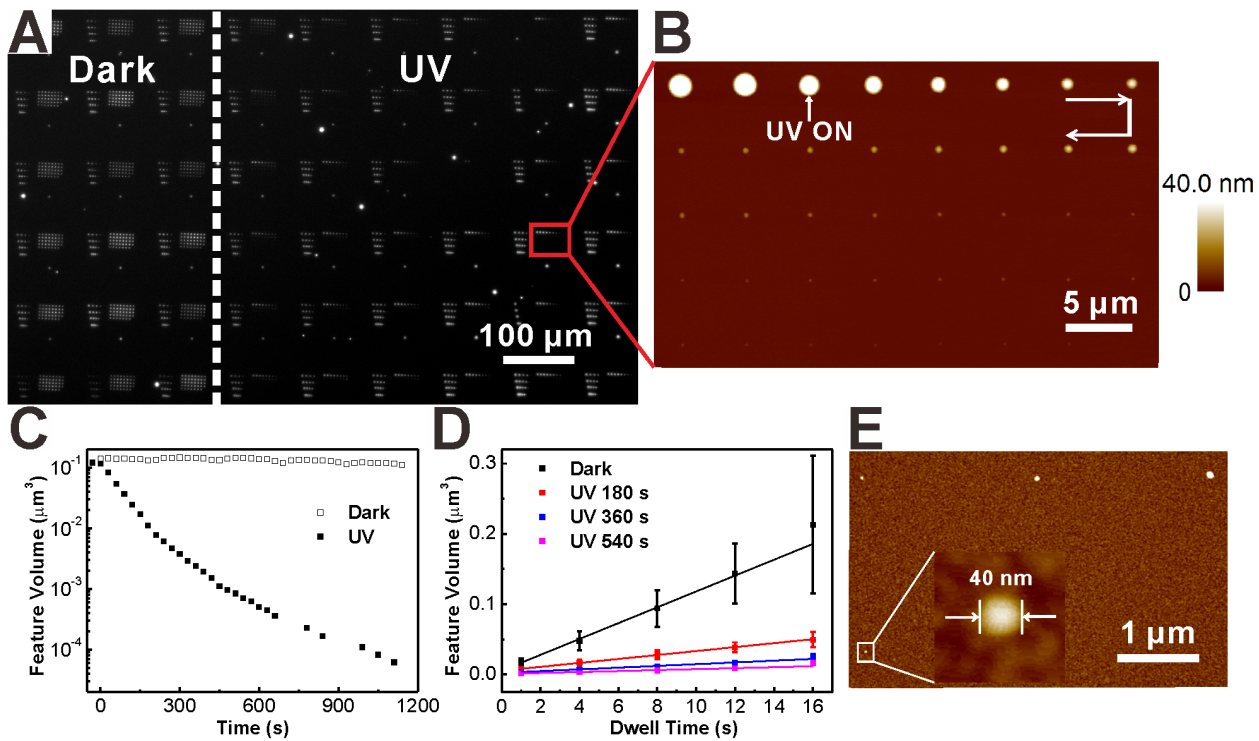


**Figure 4.2** Photo-modulated ink transport. (A) Dark-field optical microscope image of the printed features of NOA photopolymer ink under dark (left) and simultaneous UV illumination (right) conditions. (B) Magnified atomic force microscopy (AFM) image of one typical NOA dot array patterned with UV light, with the white arrows showing the writing direction. The dwell time for each dot is 5 s. (C) Plot of feature volume with time for two typical arrays patterned under dark and UV light. The UV intensity is  $\sim 0.1 \text{ mW/cm}^2$ . (D) Dwell-time dependence of the NOA feature volume with varied UV illumination time, with statistics from arrays patterned by 5 pens. (E) AFM image of NOA dot features generated on Au substrate with size ranging from 100 to 40 nm by 18-min UV illumination. The UV intensity is  $\sim 0.1 \text{ mW/cm}^2$ .

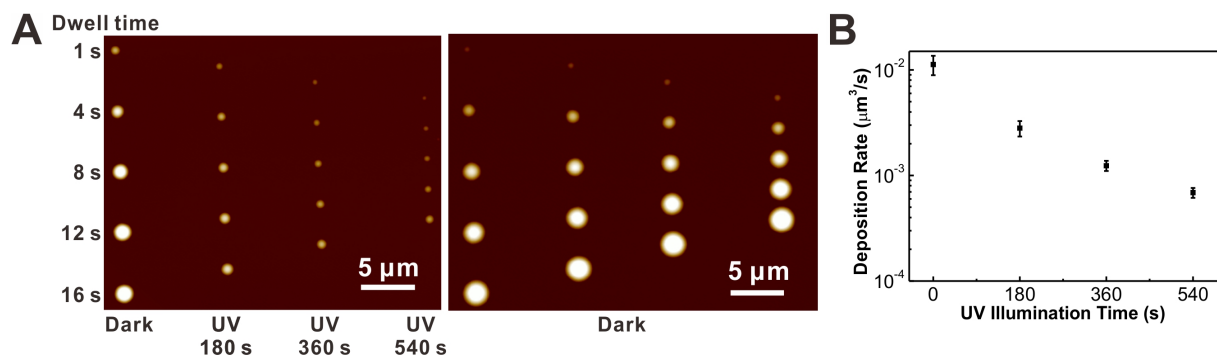
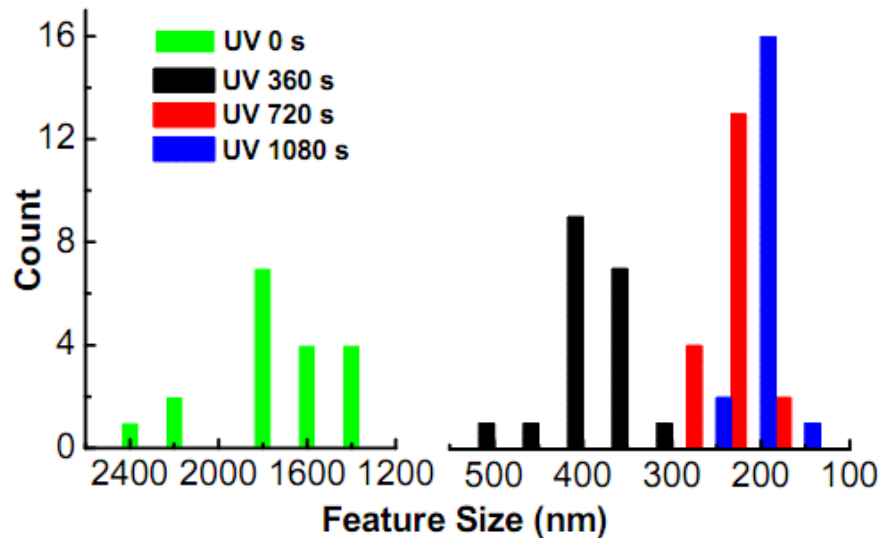


**Figure 4.3** (A) AFM images of a typical dot array for time-dependent ink transport study in which each column was patterned with different UV illumination time sequentially, and a control array patterned under dark. (B) Plot of deposition rate with UV illumination time corresponding to Figure 2D. Statistics are obtained from arrays printed by 5 pens.

From a surface patterning point of view, since the local mobility of ink molecules on the tip can be adjusted by polymerization, the photochemical approach renders the capability for fine controlling the feature size regardless of the initial ink viscosity, environmental humidity, and ink loading. As shown in Figure 4.2E, we have achieved NOA features with size ranging from 100 to 40 nm on Au substrate with continuous UV illumination prior to the complete solidification of ink on the tip. Moreover, the on-tip photopolymerization strategy also led to improved size uniformity of NOA features among different pens (Figure 4.4). Besides the NOA ink based on thiol-ene photoreaction, the photoinitiated polymerization can be universally applied to a wide range of ink materials to control the ink transport. As proof-of-concept experiment, a diacrylate monomer polyethylene glycol diacrylate (PEGDA, average  $M_n = 700$ ) was employed as the flow phase incorporating poly(ethylene oxide)-block-poly(2-vinyl pyridine) (PEO-b-P2VP) loaded with HAuCl<sub>4</sub>, in which the free-radical photopolymerization of PEGDA will dominate the transport of PEO-b-P2VP/HAuCl<sub>4</sub> precursors. After reduction of metal ions within the patterned polymers, metal nanoparticles will be obtained with the position and size dictated by the polymer features.<sup>113, 115-117</sup> The mixture was printed on hexamethyldisilazane (HMDS) modified silicon substrate with continuous UV illumination (365 nm, ~150 mW/cm<sup>2</sup>) and 5 s dwell time. Again, the feature size was observed to reduce from 1265 to 325 nm during the 15-min illumination (Figure 4.5A). To show that the patterned polymer spots can serve as nanoreactors for nanoparticle synthesis, the patterned substrate was annealed at 120 °C for 24 h

under argon. As a consequence, single Au nanoparticle was found within each polymer spot, and the particle size was determined by the polymer feature size (Figure 4.5B and 6.5C) in accordance with literatures.<sup>113, 115-117</sup> As typical examples, Figure 4.5B shows nanoparticles with size of 19, 15, and 8 nm obtained in the corresponding polymer features with size of 1100, 760, and 325 nm, respectively. More importantly, since the light can be applied in a site-selective manner using the focus lens or other tools,<sup>39, 85</sup> it is possible to create arrays of nanoparticles with size gradient in controlled positions.



UV Time (s)	0	360	720	1080
Average Size (nm)	1790±310	407±34	233±26	174±19
RSD	17%	8%	11%	11%

**Figure 4.4** Size uniformity statistics of NOA dot features over a  $3 \times 3 \text{ mm}^2$  area from randomly selected 11 arrays.

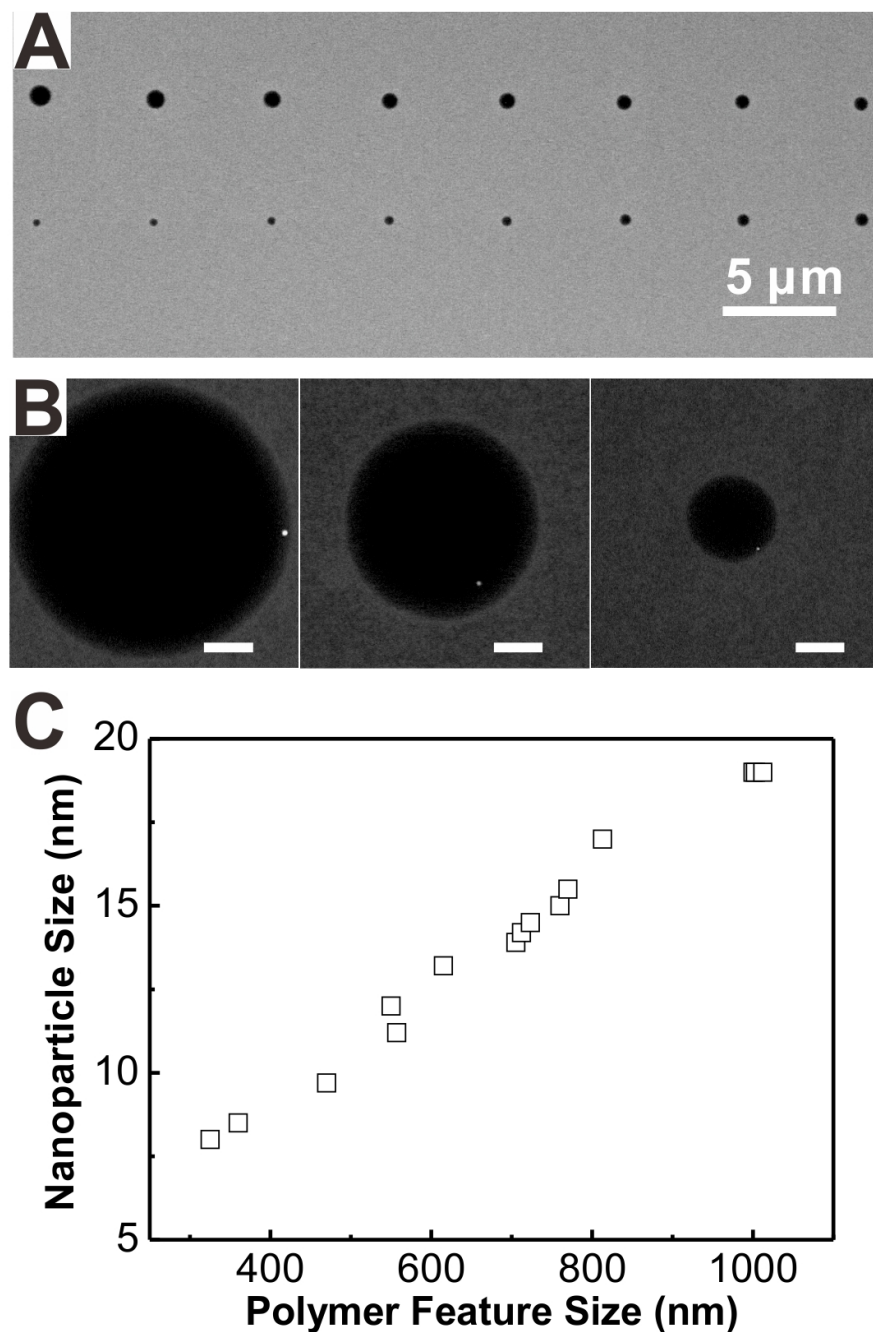


**Figure 4.5** (A) Scanning electron microscope (SEM) image of a dot array of PEGDA/PEO-b-P2VP/HAuCl<sub>4</sub> ink printed under UV illumination and after annealing. The UV intensity is  $\sim 150 \text{ mW/cm}^2$ . (B) Magnified SEM image of the patterned polymer spots with single Au nanoparticles inside. From left to right, the polymer feature size was 1100, 760, and 325 nm, corresponding to nanoparticles with size of 19, 15, and 8 nm, respectively. Scale bars: 200 nm. (C) Plot of Au nanoparticle size with printed polymer feature size controlled by light.

As a platform for on-tip photoreactions, one unique feature enabled by apertureless pen array is the continuous refilling of ink flow, through which the ink properties on the tip can be reversibly modulated depending on the presence or absence of UV light. This was observed in an experiment of printing an  $8 \times 8$  dot array of NOA ink by the apertureless pen array, during which UV light (365 nm LED,  $\sim 0.1$  mW/cm<sup>2</sup>) was applied at the beginning to reduce the feature volume for the first 3 rows. Interestingly, after the light was turned off at the start point of the 4<sup>th</sup> row (Figure 4.6A), the volume of the subsequently printed features was found to gradually increase and finally reach to a stable value comparable to that of the initial features. Notably, such reversible characteristic in ink transport was not available with polymer pen array<sup>80</sup> and beam pen array<sup>39, 85</sup> (Figure 4.6A and 6.6B), which led us to attribute the interesting size recovery phenomenon to the apertureless pen architecture.

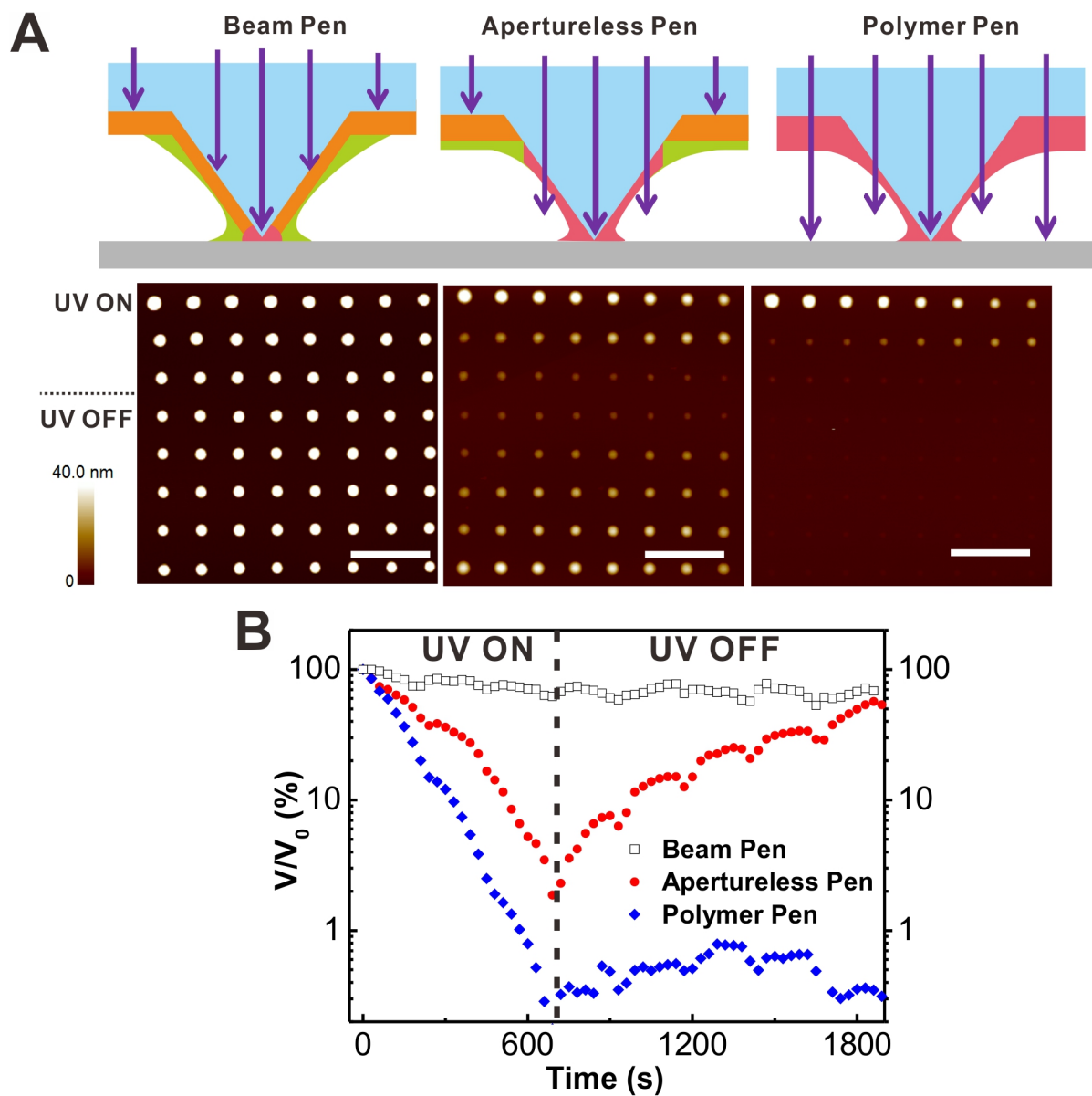


**Figure 4.6** Reversible modulation of ink properties by light switching. (A) Schematic illustrations of light propagation on different pen arrays and the resulted AFM images of dot arrays patterned with switched light. Scale bars: 10  $\mu\text{m}$ . (B) Plot of feature volume ratio  $V/V_0$  with time during the patterning with switched light by three types of pyramidal pen arrays. The UV intensity is  $\sim 0.1 \text{ mW/cm}^2$ .

Because of the presence of opaque metal layer covering the flat area between pens and the base of pyramid pens on the apertureless pen array (Figure 4.7A), the photoreaction of ink molecules is confined mainly on the apertureless tips exposed to light. More importantly, by spin coating of liquid ink on the pyramidal pen array, the ink congregates surrounding the base of pyramidal pens where the light is blocked (Figure 4.7B). After back-side illumination on the apertureless pen array, the ink on the apertureless tips can be photo-cured, while the ink covering the metal-coated areas maintains unreacted and can be washed away by acetone (Figure 4.7C). Thus, during printing, the ink protected against light functions as an ink reservoir to refill “fresh” low-viscosity monomer ink towards the tip apex driven by the gradient in Laplace pressure along the pyramidal pen.<sup>114</sup> Once the UV light is switched off, the diffusion between the ink reservoir and the on-tip photopolymerized ink will decrease the local ink viscosity at the tip apex (Figure 4.7D), giving rise to the increase in the ink transport rate and the recovery of feature volume.

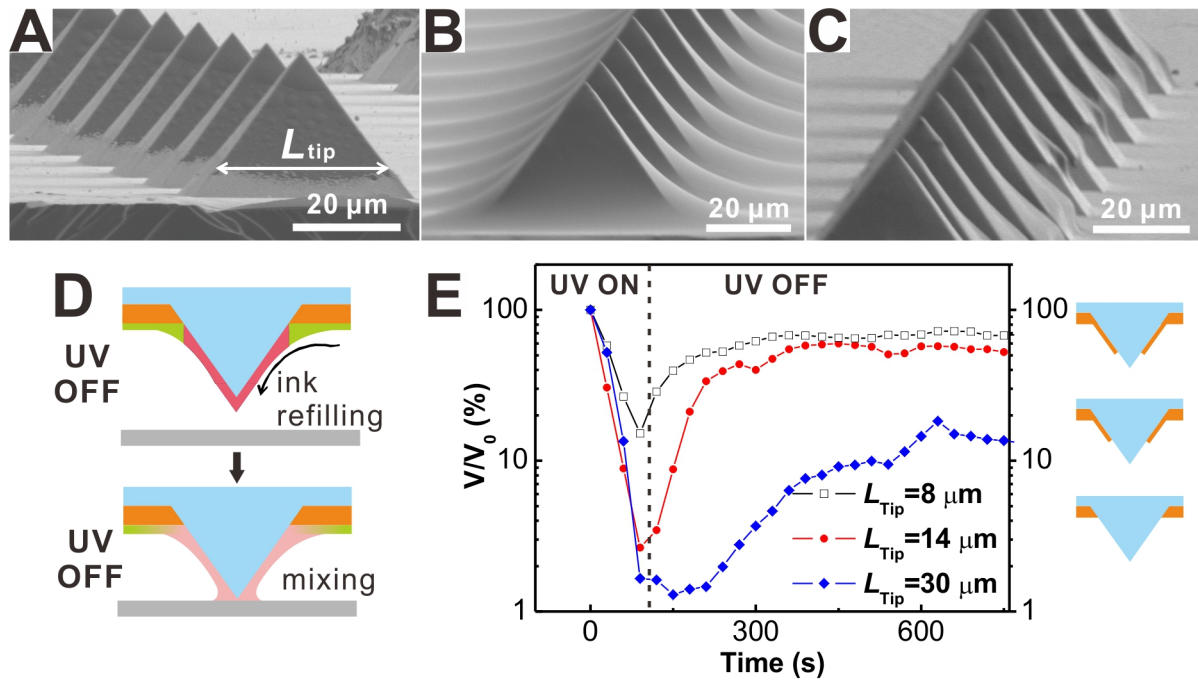


**Figure 4.7** (A) SEM image of the apertureless pen array, where  $L_{tip}$  represents the edge length of the apertureless tip. (B) SEM image of the ink-coated pen array after spin coating, showing the ink accumulation around the base of pens. The image is obtained by curing the NOA ink on the pen array from front side. (C) SEM image of the ink-coated pen array after back-side UV illumination for 40 min and acetone rinsing. (D) Schematic illustration of the ink refilling and mixing mechanism for recovery of the ink properties. (E) The effect of  $L_{tip}$  on the feature volume ratio change during the patterning with switched light. The UV intensity is  $\sim 2 \text{ mW/cm}^2$ .

Knowing that the ink properties are determined by the equilibrium result of on-tip photoreaction and dynamic ink refilling, we further showed that the size decay and recovery could be tuned by controlling the two opposite effects. For example, we employed different pen arrays with varied edge length of apertureless tip ( $L_{\text{tip}}$ , Figure 4.7A) of 30, 14 and 8  $\mu\text{m}$  to adjust the on-tip ink refilling. As shown in Figure 4.7E, under the same experiment conditions, the smaller  $L_{\text{tip}}$  resulted in slower size decay rate but faster size recovery due to the shorter path for refilling of monomer ink. In addition, we found that both the decay and recovery ratio of feature volume were found to decrease with the degree of photopolymerization (Figure 4.8). Therefore, the ink properties such as viscosity and composition could be potentially modulated in a wide range and with rapid switching by manipulating the reaction process (e.g., varying the time and light intensity) and the material transport rate in the ink flow

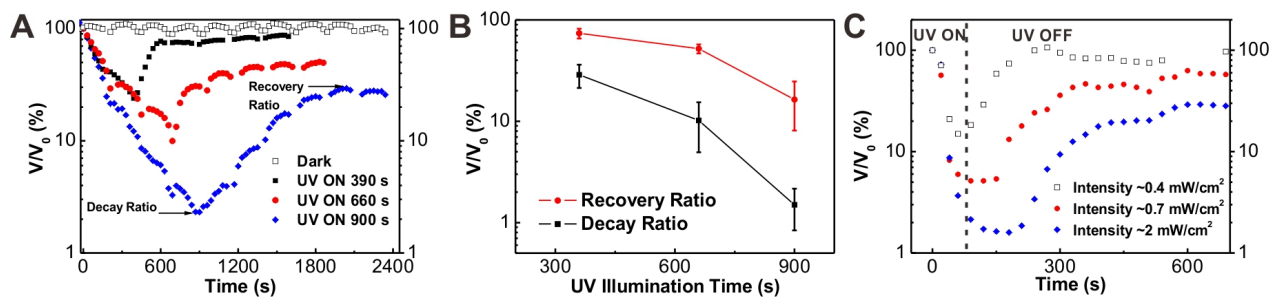


**Figure 4.8** Effect of photopolymerization on size decay and recovery. (A) Plot of feature volume ratio with time, in which the UV illumination time was varied from 390 s to 900 s. The UV intensity is  $\sim 0.1 \text{ mW/cm}^2$ . (B) Plot of decay ratio and recovery ratio with the UV illumination time, with statistics from 5 pens. (C) Plot of feature volume ratio with time by varying the applied UV intensity. The edge length of the used apertureless tip is 30  $\mu\text{m}$  for all the figures.

Having shown that the ink transport and composition can be reversibly tuned by the on-tip photoreaction and ink hydrodynamic behavior, we evaluated the ability of the on-tip flow photochemistry to yield features with varied chemical functionality. In evaluating this, we also took advantage of reversible photochemistry for dynamic photocontrol of pattern composition. To this end, we used photochromic molecules that afford photo-reversible reconfiguration with easily detected color and fluorescence change for proof-of-concept experiments. The employed ink molecule is a spiropyran derivative 1',3'-dihydro-1',3',3'-trimethyl-6-nitrospiro[2H-1-benzopyran-2,2'-(2H)-indole] (SP) that can switch its chemical structure by UV or visible light through photoisomerization to realize various dynamic functions.<sup>118</sup> Under UV illumination, this molecule can be converted from closed-ring SP structure to open-ring merocyanine (MC) structure that presents strong fluorescence emission ( $\lambda_{\text{max}} \approx 650$  nm) due to the delocalized electrons through the whole molecule (Figure 4.9A).<sup>118</sup> Also the molecular structure can be completely reversed by exposing to visible light. We mixed the photoreactive SP molecules with polyethylene glycol (PEG,  $M_w=600$ ) as delivering matrix,<sup>21, 119</sup> and spin coated the ink mixture onto the apertureless pen array for printing, during which the light was controlled to switch between UV (365 nm,  $\sim 2$  mW/cm<sup>2</sup>) and visible (530 nm,  $\sim 2.5$  mW/cm<sup>2</sup>) wavelengths. To show the two molecular states, SP and MC, can be reversibly produced in the ink flow by light, a 4×4 dot array was first printed under UV illumination with dwell time of 10 s, followed by printing an interlaced 3×3 dot array under visible light within the first 4×4 dot array. The two dot arrays

were seen from the dark-field optical microscope, while in the fluorescence images ( $\lambda_{\text{ex}} = 537 - 562 \text{ nm}$ ,  $\lambda_{\text{em}} = 570 - 640 \text{ nm}$ ), only the  $4 \times 4$  arrays printed under UV were clearly observed. This indicates the conversion of MC structure by UV light and the regeneration of SP structure under visible light during ink transport. The molecular switch between SP and MC states allows us to reversibly and rapidly change the pattern functionality for multiple cycles, as demonstrated in Figure 4.9C and 6.9D. Corresponding to the cycling of UV and visible light in each row, an alternation of weak and strong fluorescence was observed in features printed by one pen. Evidently, the chemical composition is alternately changed for the ink deposited in each row, and the switch between the two molecular states can be accomplished within 1 min. It should be noted that the previously printed features will not be affected in the subsequent printing due to the confined light propagation on apertureless tips, which is vital for the reversible generation of chemical compositional gradient. In addition, this is the first time demonstration of patterned surface with different chemical functionality by material delivery from a single pen. These results suggest the on-tip photo-modulated molecular printing could be used for maskless and reversible production of patterned surface chemistry and compositional gradient.

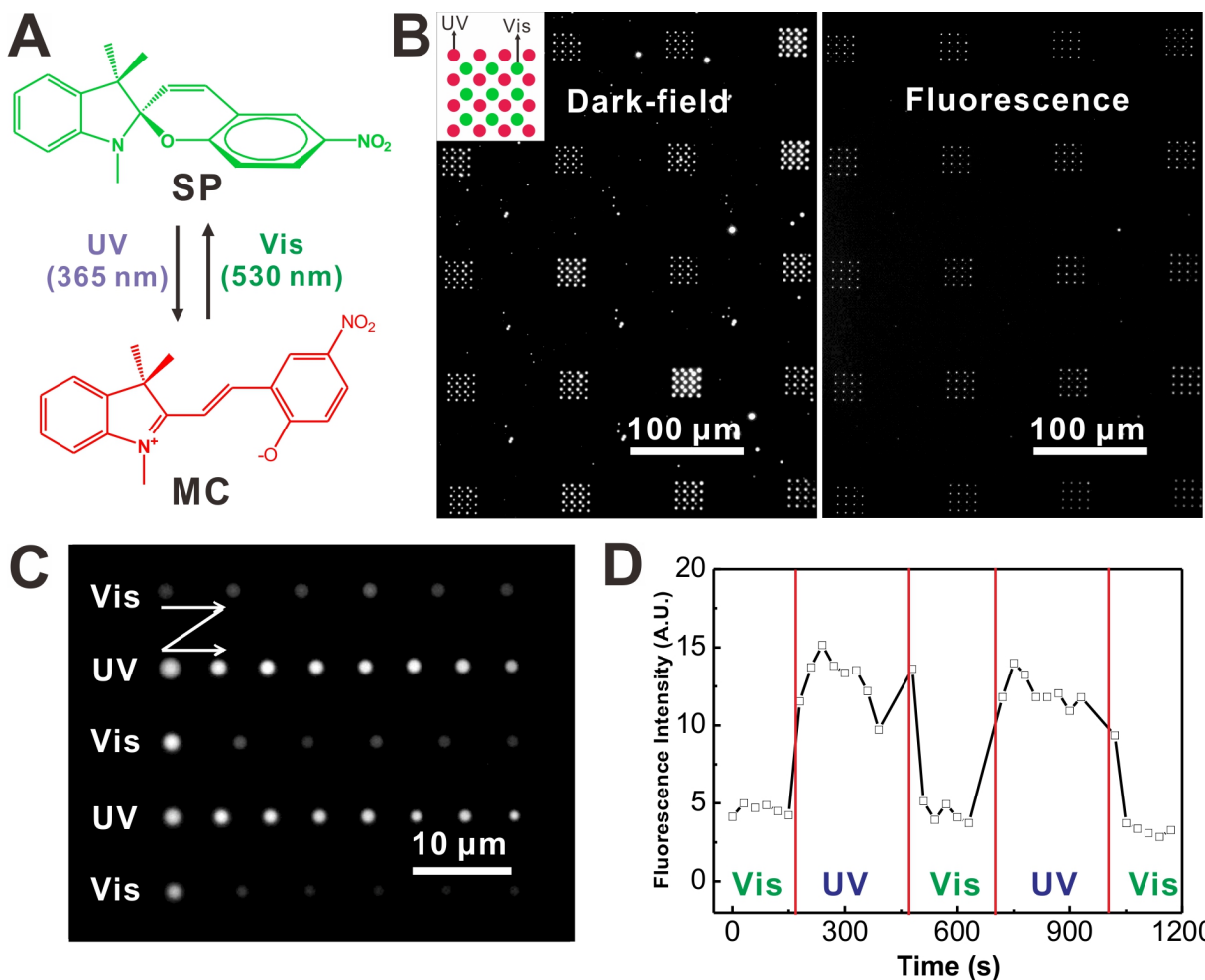


**Figure 4.9** Photo-reversible modulation of pattern functionality. (A) Schematic illustration of photoisomerization between spiropyran (SP) and merocyanine (MC) structures. The MC structure shows intense red fluorescence. (B) Dark-field and corresponding fluorescence ( $\lambda_{\text{ex}} = 537 - 562 \text{ nm}$ ,  $\lambda_{\text{em}} = 570 - 640 \text{ nm}$ ) microscope images of two interlaced arrays of PEG/SP ink printed with UV and visible light illumination, respectively. The UV intensity is  $\sim 2 \text{ mW/cm}^2$  and the power for green light is  $\sim 2.5 \text{ mW/cm}^2$ . (C) Fluorescence microscope image of the printed dot arrays under alternately varied visible and UV light in each row, with the white arrow showing the writing direction. (D) Plot of fluorescence intensity with the alternation of light.

#### 4.4 Conclusions

Chemical regulation of nanoscale ink flow by light on cantilever-free pyramidal pen array has been explored to achieve on-tip photo-modulated molecular printing. With the continuous ink flow and simultaneously integrated light energy on the apertureless pen array, it is possible to dynamically modulate the transport and chemical composition of ink molecules on the tip *in situ*, leading to reversible control over the feature size and composition. Given the widespread use of photochemistry and flow reaction<sup>120</sup>, we anticipate the on-tip photo-modulated molecular printing to provide a lab-on-tip platform for fundamental studies on nanoscale photoreactions, molecular diffusion, fluidic phenomena and surface science, as well as for the development of new strategies for rapid prototyping of multiplexed functional patterns and combinatorial chemistry.

## **Chapter 5**

### **Capillary Force-driven, Large-area Alignment of Multi-segmented Nanowires**

Portions of this chapter have been published in: *ACS Nano, 2014*

This work was done in collaboration with Dr. Xiaozhu Zhou

### 5.1. Introduction

There has been an increasing interest in the synthesis and application of anisotropic nanostructures due to their rich plasmonic, optoelectronic, and catalytic properties.<sup>121-124</sup> Among them, on-wire lithography (OWL)-generated gapped nanowires<sup>125-129</sup> have received widespread interest and show promise in various fields, including plasmonics, surface-enhanced Raman spectroscopy (SERS), nanoencoding, and molecular electronics.<sup>130-133</sup> Because of the fine control OWL provides over metal segment length and gap size, the technique has been used for the systematic investigation of the structure-function relationships for segmented wires of a wide variety of compositions and lengths, opening avenues to new nanowire applications.<sup>131</sup> For example, the localized surface plasmon resonance wavelength can be tailored deliberately by simply changing the gap size in 35 nm diameter dimer structures consisting of two 70 nm long gold segments.<sup>127</sup> Such OWL nanostructures have been used to understand the origins of hotspots in SERS and create novel taggants, known as SERS nanosheets.<sup>134</sup> In addition, we have recently demonstrated that these OWL-generated nanowires can be used as etch masks to make gapped graphene nanoribbons (GNRs).<sup>135</sup> However, in order to realize the full potential of OWL-generated nanostructures, it is imperative that methods for assembling them over large areas with control over position, orientation, and density be developed. Arrays of OWL nanostructures are of particular interest for SERS applications since, in principle, more uniform Raman signals can be obtained from ordered arrays of gapped nanowires as opposed to randomly oriented and

spaced structures. Furthermore, it may be possible to use aligned OWL nanostructures as etch masks, providing methods for translating large patterns consisting of gapped nanowires into underlying substrates. This capability would be potentially useful for a broad range of applications, spanning electronics,<sup>136-137</sup> plasmonics<sup>138</sup> and metamaterials.<sup>139</sup> Thus far, a few methods have been developed for preparing large arrays of multi-segmented nanowires. For example, Xu et al. have utilized pre-patterned arrays of nanomagnets to align nanowires that contain magnetic Ni segments.<sup>140</sup> Although a significant step forward, the disadvantages of this method are the low-yield and poor control over wire number and orientation. In addition, the requirement of pre-fabricating arrays of nanomagnets makes this method less straightforward. Our group has developed a brush method to mechanically align multi-segmented nanowires.<sup>141</sup> However, this method is only effective for micrometer long nanowires due to the large size of the brush hair (micrometer scale) and is not suitable for aligning single wires. Recently, methods that utilize capillary forces to assemble chemically-synthesized spherical and rod-like gold particles in pre-defined trenches<sup>142-144</sup> have shown promise for assembling individual and collections of particles on pre-patterned substrates. However, with these methods, challenges exist in achieving precise control over interparticle distance for multiple particles within one trench, which is a necessity for a variety of applications such as local field enhancement in SERS-active structures. Since OWL allows one to prepare nanostructures separated by multiple well-defined nanoscale gaps, a method to assemble such structures with capillary forces could

provide a straightforward way of aligning dimers or multimers with precise control over interparticle distance.

Herein, we report the large-area assembly of electrochemically-synthesized multi-segmented nanowires of different gap sizes, lengths and aspect ratios with control over wire position and orientation (Figure 5.1). To show prototypical electronic and optical devices based on these structures, we evaluated their use as masks for the fabrication of arrays of gapped graphene nanoribbons and as SERS substrates for the detection of small molecules.

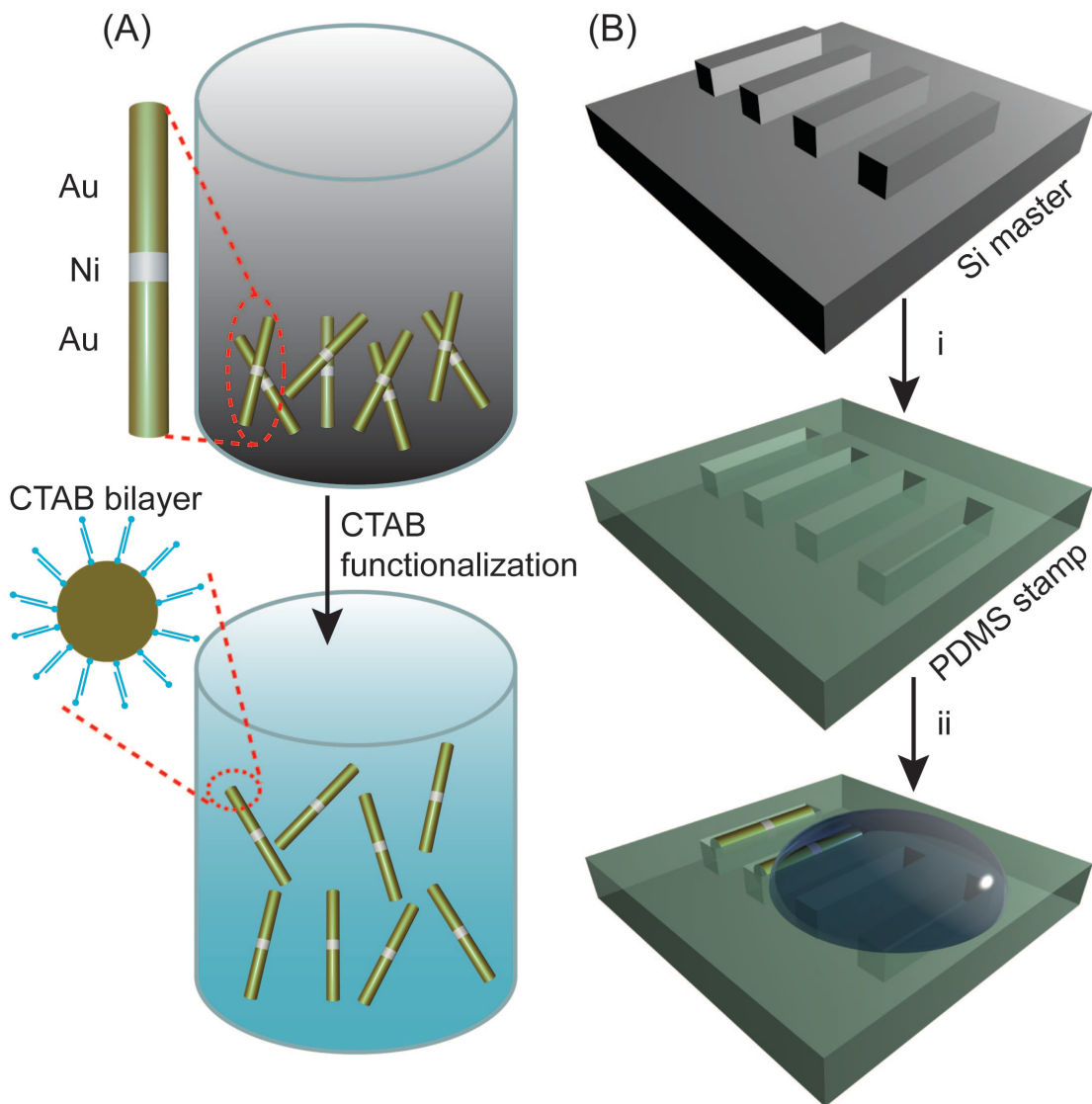


**Figure 5.1** Schematic illustration of the alignment of multi-segmented nanowires into trenches by capillary forces. (A) Functionalization of nanowires with CTAB in a 0.45 mM CTAB aqueous solution. Coating of a bilayer CTAB on the surface of the nanowires prevents their aggregation and increases the stability of the suspension. (B) (i) Fabrication of PDMS stamp with negative trenches by curing elastomers on a silicon master with positive features. (ii) Alignment of nanowires into the trenches when a drop of nanowire solution moves across the trench area driven by a drying process (via heating).

## 5.2. Experimental Section

**Synthesis of multi-segmented metal nanowires and functionalization with hexadecyltrimethylammonium bromide (CTAB).** Multi-segmented nanowires consisting of Au-Ni-Au were electrochemically synthesized in anodized aluminum oxide (AAO) membranes from Synkera Technologies, Inc. having a manufacturer-specified pore diameter of 35 nm. The general electrochemical deposition process has been described in the literature.<sup>126-127</sup> Specifically, nanowires with different lengths (110 nm Au/29 nm Ni/110 nm Au: nanowire 1; 80 nm Au/11 nm Ni/80 nm Au: nanowire 2; 60 nm Au/2 nm Ni/60 nm Au: nanowire 3) were synthesized and used for the alignment process. The synthesized nanowires were functionalized with hexadecyltrimethylammonium bromide (CTAB) in a 0.45 CTAB aqueous solution. Repeated centrifugation, re-suspension and incubation of the nanowires to new CTAB solutions (up to 8 iterations) will ensure successful functionalization of CTAB which is evidenced by the fact that the nanowires remain in a pseudo-liquid state when centrifuged and can be easily dispersed when adding new CTAB solution (without the need for sonication).

**Silicon master and PDMS stamp fabrication.** A silicon master with positive linelet arrays was made by e-beam lithography using negative-tone resist hydrogensilsesquioxane (HSQ). A PDMS stamp (10:1 elastomer to curing agent using SYLGARD® 184 SILICONE ELASTOMER KIT) with negative trenches was made from the master by curing the elastomer

precursor at 80 °C for 3 hours. The specific dimensions of the trenches and nanowires used are summarized in Table 5.1.

**Alignment of nanowires into elastomer trenches.** A droplet (5  $\mu\text{L}$ ) of nanowire solution (0.45 mM CTAB aqueous solution) was dropped on the PDMS stamp trench region under an optical microscope. The PDMS stamp was then heated on a hot plate at 50 °C, allowing the droplet to dry while the edge of the drop moves simultaneously across the trench region. The nanowires are aligned into the trenches due to capillary forces.

**Transfer of aligned nanowires to graphene and silicon substrates.** The aligned nanowires were transferred to either a PMMA-coated graphene substrate for the fabrication of arrays of graphene nanoribbons or a PMMA-coated silicon substrate in the case of SERS-active substrate. PMMA adhesion layer and heating at 135 °C facilitate the transfer of nanowires. Arrays of graphene nanoribbons were fabricated according to a previous report.<sup>15</sup> Raman mapping for SERS was carried out on a Witec instrument using 785 nm laser with a power of ~1 mW.

### 5.3. Results and Discussion

In a typical experiment, nanowires with alternating segments of Au and Ni were synthesized electrochemically (see Methods section for details). This was followed by functionalization with hexadecyltrimethylammonium bromide (CTAB) and stabilization in a 0.45 mM CTAB aqueous solution (Figure 5.1A). The solution was then dropped onto a PDMS stamp with trenches that were made by molding the elastomer on a silicon master with raised features (Figure 5. 1B and

Figure 5.2). During the drying process (the stamp was heated at 50 °C), the droplet edge spontaneously shrank due to solvent evaporation and moved over the trench area, and the nanowires were aligned into the trenches by nanoscale capillary forces over a  $200 \times 500 \mu\text{m}^2$  area.

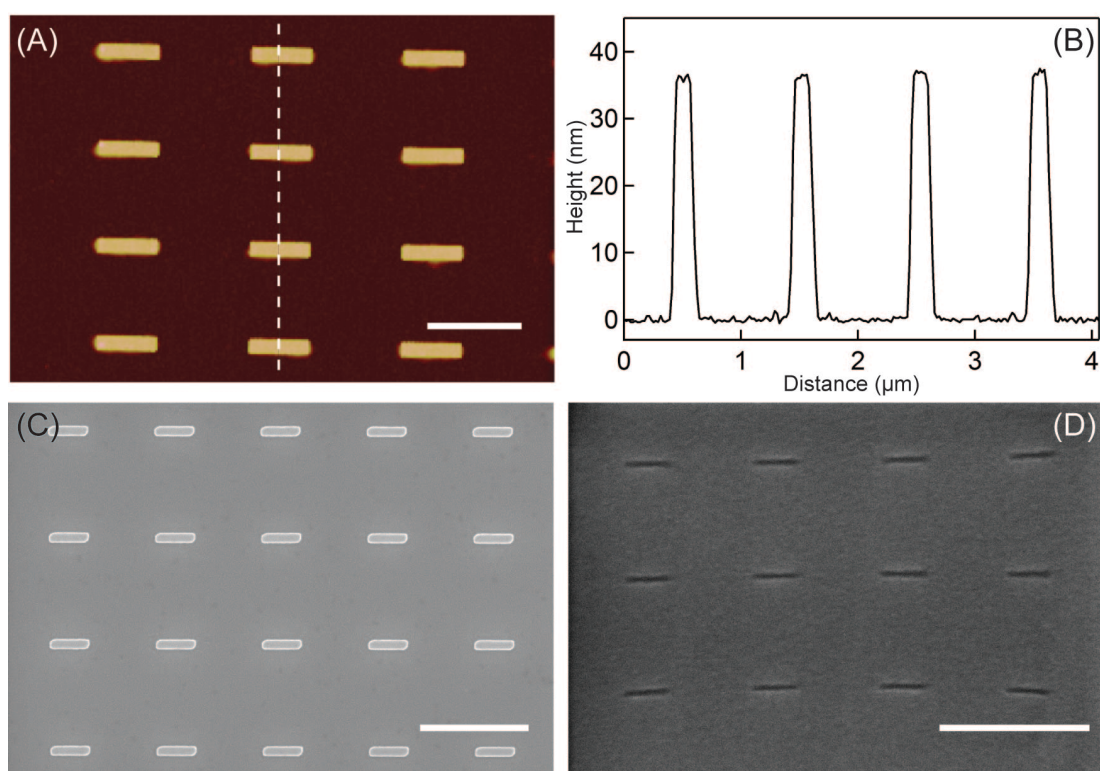


**Figure 5.2** Silicon master and PDMS stamps. AFM image (A) and height profile (B) of raised HSQ features confirm the height is  $\sim 35$  nm after E-beam patterning and development. (C) SEM image for the same raised HSQ features as in (A). (D) SEM image of the PDMS stamp with negative trenches made from molding the elastomer on the master. Scale bars: 1  $\mu\text{m}$ .

**Table 5.1:** Parameters of the nanoscale trenches for the alignment of multi-segmented nanowires

Nanowire overall length (nm)	Nanowire diameter (nm)	Trench length (nm)	Trench width (nm)	Trench depth (nm)	Alignment yield
<b>120</b>	35	300	70	35	90%
<b>180</b>	35	350	80	35	87%
<b>250</b>	35	400	80	39	85%

Electrochemically synthesized nanowires differ from many previously studied wires in that they are not capped by a surfactant. Therefore, we hypothesized that in order to reliably control the assembly of electrochemically synthesized nanowires, their surface functionality must be controlled. We selected CTAB because it has been widely used in the synthesis of gold nanoparticles as a shape directing agent and stabilizing surfactant.<sup>145-146</sup> To functionalize nanowires with CTAB, as-synthesized nanowires were rigorously washed with a 0.45 mM CTAB aqueous solution and then dispersed in the 0.45 mM CTAB solution (detailed procedures can be found in Methods section). Following functionalization, the nanowires exhibited a positive zeta potential (48 mV) and were stable in solution for up to 24 h (Figure 5.3), leading us to conclude that they were functionalized with a bilayer of CTAB.<sup>147</sup> It is important to note that if as-synthesized nanowires were used without CTAB modification, a very low yield of alignment was obtained (percentage of trenches occupied by nanowires, < 5%). Even when the nanowires were functionalized with 1,4-benzenedithiol (1,4-BDT) which provides moderate stability when transferred to 0.45 mM CTAB solution (precipitation occurred within 3 h), a typical alignment yield was still less than 20%.

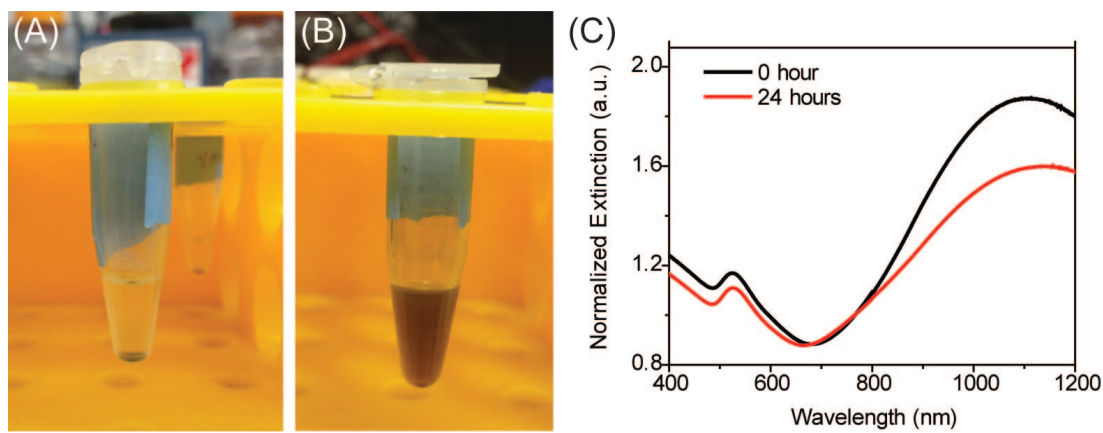


**Figure 5.3** Comparison of electrochemically-synthesized nanowires (A) before and (B) after CTAB functionalization. The nanowires that were not functionalized with CTAB using the aforementioned process settle to the bottom within a few hours (A). The CTAB-functionalized nanowires were well-dispersed without settling for up to 24 hours (B). (C) UV-Vis spectra of CTAB-functionalized nanowires as-prepared and after sitting for 24 hours show good stability.

Next, we evaluated the potential of using PDMS with well-defined trenches to align multi-segmented nanowires with different compositions and lengths (Figure 5.4A, C-E). Through experimentation, we found that the alignment yield is very sensitive to the dimensions of the trenches. In order to optimize the alignment, including yield, orientation and transfer rate, trenches of varying dimensions were systematically assessed. For 250 nm long nanowires, trenches that vary from 350 to 450 nm in length, from 70 to 120 nm in width, and from 35 to 50 nm in depth were studied. High alignment yield ( $> 85\%$ ) was achieved when trenches of 400 nm $\times$ 80 nm $\times$ 39 nm dimensions were used (Figure 5.4A). The trenches must be larger than the nanowires (with a length of 250 nm and a diameter of 35 nm) for two reasons. First, larger trenches can provide a stronger capillary force and therefore increase the contact line pinning effect,<sup>148</sup> which is important in the control of droplet evaporation dynamics by obtaining a slow shrinking speed ( $\sim 2 \mu\text{m/s}$ ) so that nanowires have enough time to be trapped. Second, because of the disordered arrangement of the nanowires at the droplet edge (Figure 5.5A), a larger trench is needed to provide extra room for the nanowires to adjust orientation and fit within it. Interestingly, 95% of the nanowires were aligned by capillary immersion forces<sup>142</sup> to the corners of the trenches in the same direction as that of the moving droplet edge. As a result, a narrow angle distribution was obtained, with 92% of the nanowires aligned within  $10^\circ$  with respect to vertical (Figure 5.4B).

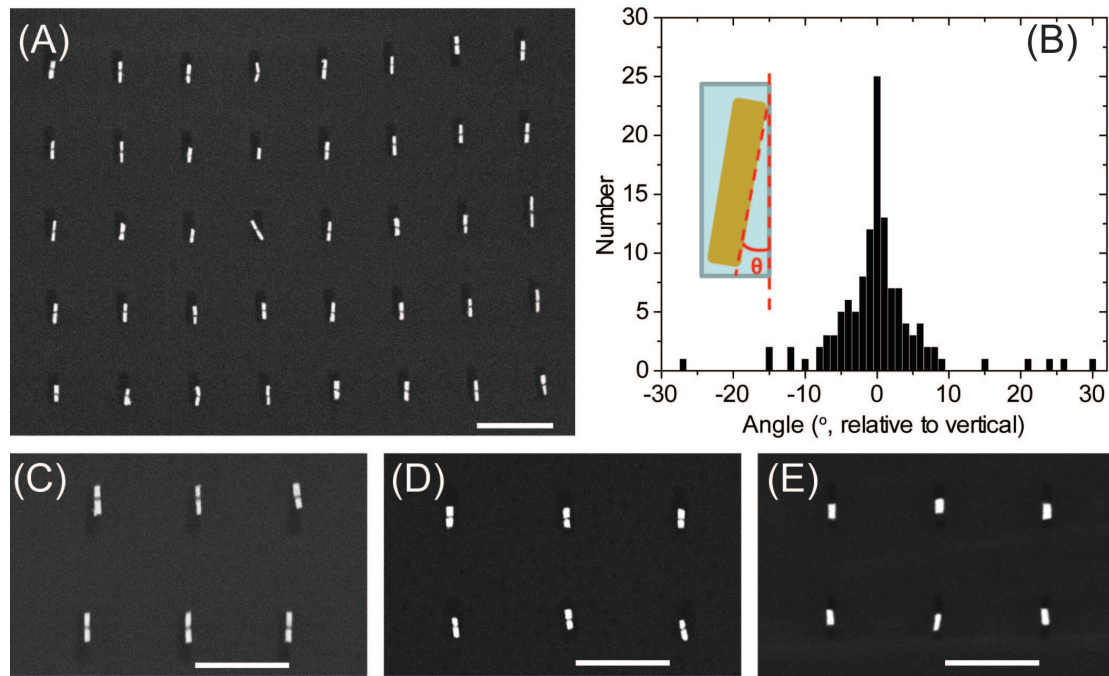


**Figure 5.4** Representative SEM images and angle statistics of the aligned multi-segmented nanowires. (A) Array of aligned nanowires consisting of two Au segments separated by a short Ni segment. (B) Distribution of the orientation of aligned nanowires with a length of 250 nm. The inset schematic shows how the alignment angle  $\theta$  is measured. The width of the histogram bar is  $1^{\circ}$ . (C-E) Arrays of nanowires with a diameter of 35 nm and consisting of Au and Ni segment with different lengths: (C) Total length:  $252 \pm 24$  nm, Ni segment:  $29 \pm 4$  nm, aspect ratio: 7; (D) Total length:  $177 \pm 9$  nm, Ni segment:  $11 \pm 3$  nm, aspect ratio: 5; (E) Total length:  $125 \pm 8$  nm, Ni segment:  $2 \pm 0.4$  nm, aspect ratio: 3.5. Scale bars: 1  $\mu\text{m}$ .

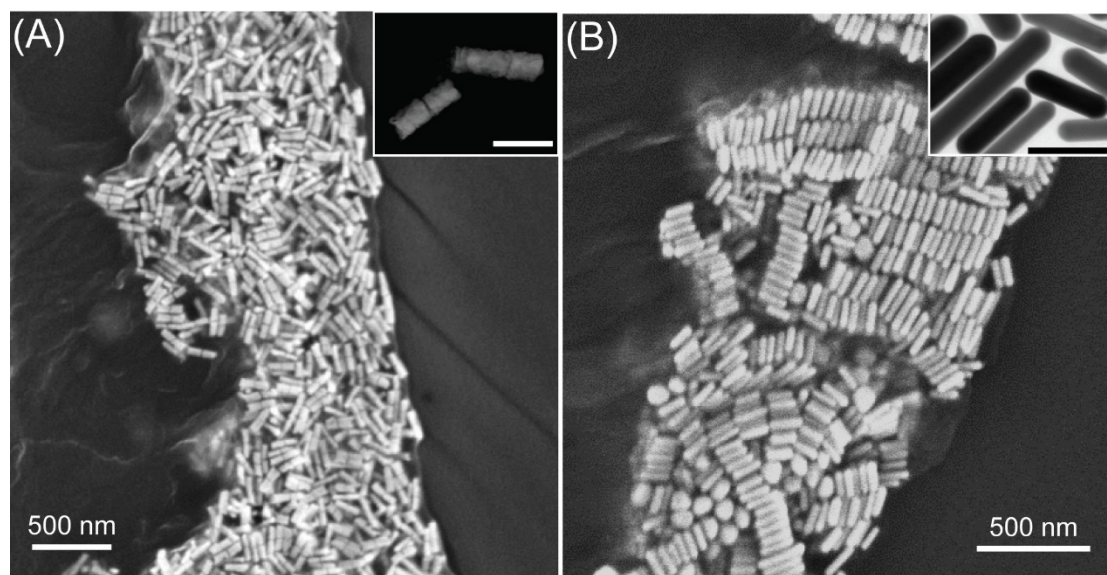


**Figure 5.5** SEM image comparison of the accumulation zone of nanowires synthesized through (A) the OWL method and (B) surfactant-mediated chemical reduction method. (A) Disordered domains are formed due to rough wire surfaces (Inset, TEM image) of the multi-segmented nanowires. (B) Ordered domains are formed due to accumulation of the nanorods with atomically smooth surfaces (Inset, TEM image). Inset scale bars: 80 nm.

To test the generality of the technique, we prepared a set of gapped nanowires with an average diameter of 35 nm and lengths varying between 120 and 250 nm and studied their assembly behavior in the PDMS with well-defined trenches (Figure 5.4C-E). The nanowires have aspect ratios (defined as L/D, where L and D is the length and diameter of the nanowire) varying between 3.5 and 7. All of the wires could be aligned on the PDMS substrates in high yield, provided the appropriate trench architectures were used, as summarized in Table 5.1. Specifically, the length and width of the trench should be ca. 150 and 40 nm larger than those of the nanowires, respectively, in order to obtain high yield. The successful alignment of nanowires with an aspect ratio of 7, larger than previously reported value of 3, is particularly encouraging since it opens possibilities for assembling nanowires that are exceedingly long (e.g., silicon nanowires<sup>149</sup>) and important for applications such as electronics. Different functionalization protocols may be needed owing to different surface chemistries for other types of nanowires but conceptually the technique should be extendible to other compositions.

Remarkably, we obtained high-yield alignment of the nanowires even though a disordered phase was formed for multi-segmented nanowire aggregates at the droplet edge (Figure 5.5A). In a study where chemically synthesized rod-like nanoparticles with an aspect ratio of 3 were used, the formation of an ordered crystalline phase was argued to be a prerequisite for the high-yield alignment of wires.<sup>144</sup> However, in our study, the electrochemically synthesized multi-segmented nanowires have rough surfaces due to the rough pores in the AAO template<sup>150</sup> (Figure 5.5A,

inset). As a result, it is difficult for the nanowires to pack closely and form ordered phases (Figure 5.5A). This is in contrast to that of many chemically synthesized nanorods that possess atomically flat surfaces, which facilitate the formation of crystalline phases (Figure 5.5B). In our study, we found that nanowires started to be trapped when the contact angle of the droplet is very small (i.e.,  $\sim 20^\circ$ ). The assembly of spherical nanoparticles has indeed been reported at such low contact angles.<sup>151</sup>

Thus far, we have primarily discussed segmented wires, but gapped nanowires can also be prepared using a variant of the aforementioned method. For example, segmented wires consisting of alternating Au and Ni segments can be transferred to desired substrates through micro-contact printing<sup>144</sup> (Figure 5.6A). In typical experiments, prior to the transfer, the substrate ( $\text{SiO}_2$  in this case) was spin-coated with a thin film (ca. 20 nm) of PMMA (495K, Microchem) which serves as an adhesive layer to promote a wire high transfer yield (> 95%), and secures the positions of the nanowires to prevent them from migrating during subsequent processing steps. The role of the PMMA is analogous to that of the silica backing layer in conventional OWL.<sup>125</sup> The nanowires were then transferred to the target substrate by heating it to 135 °C and applying pressure to the PDMS stamp against the substrate for 1 min (Figure 5.6A, i), followed by air cooling to room temperature and removal of pressure (Figure 5.6A, ii). After the transfer, Ni was etched in an HCl aqueous solution and gapped nanowire arrays were created (Figure 5.6B).

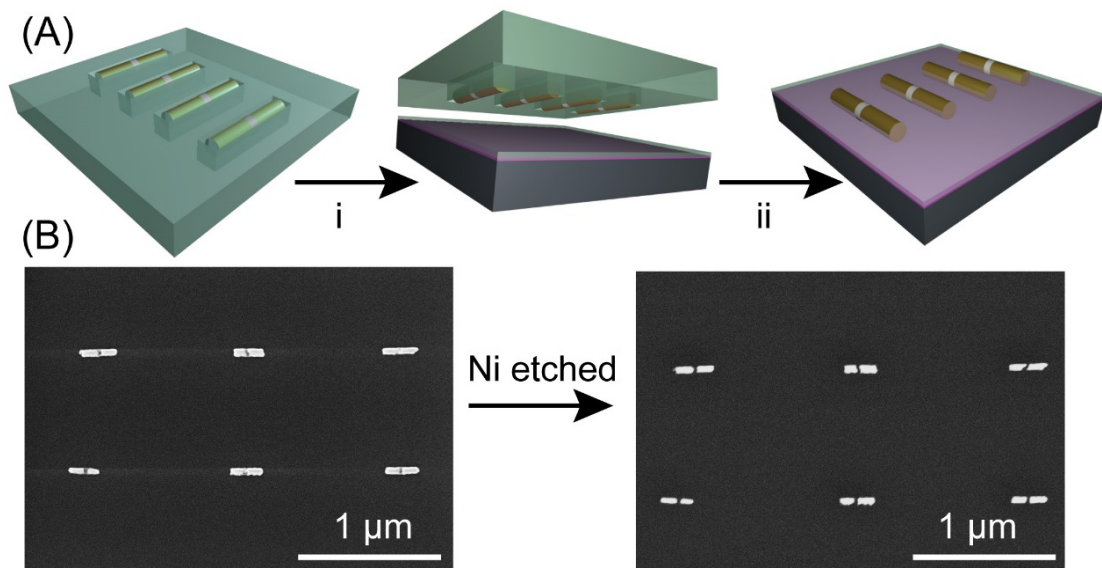


**Figure 5.6** Transfer of multi-segmented nanowire arrays to a target substrate (e.g., graphene) by micro-contact printing. (A) (i) Positioning nanowire arrays on top of graphene with a home-made micro-manipulator. (ii) Nanowires are transferred by applying pressure on the stamp against the target substrate at 135 °C. (B) SEM images of the transferred nanowires on a single layer of graphene, before and after Ni etching. The registry of Au segments is maintained.

Finally, we explored two applications for the transferred nanowires. Following the strategy of our previous work,<sup>135</sup> an array of gapped GNRs was fabricated using the aligned gapped nanowires as etch masks. As described above, the nanowire arrays were first transferred to a PMMA-coated graphene sample (Figure 5.7), followed by Ni etching and gap formation. Thereafter, the graphene sample was etched with reactive ion etching, and then sonicated in acetone to remove the remaining PMMA and reveal the gapped GNRs (Figure 5.8A). The gap size in these nanoribbons is ~25 nm, matching the length of the Ni segment in the nanowires. The ribbon array was further characterized by Raman mapping (Figure 5.9). This aligned array of GNRs affords interesting graphene structures that may prove useful for electronics<sup>136-137</sup> and plasmonics<sup>138-139, 152</sup> considering that the gap size, ribbon length and ribbon-to-ribbon distance are highly adjustable.

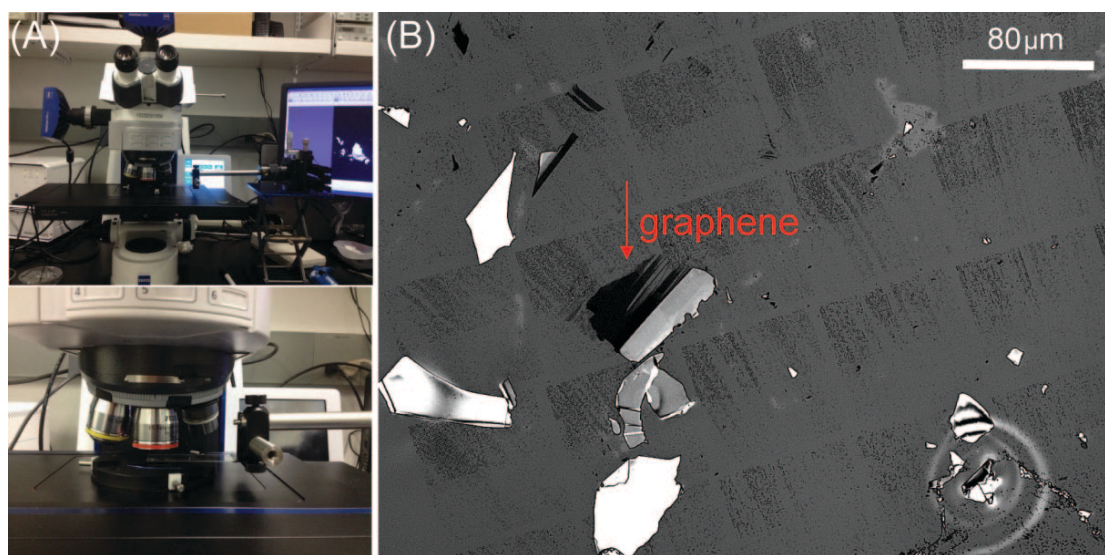


**Figure 5.7** (A) Homemade apparatus for positioning aligned nanowires on a graphene sheet. The apparatus allows one to control registry of the nanowire array and target substrate. (B) Optical image of the transferred nanowires on a few-layer graphene flake made by mechanical exfoliation.

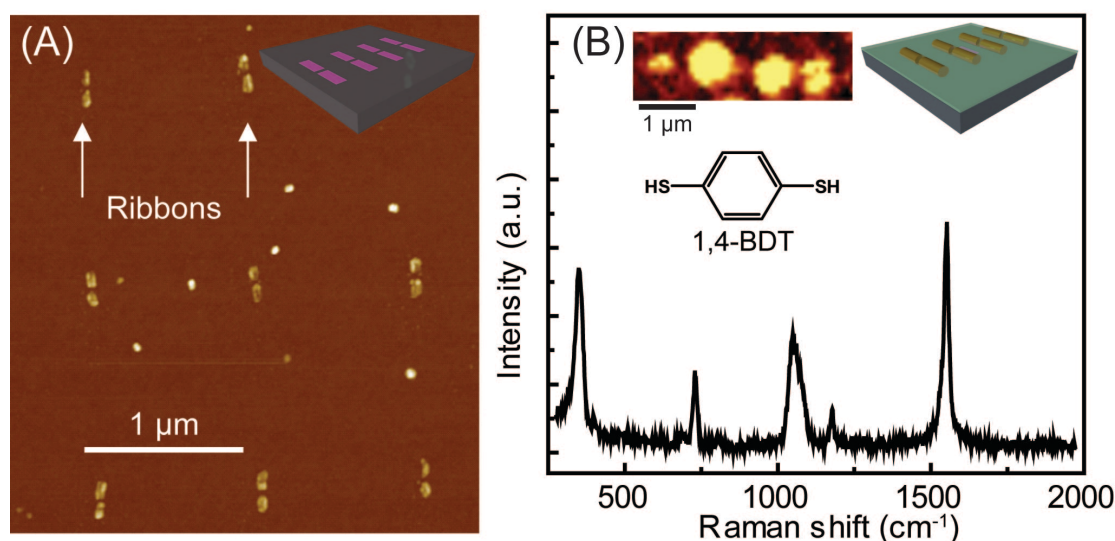


**Figure 5.8** Fabrication of gapped graphene nanoribbons and SERS substrate. (A) Aligned graphene nanoribbons generated by using the gapped nanowires from Figure 4B as etch masks. Nanoribbons 200 nm long with a gap of ~25 nm were fabricated. (B) A SERS measurement of 1,4-BDT from aligned gapped nanowires. A row of hot spots is shown in the top-left inset. a.u., arbitrary units.

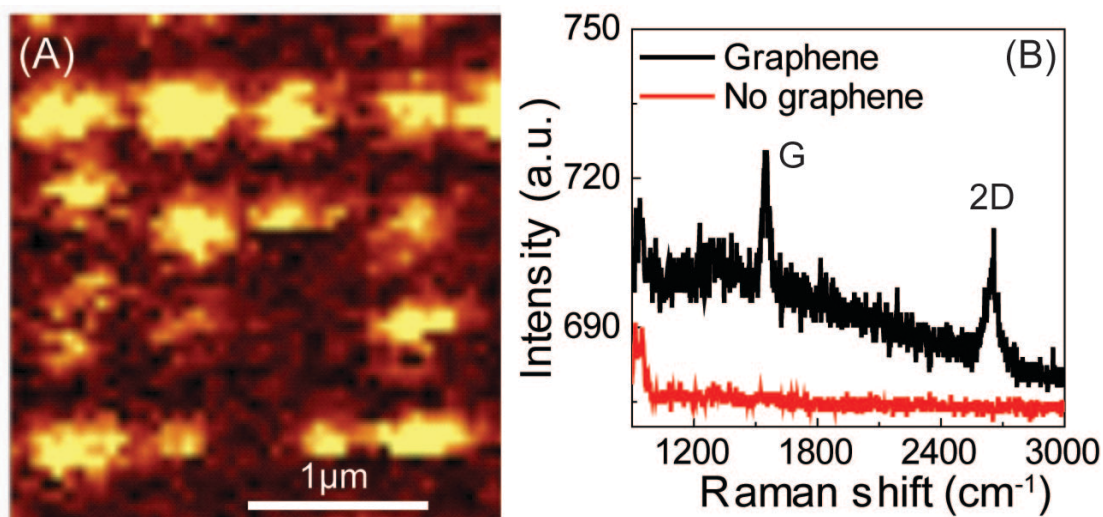


**Figure 5.9** (A) Raman mapping of aligned graphene ribbons. (B) Spectra of ribbon regions and background in (A) show clear G and 2D peaks from the graphene ribbons.

Another important application of these nanowires is to utilize them as SERS substrates. As proof-of-concept, nanowires consisting of two 60 nm gold segments and a 2 nm Ni segment were designed and synthesized. Alignment of the nanowires on a PMMA-coated silicon substrate and etching of the Ni segments yielded arrays of Au dimer structures with a plasmon resonance centered at 785 nm, matching that of the laser wavelength used in the Raman measurement. The gold nanostructures were then functionalized with 1,4-BDT by incubating the substrate in an ethanol solution (~1 mM) for 12 h. These nanostructures have been previously shown to be local amplifiers for surface-enhanced Raman scattering with enhancement factors of  $7 \times 10^8$ .<sup>153</sup> Raman mapping clearly reveals strong SERS signals (eg. C-C stretch mode at ~1561 cm<sup>-1</sup>) from 1,4-BDT when the laser is scanned across the array (Figure 5.8B). It's worth mentioning that the density of nanowires can be adjusted by simply changing the trench design (Figure 5.10). Thus, the aligned gapped nanowires provide a route to new SERS substrates with uniform distributions of hot spots that can be used for a variety of chemical and biological sensor applications.<sup>154</sup>

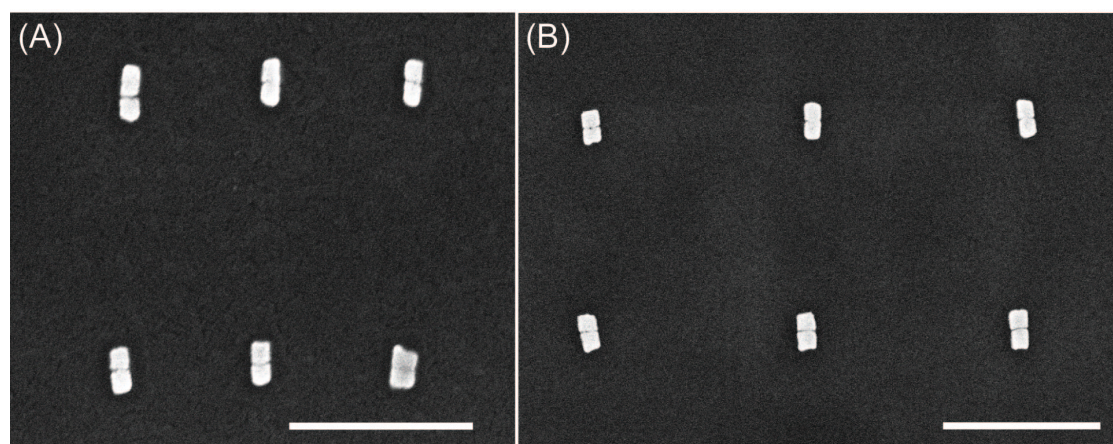


**Figure 5.10** Density control of the aligned nanowires. SEM images of aligned nanowires that were transferred to a Si substrate with (A) a lateral pitch of 400 nm and a vertical pitch of 700 nm and (B) a lateral and vertical pitch of 700 nm. Scale bars: 500 nm.

#### 5.4. Conclusions

In summary, we have developed a large-area alignment strategy for electrochemically-synthesized multi-segmented nanowires with control over position, orientation and density by using a nanoscale capillary force-mediated assembly method. Importantly, we are able to align nanowires with different gap sizes, lengths, and aspect ratios. The high-yield alignment of nanowires with an aspect ratio as large as 7 is particularly encouraging for many applications that require high aspect-ratio nanostructures. As one of the critical conditions for the alignment, the excellent wire dispersibility by CTAB functionalization is promising for many other types of nanostructures that are synthesized without surfactant modification, for example Si nanowires<sup>149</sup> and ZnO nanorods.<sup>155</sup> The proof-of-concept experiments demonstrating the fabrication of arrays of graphene nanoribbons and SERS substrates make the technique particularly attractive to researchers who require these kind of structures for a variety of electronic, spectroscopic, and plasmonic applications.<sup>152, 156</sup>

# **Chapter 6**

## **Shape-Selective Deposition and Assembly of Anisotropic Nanoparticles**

Portions of this chapter have been published in: *Nano Letters*, 2014

This work was done in collaboration with Dr. Xiaozhu Zhou

## 6.1. Introduction

Noble metal nanostructures have been the focus of intense research, in part because of their localized surface plasmon resonances (LSPRs) and their ability to be used as optical probes in a variety of chemical and biological detection schemes.<sup>134, 153-154, 157</sup> The way such structures interact with light is strongly dependent upon their position and orientation relative to other nanoparticles.<sup>158-160</sup> Top-down approaches, including electron-beam and focused-ion beam lithography, have enabled the fabrication of arrays of metal nanostructures with deliberately varied shapes and configurations, opening avenues to both fundamental investigations and applications.<sup>161-162</sup> However, these lithographic techniques suffer from some inherent disadvantages. First, because of their serial nature, it is often time-consuming and inefficient to fabricate large area patterns which are required in many applications including photonic devices.<sup>163</sup> Second, lithographically defined metal nanostructures are often polycrystalline, resulting in LSPRs with low quality factors.<sup>164-165</sup> Additionally, it is not possible to use lithographic techniques to fabricate certain three dimensional shapes, such as spheres or concave cubes. In contrast, solution-based syntheses can be used to produce large quantities of colloidal nanostructures with a wide variety of shapes, sizes, and compositions. However, the major challenge in utilizing such solution-synthesized nanoparticles in solid-state devices is positioning them on substrates with sufficiently high resolution and control over their position and orientation. One approach is to assemble nanoparticles through pick-and-place techniques such

as optical tweezing<sup>166</sup> or dielectrophoretic trapping,<sup>166-168</sup> but these serial methods are not amenable for high throughput assembly. Recently, demonstrations of template-assisted assembly utilizing capillary forces,<sup>142-143</sup> electrostatic forces,<sup>169</sup> gravitational forces,<sup>170</sup> or molecular recognition,<sup>171-172</sup> have shown great promise for the large-area assembly of nanoparticles with single particle resolution.<sup>122</sup> Importantly, theoretical studies<sup>173</sup> have predicted the possibility of trapping and aligning a variety of anisotropic nanoparticles in pre-defined templates with control over their orientation, but little has been explored experimentally.<sup>144</sup>

In this letter, we report the capillary-force based templated assembly of single crystalline colloidal gold nanoprisms and concave nanocubes with control over their position and orientation. Through a systematic study of template geometry, we elucidate the geometrical parameters of a template that are required to immobilize nanoprisms and concave nanocubes in high yield. The results of this study enable us to construct templates that can be used to immobilize nanoprisms in the presence of a majority population of spherical nanoparticle impurities, allowing for purification and assembly in a single step. Finally, we fabricate templates that allow one to immobilize two particles in close proximity in an effort to study the role of the immersion force (a type of capillary force between two particles<sup>174</sup>) in the assembly process. We find that the immersion force plays an important role in the formation of face-to-face cube dimers while it is less important for edge-to-edge cube dimers and nanoprism-based bowties. Finally, the ability to control particle orientation within pair structures allows us to

utilize the face-to-face nanocube dimer structures as enhancers of Raman scattering and compare the polarization dependence of the resultant signal with numerical simulation.<sup>175</sup>

## 6.2. Experimental Section

**Synthesis of Au nanoprisms and concave nanocubes.** Synthesis of Au nanoprisms and concave nanocubes followed previously reported surfactant-mediated methods.<sup>134, 153</sup>

**Silicon master and PDMS trench substrate fabrication.** Negative-tone electron beam lithography (EBL) resist hydrogensilsesquioxane (HSQ) layers of varying thickness were spincoated onto silicon substrates. Subsequent EBL was utilized to define positive triangular and square features on a silicon wafer. The experimental film thicknesses, spin coating speeds and concentrations of HSQ in methyl isobutyl ketone (MIBK) are summarized in Table 6.1.

After baking the HSQ-coated wafers at 250 °C for 2 min, EBL was carried out using an FEI Quanta FESEM equipped with the Nanometer Pattern Generation System (NPGS, JC Nabitity Lithography System, Bozeman, MT, USA) using a 30 kV acceleration voltage and 150 pA beam current. The patterned master was then soaked in MF-319 developer for 60 s followed by rinsing with DI water for 30 s. The final master was made hydrophobic by silanization with vapor coating of 1H,1H,2H,2H –perfluorodecyltrichlorosilane.

Polydimethylsiloxane (PDMS) stamps (10:1 elastomer to curing agent using SYLGARD® 184 SILICONE ELASTOMER KIT) with negative trenches were made by molding the elastomer precursors on the silicon master, curing at 80 °C for 3 hours and peeling off the cured

PDMS. The depth of the trenches on the PDMS surface was equal to the thickness of the resist used for EBL.

**Raman measurement and FDTD simulation.** Raman measurements were carried out using a Witec instrument using 785 nm laser with a power of ~1 mW. The laser polarization was manually adjusted to match longitudinal and transverse orientation of the cube face-to-face dimers.

**Finite-difference time-domain (FDTD) simulation.** FDTD simulations were performed with a commercial package (Lumerical FDTD solutions v.8.5.4). The dielectric functions of Au (cubes) and silicon (substrate) were taken from the experimental data collected by Johnson and Christy and the material handbook by Palik, respectively. The gap size in the face-to-face cube dimer was 4 nm, which matches the thickness of the CTAB layers on the cubes. Highest intensity enhancement factor ( $|E_{\text{local}}/E_{\text{incident}}|^2$ ) was calculated by averaging nine elements around the pixel of highest enhancement.

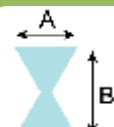
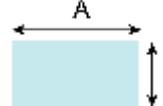
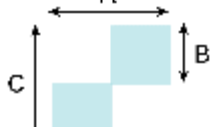
**Table 6.1:** Spin coating conditions for HSQ resist film

Resist thickness (nm)	HSQ concentration (in MIBK)	Spincoating speed
20	1%	2000 rpm
30	2%	4000 rpm
100	6%	4000 rpm

**Table 6.2:** Parameters for individual particle alignment

<b>Particle shape</b>	<b>Particle edge length (nm)</b>	<b>Trench shape</b>	<b>Trench edge length (nm)</b>	<b>Trench depth (nm)</b>
<b>Prism</b>	100	Triangle	150	20,30
<b>Prism</b>	140	Triangle	180	20
<b>Concave cube</b>	100	Square	180	100

**Table 6.3:** Parameters for nanoparticle dimer alignment

Dimer type	Particle edge length (nm)	Trench shape	Trench dimensions (nm)	Trench depth (nm)
<b>Bowtie</b>	100		A = 150 B = 230 or 250	30
<b>Concave cube (face-to-face)</b>	100		A = 240 B = 170	100
<b>Concave cube (edge-to-edge)</b>	100		A = 350 B = 180 C = 350	100

### 6.3. Results and Discussion

In a typical capillary assembly experiment, a solution of nanoparticles is placed onto a polydimethylsiloxane (PDMS) substrate with an array of trenches and allowed to dry at elevated temperatures (Figure 6.1). PDMS substrates are prepared by fabricating an array of pillars using electron beam lithography and utilizing this structure as a master to mold PDMS (details can be found in Supporting Information). A 5  $\mu\text{l}$  volume of gold triangular nanoprisms<sup>176-177</sup> (edge length of 100 nm and a concentration of 50 pM) dispersed in an aqueous 0.45 mM CTAB solution are then pipetted onto the PDMS substrate and allowed to dry at 40 °C (Figure 6.1). As the droplet evaporates, a convective flow brings nanoprisms to the contact line<sup>178</sup> and a region consisting of densely packed particles forms (Figure 6.2). As the droplet shrinks, this densely packed region slides across the template, allowing nanoprisms to settle into trenches and become trapped.

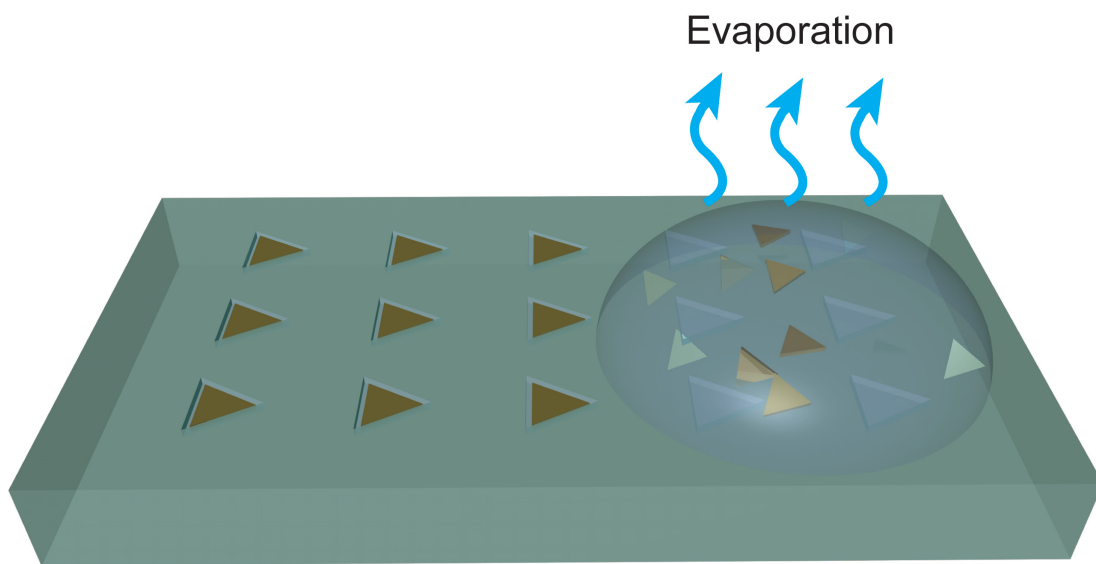


**Figure 6.1** Schematic process of large-area, shape-selective assembly of Au nanoprisms into pre-defined triangular trenches on a PDMS stamp. During the evaporation of the nanoprism solution droplet at 40 °C, a dense packing zone of nanoprisms is formed at the drop edge. The prisms in the packing zone are immobilized in the templates due to capillary forces present when the drop shrinks and moves over the trench area.

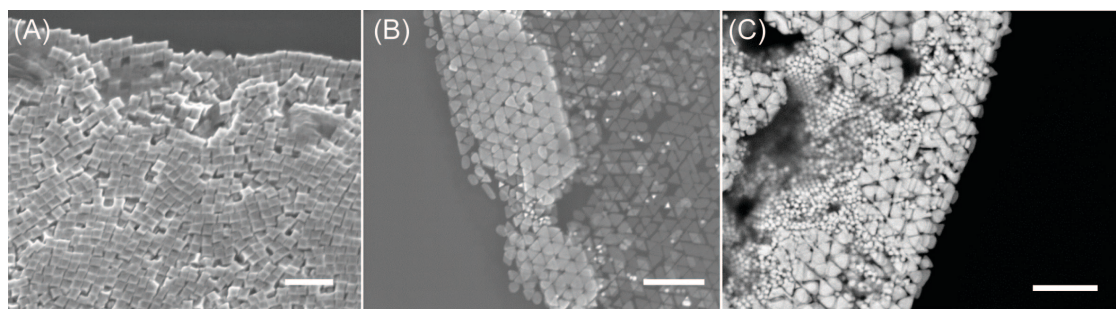


**Figure 6.2** SEM images of the dense packing zones of nanoparticles at the drop edge. (A) Concave nanocubes. (B) Nanoprisms after purification. (C) As-synthesized nanoprisms with impurity spherical nanoparticles. Scale bars: 500 nm.

By rationally designing templates for a given anisotropic nanoparticle, we find it is possible to immobilize single nanoparticles in high yield. Importantly, by systematically evaluating the assembly efficiency of substrates with different trench geometries, we find that trench depth is a crucial parameter. Specifically, for 100 nm edge length nanoprisms that are 7.5 nm thick, trenches less than 20 nm thick did not provide reliable immobilization. In contrast, trenches with a depth of 20 nm or deeper resulted in high yield assembly (~80% of the templates were occupied by one nanoprism) (Figure 6.3 and 6.4A). Another important parameter was the edge length of the trench. For 100 nm edge length prisms, trenches with edge lengths less than 150 nm were insufficient for reliably immobilizing nanoparticles. The large trenches not only provide excess space for nanoprisms to adjust their orientation to fit but also result in sufficient pinning force to trap the nanoprisms.<sup>179</sup> Importantly, with properly designed templates, the standard deviation of the angular distribution could be reduced to  $\pm 6^\circ$  (Figure 6.4C).

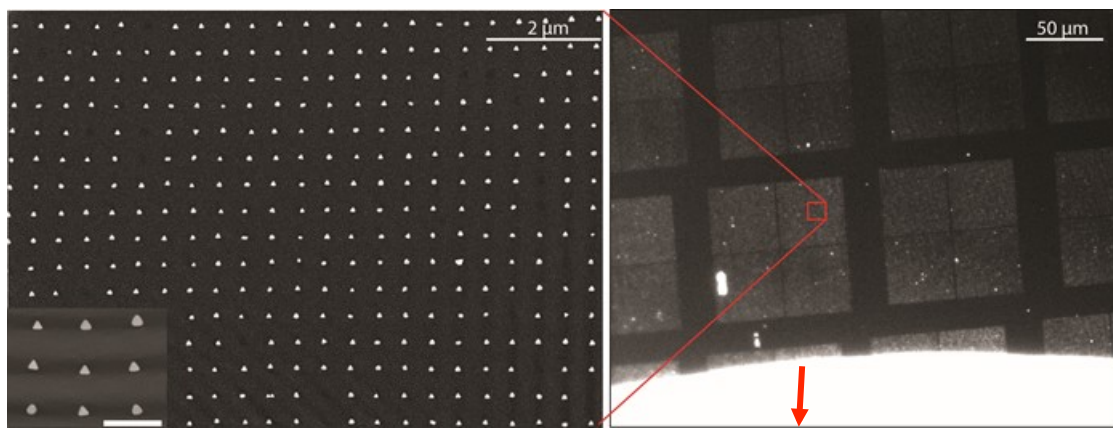


**Figure 6.3** Large-area assembly of gold nanoprisms with control over the angular position. SEM image (left) shows an array of mostly single nanoprism assembled in triangular templates with inset that highlights the control over angular orientation. Scale bar: 500 nm. The dark-field microscope image (right) shows the downward movement (as shown by the arrow) of a drop edge across the template regions as water evaporates.

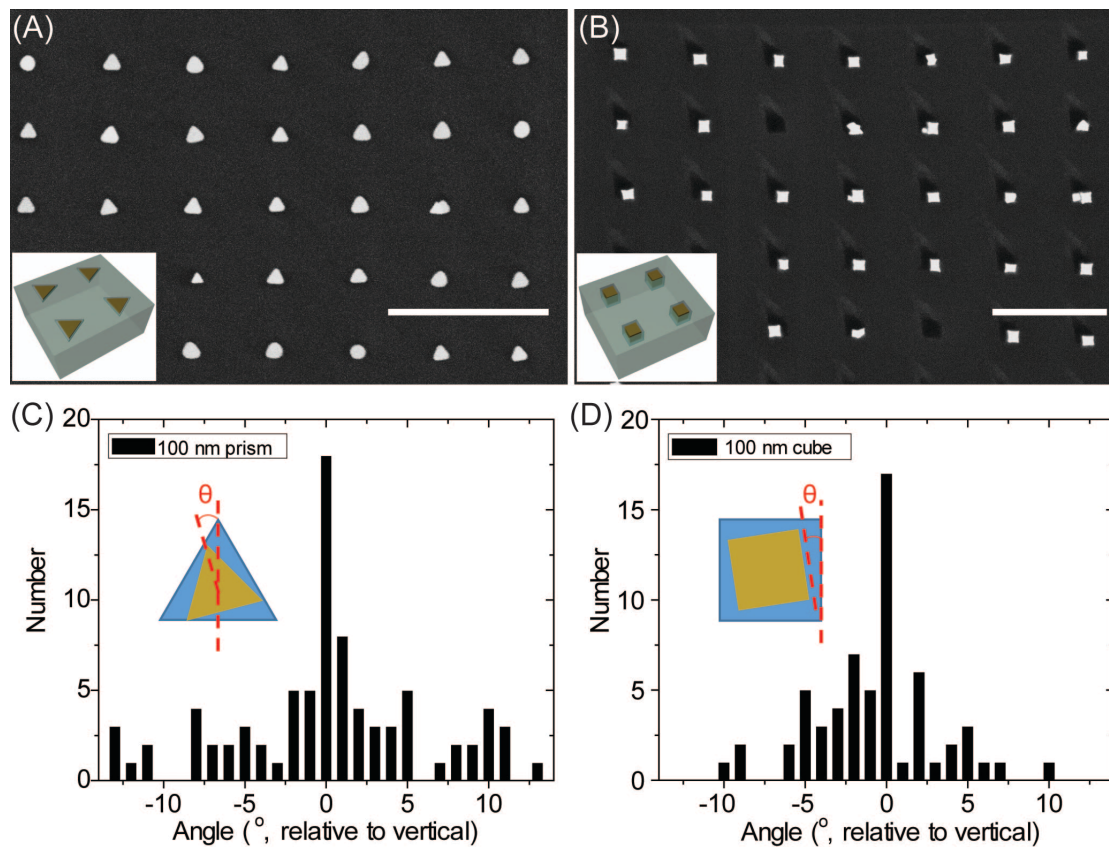


**Figure 6.4** Representative SEM images and angular statistics of the assembled Au nanostructures. Arrays of (A) nanoprisms and (B) concave nanocubes with edge lengths of 100 nm assembled on PDMS substrates. Insets show schematics of nanoprisms and cubes aligned to triangular and square templates. Scale bars: 1  $\mu$ m. Angular statistics of the (C) nanoprism and (D) concave nanocube within the templates show narrow orientation distributions within  $\pm 6^{\circ}$  and  $\pm 5^{\circ}$ , respectively. Insets show how the angular orientation is defined.

Having demonstrated the assembly of nanoprisms on triangular templates, we next investigated if a similar strategy could be used to assemble concave nanocubes in square templates. In addition to the geometric difference between the triangular nanoprisms and cubes, they are characterized by very different aspect ratios (prisms ~13 and cubes ~1), so it is not obvious that the same geometric relationships will hold. Indeed, while 7.5 nm thick prisms required trenches approximately three times deeper than their thickness, nanocubes were assembled in high-yield (>85%) when the template depth was commensurate with the 100 nm cube thickness (Figure 6.4C). This may suggest that there are fluctuations in nanoparticles when they are in the solution due to Brownian motions, and that a shallow template (10 nm in depth) cannot efficiently trap particles regardless of the particle size.

Since different trench depths are required to assemble different particle geometries, we hypothesized that trenches of different specified depths may allow one to purify mixtures of particles, thus achieving shape selective particle assembly. This is an important issue in the context of seed-mediated nanoparticle synthesis techniques,<sup>145, 176, 180</sup> as these methods frequently result in a mixture of particles that contain the desired product shape as well as various shape impurities. The synthesis of triangular nanoprisms is an excellent example of this, as this particle shape is always synthesized in the presence of an excess of spherical nanoparticles that can be challenging to remove using conventional purification techniques.<sup>176</sup> While depletion force-based and DNA-mediated methods<sup>176</sup> have been developed to extract the prisms in high purity,

both represent extra steps that could be avoided using a well-designed template that would combine the purification and assembly processes into a single step. In order to test this selective templating hypothesis, we performed an assembly experiment using a substrate with an array of 20 nm deep triangular trenches using an as-synthesized solution containing both nanoprisms (140 nm edge length) and spherical nanoparticle impurities (35 nm diameter, Figure 6.5A, B). By utilizing 20 nm deep trenches, we find high yield assembly of nanoprisms with no observed spherical particles (Figure 6.5C). This result is in agreement with our previous finding that there is a minimum depth needed to trap a given particle. While 20 nm is sufficient for trapping 140 nm nanoprisms, it is clearly insufficient for trapping 35 nm spheres. As reported in literature<sup>142</sup> the trenches are filled with liquid when the droplet moves over them. Since the thickness of the nanoprisms (7.5 nm) is smaller than the depth of the trenches (20 nm), it is energetically favorable for the nanoprism to be trapped without exposing any of their surface to air. However, since the diameter of spherical nanoparticles (35 nm) is much larger than the trench depth, their trapping is unfavorable due to an additional particle-air surface energy term created by the shallow trenches.

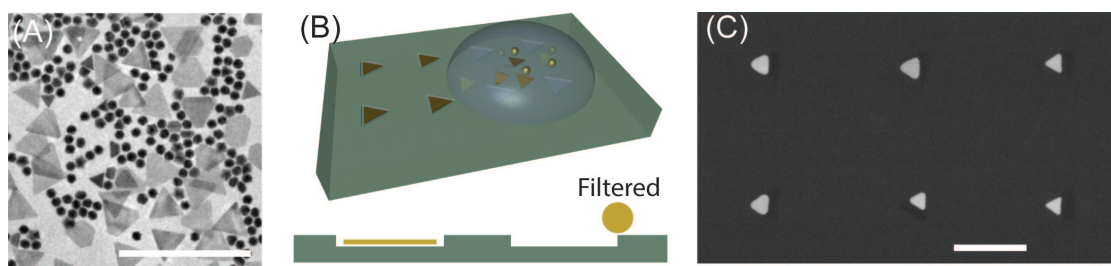


**Figure 6.5** Shape-selective template-assisted assembly and purification of nanoprisms. (A) TEM image of the product of the Au nanoprism synthesis containing nanoprism products (edge length: 140 nm, thickness: 7.5 nm) and spherical nanoparticle impurities (diameter: 35 nm). (B) Schematics showing that gold nanoprisms are selectively assembled to the shallow triangular templates while spherical nanoparticles with a much larger diameter are not. In the bottom scheme, the particles and trenches are to-scale. (C) SEM image of the assembly of as-synthesized nanoprisms into 20 nm deep templates. No spherical particles were found in a template area consisting of two thousand templates. Scale bars: 500 nm.

Thus far, we have focused on immobilizing individual particles. It would be more interesting to bring these nanostructures into close proximity and with control over particle orientation because then they could couple plasmonically, electronically and magnetically in a controlled fashion.<sup>122, 175, 181</sup> Specifically, we investigated the behavior of the hybridized LSPR modes for dimer structures of these nanoparticles. Thus, we designed and fabricated trenches that can accommodate three types of dimer structures based on the particles that were assembled previously (*vide supra*): face-to-face (FF) concave cubes, edge-to-edge (EE) concave cubes, and nanopism bowties (BT) (Table 6.3 and Figure 6.6). After assembling these structures, we observed that the individual cubes in the FF structures were separated by a small distance while the nanoparticles in the EE and BT structures were separated by a much larger distance that varied between 45 and 120 nm (Figure 6.6). We hypothesize that this result is a manifestation of the competition between the interparticle immersion force, which draws particles together, and the trench-particle capillary force, which draws particles towards the walls of the trenches. Specifically, for the FF structures the surface area overlap between the two particles was sufficiently large such that the interparticle immersion force dominated (methods for calculating this force can be found in Ref. 178). However, in the case of the EE and BT structures, the surface area overlap between the two particles was relatively small, resulting in an interparticle

immersion force insufficient to move them toward each other. Accordingly, the cubes in the FF dimers (Figure 6.6A) were too close to accurately measure their separation, in agreement with our prediction that they would come as close to touching as sterically permitted by their ligands. The finding that the immersion force is highly dependent upon the surface area overlap between particles is instructive and needs to be taken into account when one intends to assemble particles of particular shapes into desired configurations using this capillary- and trench-based approach.

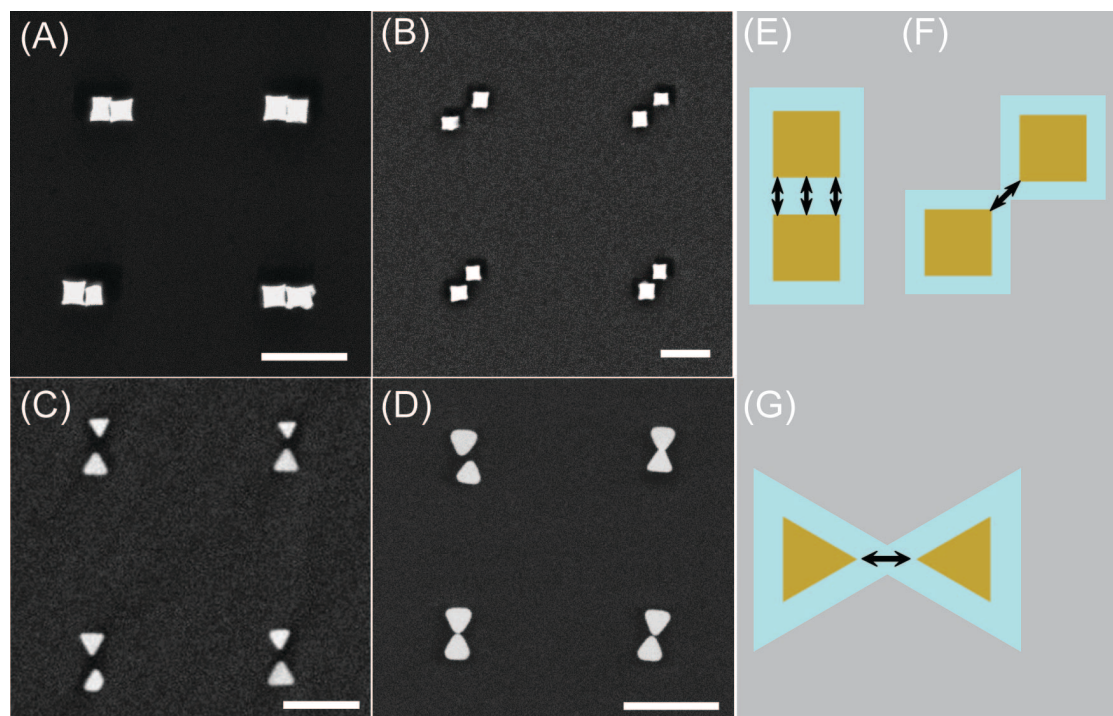


**Figure 6.6** Representative SEM images of nanoparticle dimers consisting of concave cubes (A: face-to-face; B: edge-to-edge) and nanoprism bowties (C, D). Scale bars: 500 nm. Large immersion forces between the cubes in the face-to-face dimers (E) are responsible for pulling the cubes together to form intimate contact, while smaller immersion force between the cubes in the edge-to-edge dimers (F) and prisms in the bowties (G) do not pull the individual particles together.

The assembly method provides a straightforward way to prepare dimer structures on substrates for subsequent property investigations. In particular, the small interparticle distance provides a good platform for studying SERS which arises from the coupling between the particles with gaps as small as a few nanometers. Herein, we studied the SERS of 1,4-benzenedithiol (1,4-BDT) functionalized on concave nanocube FF dimers in which small gaps can be prepared. Importantly, because of the anisotropic arrangement of particles in this pair structure, one may expect the polarization dependence of the SERS enhancement to be significant. Indeed, we observed a markedly larger SERS intensity for 1,4-BDT when the light was polarized longitudinally to the dimer (top spectrum, Figure 6.7A) as compared to light polarized in the transverse orientation (bottom spectrum, Figure 6.7A). To further explore this phenomenon, finite-difference time-domain (FDTD) simulations were performed to understand the spatial distribution of electromagnetic field under our two polarization conditions (Figure 6.7B-E). In all calculations, the wavelength of the incident light was 784.5 nm. Consistent with our experiment, the simulation predicts that the highest SERS enhancements  $|E_{\text{local}}/E_{\text{incident}}|^4$  are  $10^{6.6}$  and  $10^{5.6}$  for the longitudinal and transverse polarizations, respectively (Figure 6.7B-E), indicating a factor of 10 difference in the SERS intensity.

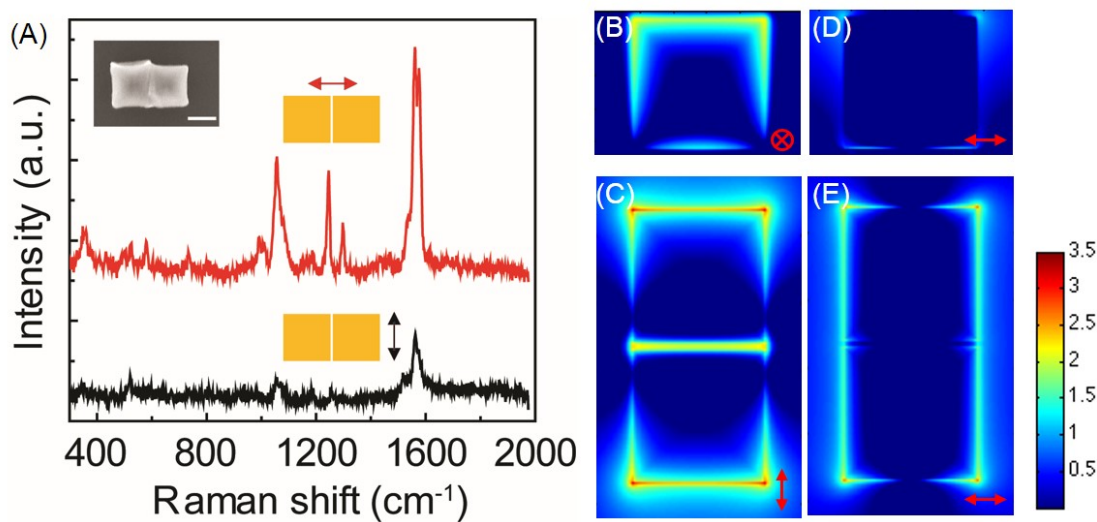


**Figure 6.7** Polarization-dependent field-enhancement of face-to-face concave nanocube dimers by Raman spectroscopy and FDTD simulation. (A) SERS Spectra of a face-to-face concave cube dimer functionalized with 1,4-BDT, showing larger SERS intensity from longitudinal (red) than transverse (black) polarization. A 785 nm laser was used for the Raman measurement. The inset SEM image shows the dimer transferred to a silicon substrate for the SERS measurement; scale bar is 100 nm. (B-E) The intensity enhancements  $|E_{\text{local}}/E_{\text{incident}}|^2$  based on FDTD simulation for both longitudinal (B, C) and transverse (D, E) polarizations at 784.5 incident wavelength. (B, D) are cross sections at the gap centers and (C, E) are cross sections at top surface of the cubes (C, E). Intensity data are shown logarithmically.

#### 6.4. Conclusions

Exploring the role of template geometry and interparticle interactions in capillary assembly allowed for the shape-selective immobilization of nanoparticles and the construction of Raman enhancing anisotropic nanoparticle dimers. Given that many interesting arrangements of plasmonic nanoparticles involve multiple particles positioned precisely, and in close proximity with one another, understanding and utilizing these immersion forces will be crucial in constructing structures such as plasmonic metasurfaces. Furthermore, as the intuition built here primarily relates to the geometry of the particles and the templates, these methods are likely generalizable to particles of different shapes and compositions. Given the breadth and high quality of nanoparticles that now can be made using solution-based syntheses,<sup>182-183</sup> this method may enable new classes of experiments that test fundamental relationships in plasmonics, photonics, and catalysis.

## References

1. Schaller, R. R., *Spectrum, IEEE* **1997**, *34*, 52-59.
2. Xia, Y.; Whitesides, G. M., *Angew. Chem., Int. Ed.* **1998**, *37*, 550-575.
3. Bruning, J. H., Deep-uv lithography. Google Patents: 1989.
4. Chou, S. Y.; Krauss, P. R.; Renstrom, P. J., *Science* **1996**, *272*, 85-87.
5. Hulteen, J. C.; Van Duyne, R. P., *Journal of Vacuum Science & Technology A* **1995**, *13*, 1553-1558.
6. Manfrinato, V. R.; Zhang, L. H.; Su, D.; Duan, H. G.; Hobbs, R. G.; Stach, E. A.; Berggren, K. K., *Nano Letters* **2013**, *13*, 1555-1558.
7. Ehrlich, D. J.; Osgood, R. M.; Deutsch, T. F., *Applied Physics Letters* **1981**, *38*, 1018-1020.
8. Garcia, R.; Knoll, A. W.; Riedo, E., *Nat Nano* **2014**, *9*, 577-587.
9. Piner, R. D.; Zhu, J.; Xu, F.; Hong, S.; Mirkin, C. A., *Science* **1999**, *283*, 661-663.
10. Binnig, G.; Quate, C. F.; Gerber, C., *Physical Review Letters* **1986**, *56*, 930-933.
11. Salaita, K.; Wang, Y. H.; Mirkin, C. A., *Nat Nanotechnol* **2007**, *2*, 145-155.
12. Kim, Y.; Lieber, C. M., *Science* **1992**, *257*, 375-377.
13. Minne, S. C.; Manalis, S. R.; Atalar, A.; Quate, C. F., *Journal of Vacuum Science & Technology B* **1996**, *14*, 2456-2461.
14. Maoz, R.; Cohen, S. R.; Sagiv, J., *Advanced Materials* **1999**, *11*, 55-61.
15. Betzig, E.; Trautman, J. K., *Science* **1992**, *257*, 189-195.
16. Wouters, D.; Schubert, U. S., *Angewandte Chemie International Edition* **2004**, *43*, 2480-2495.
17. Ginger, D. S.; Zhang, H.; Mirkin, C. A., *Angew Chem Int Edit* **2004**, *43*, 30-45.
18. Demers, L. M.; Ginger, D. S.; Park, S.-J.; Li, Z.; Chung, S.-W.; Mirkin, C. A., *Science* **2002**, *296*, 1836-1838.
19. Lee, K.-B.; Lim, J.-H.; Mirkin, C. A., *Journal of the American Chemical Society* **2003**, *125*, 5588-5589.
20. Nyamjav, D.; Ivanisevic, A., *Chemistry of Materials* **2004**, *16*, 5216-5219.
21. Huang, L.; Braunschweig, A. B.; Shim, W.; Qin, L. D.; Lim, J. K.; Hurst, S. J.; Huo, F. W.; Xue, C.; Jong, J. W.; Mirkin, C. A., *Small* **2010**, *6*, 1077-1081.
22. Jang, J.-W.; Sanedrin, R. G.; Senesi, A. J.; Zheng, Z.; Chen, X.; Hwang, S.; Huang, L.; Mirkin, C. A., *Small* **2009**, *5*, 1850-1853.
23. Wang, B.; Zhao, W.; Chen, A.; Chua, S.-J., *Journal of Crystal Growth* **2006**, *288*, 200-204.
24. Coffey, D. C.; Ginger, D. S., *Journal of the American Chemical Society* **2005**, *127*, 4564-4565.

25. Vettiger, P.; Cross, G.; Despont, M.; Drechsler, U.; Durig, U.; Gotsmann, B.; Haberle, W.; Lantz, M. A.; Rothuizen, H. E.; Stutz, R.; Binnig, G. K., *Nanotechnology, IEEE Transactions on* **2002**, *1*, 39-55.
26. Salaita, K.; Lee, S. W.; Wang, X.; Huang, L.; Dellinger, T. M.; Liu, C.; Mirkin, C. A., *Small* **2005**, *1*, 940-945.
27. Salaita, K.; Wang, Y.; Fragala, J.; Vega, R. A.; Liu, C.; Mirkin, C. A., *Angewandte Chemie* **2006**, *118*, 7378-7381.
28. Lenhert, S.; Sun, P.; Wang, Y.; Fuchs, H.; Mirkin, C. A., *Small* **2007**, *3*, 71-75.
29. Huo, F.; Zheng, Z.; Zheng, G.; Giam, L. R.; Zhang, H.; Mirkin, C. A., *Science* **2008**, *321*, 1658-1660.
30. Bian, S.; He, J.; Schesing, K. B.; Braunschweig, A. B., *Small* **2012**, *8*, 2000-2005.
31. Chai, J.; Huo, F.; Zheng, Z.; Giam, L. R.; Shim, W.; Mirkin, C. A., *Proceedings of the National Academy of Sciences* **2010**, *107*, 20202-20206.
32. Huang, L.; Braunschweig, A. B.; Shim, W.; Qin, L.; Lim, J. K.; Hurst, S. J.; Huo, F.; Xue, C.; Jang, J.-W.; Mirkin, C. A., *Small (Weinheim an der Bergstrasse, Germany)* **2010**, *6*, 1077-1081.
33. Zheng, Z.; Daniel, W. L.; Giam, L. R.; Huo, F.; Senesi, A. J.; Zheng, G.; Mirkin, C. A., *Angewandte Chemie* **2009**, *121*, 7762-7765.
34. Zhong, X.; Bailey, N. A.; Schesing, K. B.; Bian, S.; Campos, L. M.; Braunschweig, A. B., *Journal of Polymer Science Part A: Polymer Chemistry* **2013**, *51*, 1533-1539.
35. Brinkmann, F.; Hirtz, M.; Greiner, A. M.; Weschenfelder, M.; Waterkotte, B.; Bastmeyer, M.; Fuchs, H., *Small* **2013**, *9*, 3266-3275.
36. Chai, J. A.; Wong, L. S.; Giam, L.; Mirkin, C. A., *Proceedings of the National Academy of Sciences of the United States of America* **2011**, *108*, 19521-19525.
37. Bian, S. D.; Schesing, K. B.; Braunschweig, A. B., *Chem Commun* **2012**, *48*, 4995-4997.
38. Bian, S. D.; Scott, A. M.; Cao, Y.; Liang, Y.; Osuna, S.; Houk, K. N.; Braunschweig, A. B., *Journal of the American Chemical Society* **2013**, *135*, 9240-9243.
39. Huo, F. W.; Zheng, G. F.; Liao, X.; Giam, L. R.; Chai, J. A.; Chen, X. D.; Shim, W. Y.; Mirkin, C. A., *Nat Nanotechnol* **2010**, *5*, 637-640.
40. Liao, X.; Brown, K. A.; Schmucker, A. L.; Liu, G.; He, S.; Shim, W.; Mirkin, C. A., *Nat Commun* **2013**, *4*.
41. Su, M.; Liu, X.; Li, S.-Y.; Dravid, V. P.; Mirkin, C. A., *Journal of the American Chemical Society* **2002**, *124*, 1560-1561.
42. Wilson, D. L.; Martin, R.; Hong, S.; Cronin-Golomb, M.; Mirkin, C. A.; Kaplan, D. L., *Proceedings of the National Academy of Sciences* **2001**, *98*, 13660-13664.
43. Liu, X.; Fu, L.; Hong, S.; Dravid, V. P.; Mirkin, C. A., *Advanced Materials* **2002**, *14*, 231-234.
44. Wang, W. M.; Stoltenberg, R. M.; Liu, S.; Bao, Z., *ACS Nano* **2008**, *2*, 2135-2142.

45. Kim, J.; Shin, Y.-H.; Yun, S.-H.; Choi, D.-S.; Nam, J.-H.; Kim, S. R.; Moon, S.-K.; Chung, B. H.; Lee, J.-H.; Kim, J.-H.; Kim, K.-Y.; Kim, K.-M.; Lim, J.-H., *Journal of the American Chemical Society* **2012**, *134*, 16500-16503.
46. Kim, J.; Shin, Y. H.; Yun, S. H.; Choi, D. S.; Nam, J. H.; Kim, S. R.; Moon, S. K.; Chung, B. H.; Lee, J. H.; Kim, J. H.; Kim, K. Y.; Kim, K. M.; Lim, J. H., *Journal of the American Chemical Society* **2012**, *134*, 16500-16503.
47. Salaita, K.; Wang, Y.; Mirkin, C. A., *Nature Nanotechnology* **2007**, *2*, 145-155.
48. Torrey, J. D.; Vasko, S. E.; Kapetanovic, A.; Zhu, Z. H.; Scholl, A.; Rolandi, M., *Advanced Materials* **2010**, *22*, 4639-4642.
49. Saavedra, H. M.; Mullen, T. J.; Zhang, P. P.; Dewey, D. C.; Claridge, S. A.; Weiss, P. S., *Rep. Prog. Phys.* **2010**, *73*.
50. Unruh, D. A.; Mauldin, C.; Pastine, S. J.; Rolandi, M.; Fréchet, J. M. J., *Journal of the American Chemical Society* **2010**, *132*, 6890-6891.
51. Oberhansl, S.; Hirtz, M.; Lagunas, A.; Eritja, R.; Martinez, E.; Fuchs, H.; Samitier, J., *Small* **2012**, *8*, 541-545.
52. Sekula-Neuner, S.; Maier, J.; Oppong, E.; Cato, A. C. B.; Hirtz, M.; Fuchs, H., *Small* **2012**, *8*, 585-591.
53. Chai, J.; Huo, F.; Zheng, Z.; Giam, L. R.; Shim, W.; Mirkin, C. A., *Proc. Natl. Acad. Sci. USA* **2010**, *107*, 20202-20206.
54. Giam, L. R.; He, S.; Horwitz, N. E.; Eichelsdoerfer, D. J.; Chai, J.; Zheng, Z.; Kim, D.; Shim, W.; Mirkin, C. A., *Nano Lett.* **2012**, *12*, 1022-1025.
55. Liu, G. L.; Eichelsdoerfer, D. J.; Rasin, B.; Zhou, Y.; Brown, K. A.; Liao, X.; Mirkin, C. A., *Proc. Natl. Acad. Sci. USA* **2012**.
56. Jang, J. Y.; Hong, S. H.; Schatz, G. C.; Ratner, M. A., *Journal of Chemical Physics* **2001**, *115*, 2721-2729.
57. Jonathan, R. F.; Suhas, S.; Randy, H. E.; William, P. K., *Nanotechnology* **2012**, *23*, 215301.
58. Wu, C. D.; Fang, T. H.; Wu, T. T., *Polymer* **2012**, *53*, 857-863.
59. Wu, C. D.; Fang, T. H.; Lin, J. F., *Journal of Colloid and Interface Science* **2011**, *361*, 316-320.
60. Saha, S. K.; Culpepper, M. L., *Appl Phys Lett* **2010**, *96*.
61. Saha, S. K.; Culpepper, M. L., *J Phys Chem C* **2010**, *114*, 15364-15369.
62. Kim, H.; Saha, L. C.; Saha, J. K.; Jang, J., *Scanning* **2010**, *32*, 2-8.
63. Sheehan, P. E.; Whitman, L. J., *Physical review letters* **2002**, *88*.
64. John, N. S.; Kulkarni, G. U., *J Nanosci Nanotechno* **2007**, *7*, 977-981.
65. Weeks, B. L.; Vaughn, M. W.; DeYoreo, J. J., *Langmuir* **2005**, *21*, 8096-8098.
66. Wu, T. H.; Lu, H. H.; Lin, C. W., *Langmuir* **2012**, *28*, 14509-14513.
67. de Gennes, P. G.; Leger, L., *Annual Review of Physical Chemistry* **1982**, *33*, 49-61.

68. Bronstein, L. M.; Sidorov, S. N.; Valetsky, P. M.; Hartmann, J.; Cölfen, H.; Antonietti, M., *Langmuir* **1999**, *15*, 6256-6262.
69. Martin, T. J.; Procházka, K.; Munk, P.; Webber, S. E., *Macromolecules* **1996**, *29*, 6071-6073.
70. Barakat, K.; Cundari, T. R., *Chem. Phys.* **2005**, *311*, 3-11.
71. Chen, T.; Amin, I.; Jordan, R., *Chemical Society Reviews* **2012**, *41*, 3280-3296.
72. Liu, G. L.; Ramirez-Hernandez, A.; Yoshida, H.; Nygard, K.; Satapathy, D. K.; Bunk, O.; de Pablo, J. J.; Nealey, P. F., *Physical review letters* **2012**, *108*.
73. Liu, G. L.; Thomas, C. S.; Craig, G. S. W.; Nealey, P. F., *Advanced Functional Materials* **2010**, *20*, 1251-1257.
74. Nakashima, H.; Higgins, M. J.; O'Connell, C.; Torimitsu, K.; Wallace, G. G., *Langmuir* **2012**, *28*, 804-811.
75. Zhou, X. C.; Liu, Z. L.; Xie, Z.; Liu, X. Q.; Zheng, Z. J., *Small* **2012**, *8*, 3568-3572.
76. Nie, Z. H.; Kumacheva, E., *Nat. Mater.* **2008**, *7*, 277-290.
77. Braunschweig, A. B.; Huo, F. W.; Mirkin, C. A., *Nat. Chem.* **2009**, *1*, 353-358.
78. Zhou, X. Z.; Boey, F.; Huo, F. W.; Huang, L.; Zhang, H., *Small* **2011**, *7*, 2273-2289.
79. Giam, L. R.; Mirkin, C. A., *Angew. Chem., Int. Ed.* **2011**, *50*, 7482-7485.
80. Huo, F. W.; Zheng, Z. J.; Zheng, G. F.; Giam, L. R.; Zhang, H.; Mirkin, C. A., *Science* **2008**, *321*, 1658-1660.
81. Shim, W.; Braunschweig, A. B.; Liao, X.; Chai, J.; Lim, J. K.; Zheng, G.; Mirkin, C. A., *Nature* **2011**, *469*, 516-521.
82. Shim, W.; Brown, K. A.; Zhou, X. Z.; Rasin, B.; Liao, X.; Mirkin, C. A., *Proc. Natl. Acad. Sci. USA* **2012**, *109*, 18312-18317.
83. Xie, Z.; Shen, Y. D.; Zhou, X. C.; Yang, Y.; Tang, Q.; Miao, Q.; Su, J.; Wu, H. K.; Zheng, Z. J., *Small* **2012**, *8*, 2664-2669.
84. Brown, K. A.; Eichelsdoerfer, D. J.; Shim, W.; Rasin, B.; Radha, B.; Liao, X.; Schmucker, A. L.; Liu, G. L.; Mirkin, C. A., *Proc. Natl. Acad. Sci. USA* **2013**, *110*, 12921-12924.
85. Liao, X.; Brown, K. A.; Schmucker, A. L.; Liu, G. L.; He, S.; Shim, W.; Mirkin, C. A., *Nature Commun.* **2013**, *4*, 2103.
86. Bian, S.; Zieba, S. B.; Morris, W.; Han, X.; Richter, D. C.; Brown, K. A.; Mirkin, C. A.; Braunschweig, A. B., *Chem. Sci.* **2014**, *5*, 2023-2030.
87. Hu, H.; Yeom, J.; Mensing, G.; Chen, Y. F.; Shannon, M. A.; King, W. P., *Nanotechnology* **2012**, *23*, 175303.
88. Chen, Y.-Z.; Wu, C.-Y.; Lee, Y.-C., *Journal of Micromechanics and Microengineering* **2014**, *24*, 045007.
89. Eichelsdoerfer, D. J.; Brown, K. A.; Wang, M. X.; Mirkin, C. A., *J. Phys. Chem. B* **2013**, *117*, 16363-16368.

90. Hong, J. M.; Ozkeskin, F. M.; Zou, J., *J. Micromech. Microeng.* **2008**, *18*, 015003.
91. Liao, X.; Braunschweig, A. B.; Zheng, Z. J.; Mirkin, C. A., *Small* **2010**, *6*, 1082-1086.
92. Qin, D.; Xia, Y. N.; Black, A. J.; Whitesides, G. M., *J. Vac. Sci. Technol. B* **1998**, *16*, 98-103.
93. Qin, D.; Xia, Y. N.; Whitesides, G. M., *Adv. Mater.* **1997**, *9*, 407-410.
94. Giam, L. R.; Massich, M. D.; Hao, L.; Wong, L. S.; Mader, C. C.; Mirkin, C. A., *PNAS* **2012**, *109*, 4377-4382.
95. Wendeln, C.; Rinnen, S.; Schulz, C.; Arlinghaus, H. F.; Ravoo, B. J., *Langmuir* **2010**, *26*, 15966-15971.
96. Maier, W. F.; Stowe, K.; Sieg, S., *Angew. Chem., Int. Ed.* **2007**, *46*, 6016-6067.
97. Kuang, M. X.; Wang, L. B.; Song, Y. L., *Adv. Mater.* **2014**, *26*, 6950-6958.
98. Dean, N., *Nature Nanotech.* **2015**, *10*, 15-16.
99. Zhou, X. Z.; Zhou, Y.; Ku, J. C.; Zhang, C.; Mirkin, C. A., *ACS Nano* **2014**, *8*, 1511-1516.
100. Zhou, Y.; Zhou, X. Z.; Park, D. J.; Torabi, K.; Brown, K. A.; Jones, M. R.; Zhang, C.; Schatz, G. C.; Mirkin, C. A., *Nano Lett.* **2014**, *14*, 2157-2161.
101. MacBeath, G.; Schreiber, S. L., *Science* **2000**, *289*, 1760-1763.
102. Rosi, N. L.; Mirkin, C. A., *Chem. Rev.* **2005**, *105*, 1547-1562.
103. Zhong, J.; Ma, M. J.; Zhou, J.; Wei, D. X.; Yan, Z. G.; He, D. N., *ACS Appl. Mater. Interfaces* **2013**, *5*, 737-746.
104. Guo, L. J., *Adv. Mater.* **2007**, *19*, 495-513.
105. Piner, R. D.; Zhu, J.; Xu, F.; Hong, S. H.; Mirkin, C. A., *Science* **1999**, *283*, 661-663.
106. Zheng, Z. J.; Daniel, W. L.; Giam, L. R.; Huo, F. W.; Senesi, A. J.; Zheng, G. F.; Mirkin, C. A., *Angew. Chem., Int. Ed.* **2009**, *48*, 7626-7629.
107. Xie, Z.; Chen, C.; Zhou, X.; Gao, T.; Liu, D.; Miao, Q.; Zheng, Z., *ACS Appl. Mater. Interfaces* **2014**, DOI: 10.1021/am405555e.
108. Zhou, Y.; Xie, Z.; Brown, K. A.; Park, D. J.; Zhou, X.; Chen, P.-C.; Hirtz, M.; Lin, Q.-Y.; Dravid, V. P.; Schatz, G. C.; Zheng, Z.; Mirkin, C. A., *Small* **2015**, *11*, 913-918.
109. Hoyle, C. E.; Bowman, C. N., *Angew. Chem., Int. Ed.* **2010**, *49*, 1540-1573.
110. Wang, L.; Zhang, Z.; Ding, Y. F., *Soft Matter* **2013**, *9*, 4455-4463.
111. Chiou, B. S.; Khan, S. A., *Macromolecules* **1997**, *30*, 7322-7328.
112. Felts, J. R.; Somnath, S.; Ewoldt, R. H.; King, W. P., *Nanotechnology* **2012**, *23*.
113. Liu, G. L.; Zhou, Y.; Banga, R. S.; Boya, R.; Brown, K. A.; Chipre, A. J.; Nguyen, S. T.; Mirkin, C. A., *Chem. Sci.* **2013**, *4*, 2093-2099.
114. O'Connell, C. D.; Higgins, M. J.; Sullivan, R. P.; Moulton, S. E.; Wallace, G. G., *Small* **2014**, *10*, 3717-3728.
115. Chai, J. A.; Huo, F. W.; Zheng, Z. J.; Giam, L. R.; Shim, W.; Mirkin, C. A., *Proc. Natl. Acad. Sci. USA* **2010**, *107*, 20202-20206.

116. Liu, G. L.; Eichelsdoerfer, D. J.; Rasin, B.; Zhou, Y.; Brown, K. A.; Liao, X.; Mirkin, C. A., *Proc. Natl. Acad. Sci. USA* **2013**, *110*, 887-891.
117. Wu, J.; Zan, X. L.; Li, S. Z.; Liu, Y. Y.; Cui, C. L.; Zou, B. H.; Zhang, W. N.; Xu, H. B.; Duan, H. W.; Tian, D. B.; Huang, W.; Huo, F. W., *Nanoscale* **2014**, *6*, 749-752.
118. Klajn, R., *Chem. Soc. Rev.* **2014**, *43*, 148-184.
119. Guo, R. S.; Yu, Y.; Xie, Z.; Liu, X. Q.; Zhou, X. C.; Gao, Y. F.; Liu, Z. L.; Zhou, F.; Yang, Y.; Zheng, Z. J., *Adv. Mater.* **2013**, *25*, 3343-3350.
120. Hartman, R. L.; McMullen, J. P.; Jensen, K. F., *Angew. Chem., Int. Ed.* **2011**, *50*, 7502-7519.
121. Burda, C.; Chen, X.; Narayanan, R.; El-Sayed, M. A., *Chem. Rev.* **2005**, *105*, 1025.
122. Jones, M. R.; Osberg, K. D.; Macfarlane, R. J.; Langille, M. R.; Mirkin, C. A., *Chem. Rev.* **2011**, *111*, 3736.
123. Wall, B. D.; Diegelmann, S. R.; Zhang, S.; Dawidczyk, T. J.; Wilson, W. L.; Katz, H. E.; Mao, H. Q.; Tovar, J. D., *Adv. Mater.* **2011**, *23*, 5009.
124. Komanicky, V.; Iddir, H.; Chang, K. C.; Menzel, A.; Karapetrov, G.; Hennessy, D.; Zapol, P.; You, H., *J. Am. Chem. Soc.* **2009**, *131*, 5732.
125. Qin, L.; Park, S.; Huang, L.; Mirkin, C. A., *Science* **2005**, *309*, 113.
126. Banholzer, M. J.; Qin, L.; Millstone, J. E.; Osberg, K. D.; Mirkin, C. A., *Nat. Protoc.* **2009**, *4*, 838.
127. Osberg, K. D.; Schmucker, A. L.; Senesi, A. J.; Mirkin, C. A., *Nano Lett.* **2011**, *11*, 820.
128. Rivera, T. P.; Lecarme, O.; Hartmann, J.; Inglebert, R. L.; Peyrade, D., *Microelectron. Eng.* **2009**, *86*, 1089.
129. Jiang, L.; Sun, Y.; Huo, F.; Zhang, H.; Qin, L.; Li, S.; Chen, X., *Nanoscale* **2012**, *4*, 66.
130. Qin, L.; Banholzer, M. J.; Millstone, J. E.; Mirkin, C. A., *Nano Lett.* **2007**, *7*, 3849.
131. Qin, L.; Zou, S.; Xue, C.; Atkinson, A.; Schatz, G. C.; Mirkin, C. A., *Proc. Natl. Acad. Sci. U.S.A.* **2006**, *103*, 13300.
132. Wei, W.; Li, S.; Millstone, J. E.; Banholzer, M. J.; Chen, X.; Xu, X.; Schatz, G. C.; Mirkin, C. A., *Angew. Chem., Int. Ed.* **2009**, *48*, 4210.
133. Chen, X.; Yeganeh, S.; Qin, L.; Li, S.; Xue, C.; Braunschweig, A. B.; Schatz, G. C.; Ratner, M. A.; Mirkin, C. A., *Nano Lett.* **2009**, *9*, 3974.
134. Osberg, K. D.; Rycenga, M.; Bourret, G. R.; Brown, K. A.; Mirkin, C. A., *Adv. Mater.* **2012**, *24*, 6065.
135. Zhou, X.; Shade, C. M.; Schmucker, A. L.; Brown, K. A.; He, S.; Boey, F.; Ma, J.; Zhang, H.; Mirkin, C. A., *Nano Lett.* **2012**, *12*, 4734.
136. Jiao, L.; Zhang, L.; Ding, L.; Liu, J.; Dai, H., *Nano Res.* **2010**, *3*, 387.
137. Son, J. G.; Son, M.; Moon, K. J.; Lee, B. H.; Myoung, J. M.; Strano, M. S.; Ham, M. H.; Ross, C. A., *Adv. Mater.* **2013**, *25*, 4723.

138. Freitag, M.; Low, T.; Zhu, W.; Yan, H.; Xia, F.; Avouris, P., *Nat. Commun.* **2013**, *4*, 1951.
139. Ju, L.; Geng, B.; Horng, J.; Girit, C.; Martin, M.; Hao, Z.; Bechtel, H. A.; Liang, X.; Zettl, A.; Shen, Y. R., *Nat. Nanotechnol.* **2011**, *6*, 630.
140. Xu, X.; Kim, K.; Li, H.; Fan, D. L., *Adv. Mater.* **2012**, *24*, 5457.
141. Lim, J. K.; Lee, B. Y.; Pedano, M. L.; Senesi, A. J.; Jang, J. W.; Shim, W.; Hong, S.; Mirkin, C. A., *Small* **2010**, *6*, 1736.
142. Gordon, M. J.; Peyrade, D., *Appl. Phys. Lett.* **2006**, *89*, 053112-3.
143. Kraus, T.; Malaquin, L.; Schmid, H.; Riess, W.; Spencer, N. D.; Wolf, H., *Nat. Nanotechnol.* **2007**, *2*, 570.
144. Kuemin, C.; Nowack, L.; Bozano, L.; Spencer, N. D.; Wolf, H., *Adv. Funct. Mater.* **2012**, *22*, 702.
145. Millstone, J. E.; Park, S.; Shuford, K. L.; Qin, L.; Schatz, G. C.; Mirkin, C. A., *J. Am. Chem. Soc.* **2005**, *127*, 5312.
146. Nikoobakht, B.; El-Sayed, M. A., *Chem. Mater.* **2003**, *15*, 1957.
147. Murphy, C. J.; Sau, T. K.; Gole, A. M.; Orendorff, C. J.; Gao, J.; Gou, L.; Hunyadi, S. E.; Li, T., *J. Phys. Chem. B* **2005**, *109*, 13857.
148. Ondarçuhu, T.; Piednoir, A., *Nano Lett.* **2005**, *5*, 1744.
149. Freer, E. M.; Grachev, O.; Duan, X.; Martin, S.; Stumbo, D. P., *Nat. Nanotechnol.* **2010**, *5*, 525.
150. Martinson, A. B. F.; Elam, J. W.; Hupp, J. T.; Pellin, M. J., *Nano Lett.* **2007**, *7*, 2183.
151. Malaquin, L.; Kraus, T.; Schmid, H.; Delamarche, E.; Wolf, H., *Langmuir* **2007**, *23*, 11513.
152. Yan, H.; Low, T.; Zhu, W.; Wu, Y.; Freitag, M.; Li, X.; Guinea, F.; Avouris, P.; Xia, F., *Nat. Photonics* **2013**, *7*, 394.
153. Osberg, K. D.; Rycenga, M.; Harris, N.; Schmucker, A. L.; Langille, M. R.; Schatz, G. C.; Mirkin, C. A., *Nano Lett.* **2012**, *12*, 3828.
154. Stiles, P. L.; Dieringer, J. A.; Shah, N. C.; Van Duyne, R. P., *Annu. Rev. Anal. Chem.* **2008**, *1*, 601.
155. Sun, Y.; Fuge, G. M.; Ashfold, M. N. R., *Chem. Phys. Lett.* **2004**, *396*, 21.
156. Chang, W. S.; Ha, J. W.; Slaughter, L. S.; Link, S., *Proc. Natl. Acad. Sci. U.S.A.* **2010**, *107*, 2781.
157. Haes, A. J.; Van Duyne, R. P., *J. Am. Chem. Soc.* **2002**, *124*, 10596.
158. Shalaev, V. M., *Nat. Photonics* **2007**, *1*, 41.
159. Wang, X. D.; Neff, C.; Graugnard, E.; Ding, Y.; King, J. S.; Pranger, L. A.; Tannenbaum, R.; Wang, Z. L.; Summers, C. J., *Adv. Mater.* **2005**, *17*, 2103.
160. Zhang, S.; Ye, Z.; Wang, Y.; Park, Y.; Bartal, G.; Mrejen, M.; Yin, X.; Zhang, X., *Phys. Rev. Lett.* **2012**, *109*, 193902.

161. Liu, N.; Langguth, L.; Weiss, T.; Kastel, J.; Fleischhauer, M.; Pfau, T.; Giessen, H., *Nat. Mater.* **2009**, *8*, 758.
162. Yu, N.; Genevet, P.; Kats, M. A.; Aieta, F.; Tetienne, J. P.; Capasso, F.; Gaburro, Z., *Science* **2011**, *334*, 333.
163. Bogaerts, W.; Wiaux, V.; Dumon, P.; Taillaert, D.; Wouters, J.; Beckx, S.; Van Campenhout, J.; Luyssaert, B.; Van Thourhout, D.; Baets, R., *Opt. Sci. Technol., SPIE's 48th Annu. Meeting* **2003**, 101.
164. Huang, J. S.; Callegari, V.; Geisler, P.; Brüning, C.; Kern, J.; Prangsma, J. C.; Wu, X.; Feichtner, T.; Ziegler, J.; Weinmann, P., *Nat. Commun.* **2010**, *1*, 150.
165. Viarbitskaya, S.; Teulle, A.; Marty, R.; Sharma, J.; Girard, C.; Arbouet, A.; Dujardin, E., *Nat. Mater.* **2013**, *12*, 426.
166. Jamshidi, A.; Pauzauskie, P. J.; Schuck, P. J.; Ohta, A. T.; Chiou, P. Y.; Chou, J.; Yang, P.; Wu, M. C., *Nat. Photonics* **2008**, *2*, 86.
167. Brown, K. A.; Westervelt, R. M., *Nanotechnology* **2009**, *20*, 385302.
168. Brown, K. A.; Westervelt, R. M., *Nano Lett.* **2011**, *11*, 3197.
169. Krishnan, M.; Mojarrad, N.; Kukura, P.; Sandoghdar, V., *Nature* **2010**, *467*, 692.
170. Henzie, J.; Andrews, S. C.; Ling, X. Y.; Li, Z.; Yang, P., *Proc. Natl. Acad. Sci. U.S.A.* **2013**, *110*, 6640.
171. Demers, L. M.; Park, S. J.; Taton, T. A.; Li, Z.; Mirkin, C. A., *Angew. Chem., Int. Ed.* **2001**, *40*, 3071.
172. Li, H.; Zhang, J.; Zhou, X. Z.; Lu, G.; Yin, Z. Y.; Li, G. P.; Wu, T.; Boey, F.; Venkatraman, S. S.; Zhang, H., *Langmuir* **2010**, *26*, 5603.
173. Celebrano, M.; Rosman, C.; Sönnichsen, C.; Krishnan, M., *Nano Lett.* **2012**, *12*, 5791.
174. Kralchevsky, P. A.; Nagayama, K., *Langmuir* **1994**, *10*, 23.
175. Gao, B.; Arya, G.; Tao, A. R., *Nat. Nanotechnol.* **2012**, *7*, 433.
176. Jones, M. R.; Mirkin, C. A., *Angew. Chem., Int. Ed.* **2013**, *52*, 2886.
177. Millstone, J. E.; Wei, W.; Jones, M. R.; Yoo, H.; Mirkin, C. A., *Nano Lett.* **2008**, *8*, 2526.
178. Walker, D. A.; Browne, K. P.; Kowalczyk, B.; Grzybowski, B. A., *Angew. Chem., Int. Ed.* **2010**, *49*, 6760.
179. Zhou, X.; Zhou, Y.; Ku, J. C.; Zhang, C.; Mirkin, C. A., *ACS Nano* **2014**, *8*, 1511.
180. Xia, Y.; Xiong, Y.; Lim, B.; Skrabalak, S. E., *Angew. Chem., Int. Ed.* **2009**, *48*, 60.
181. Kinkhabwala, A.; Yu, Z.; Fan, S.; Avlasevich, Y.; Mullen, K.; Moerner, W. E., *Nat. Photonics* **2009**, *3*, 654.
182. Langille, M. R.; Personick, M. L.; Mirkin, C. A., *Angew. Chem., Int. Ed.* **2013**, *52*, 13910.
183. Personick, M. L.; Mirkin, C. A., *J. Am. Chem. Soc.* **2013**, *135*, 18238.